UNIVERSITÉ DU LUXEMBOURG

PhD-FSTM-2025-103
The Faculty of Science, Technology and Medicine

DISSERTATION

Defence held on 26/09/2025 in Luxembourg

to obtain the degree of

DOCTEUR DE L'UNIVERSITÉ DU LUXEMBOURG

EN INFORMATIQUE

by

Alejandro GONZÁLEZ GARRIDO
Born on 25 November 1987 in Albolote, Granada (Spain)

CONTRIBUTIONS TO HYBRID 5G AND GNSS FOR PNT APPLICATIONS

Dissertation defence committee
Dr Jorge Querol Borràs, dissertation supervisor
Research Scientist, Université du Luxembourg

Dr Symeon Chatzinotas
Professor, Université du Luxembourg

Dr Eva LAGUNAS TARGARONA, Chair
Assistant Professor, Université du Luxembourg

Dr Henk Wymeersh
Professor, Chalmers University of Technology

Dr Gonzalo Seco Granados
Professor, Universitat Autonoma de Barcelona

CONTRIBUTIONS TO HYBRID 5G AND GNSS FOR PNT APPLICATIONS

Acknowledgements

I would like to express my sincere gratitude to Dr. Jorge Querol Borràs for his invaluable mentorship, guidance, and continuous support throughout the development of this thesis. His insightful suggestions, constructive comments, and meticulous feedback have been essential for the successful completion of this work.

In addition, I would like to express my profound gratitude to Professors Symeon Chatzinotas and Henk Wymeersch for their meticulous attention to my progress and for offering invaluable guidance and support throughout this academic endeavour. The comments received during the process of working on the papers have been an invaluable source of feedback, contributing to a significant enhancement in my academic writing and mathematical rigour.

I would like to express my gratitude to Dr. Idir Edjekouane for our deliberations on receiver architectures, the suggestions he provided, his comments, and the feedback he offered.

I would like to express my sincere gratitude to Dr. Riccardo di Gaudenzi, Dr. Florian Grec, Dr. Ottavio Picchi, and Dr. Francesco Menzione for their insightful discussions and valuable suggestions regarding the technical aspects of this research.

To my partner in crime

Abstract

Global Navigation Satellite Systems (GNSS) have long served as the backbone of positioning services. However, GNSS signals are highly susceptible to interference, spoofing, and blockage, which poses significant challenges for applications that require robust and reliable positioning. Recent advances in fifth-generation (5G) wireless technologies, New Radio (NR), have opened promising pathways to deliver integrated communication and positioning services. Using the existing 5G framework to embed positioning functionalities can potentially mitigate the vulnerabilities inherent in GNSS, facilitating GNSS-independent positioning solutions.

One of the challenges in a position, navigation and timing (PNT) system is the management of the interference from several transmissions; to address the inherent challenge of interference management in dense satellite constellations, this thesis first develops a comprehensive statistical interference model tailored explicitly for non-terrestrial networks (NTN) scenarios involving multiple satellites. Through Monte Carlo simulations, realistic satellite deployments resembling commercial low-earth orbit (LEO) constellations are assessed, resulting in the formulation of a Generalised Extreme Value (GEV) distribution model for interference. This statistical characterisation reveals the interference bounds crucial for an accurate link budget analysis.

Building upon these insights, two novel payload architectures for joint communication and positioning (JCAP) in 5G-NTN are proposed and evaluated: a shared beam architecture, integrating direct-sequence spread spectrum (DSSS) for navigation signals with cyclic-prefix orthogonal frequency division multiplexing (CP-OFDM) for data, and an independent beam architecture, employing separate beams for navigation and communication services. A trade-off analysis between positioning accuracy and spectral efficiency is conducted, quantifying performance analytically via a Pareto frontier. The simulation results demonstrate that precise, metre-level positioning can be maintained consistently while minimising the impact on the loss of data throughput.

The research then introduces an advanced hybrid receiver design explicitly tailored for the integrated DSSS and OFDM signals. Utilising an extended Kalman filter (EKF), the receiver effectively estimates the Doppler shifts, providing resilient observables even in the presence of strong interference. The performance evaluations demonstrate that the proposed receiver structure maintains robust tracking capabilities under challenging signal-to-interference conditions, significantly improving overall system reliability and service continuity.

The comprehensive simulation results validate the viability and practical benefits of integrating the communication and positioning functionalities within 5G-NTN. These findings highlight that existing satellite deployments, supplemented with minimal modifications, can deliver reliable positioning services without relying on external GNSS infrastructures. This approach not only preserves backward compatibility with conventional 5G NTN terminals, but also establishes a solid foundation for the future convergence of communication, positioning, and sensing capabilities envisioned for sixth-generation (6G) wireless networks. Ultimately, this work significantly advances the feasibility of navigation services in NTN deployments without external GNSS support, paving the way for resilient and integrated next-generation wireless services.

Index

1 Introduction **1**

1.1 Background and context 1

1.2 Problem statement 5

1.2.1 First objective 5

1.2.2 Second objective 7

1.2.3 Third objective 8

1.3 Thesis outline 9

2 State of the art **11**

2.1 5G localization services 11

2.1.1 5G localization based services architecture 11

2.1.2 Messages flow for localization services 12

2.1.3 Positioning technologies in 5G 13

2.1.4 Use case requirements 18

2.2 Localization services with LEO satellites 18

2.2.1 Fused LEO-PNT 19

2.3 Interference for LEO-PNT services 20

2.4 Joint communication and positioning services 21

2.5 Summary 24

3 Suitability of data waveforms for PNT services **25**

3.1 Waveforms for JCAP 25

3.2 Waveforms models 26

3.2.1 CP-OFDM 27

3.2.2 OTFS 27

3.3 Candidate pilots for observable estimation 29

3.3.1 OFDM. 5G synchronization signal block . . . 29
3.3.2 OFDM. Starlink signal . . . 31
3.3.3 OFDM. 5G positioning reference signal . . . 31
3.3.4 OTFS. Positioning reference signal . . . 33
3.4 Data waveform evaluation for PNT observable estimation . . . 34
3.4.1 Theoretical ambiguity function for an OFDM waveform . . . 34
3.4.2 Theoretical ambiguity function for an OTFS waveform . . . 36
3.4.3 Empirical ambiguity function evaluation for the selected waveforms and pilots . . . 37
3.5 Summary . . . 39

4 Interference model extraction for the positioning reference signal in an NTN scenario 43
4.1 Scenario for 5G satellite positioning . . . 43
4.1.1 Satellite scenario . . . 44
4.1.2 Wireless channel model . . . 48
4.2 Transmitted and received signal model . . . 49
4.2.1 Downlink signal model . . . 49
4.2.2 Received signal model . . . 50
4.2.3 Matched filter . . . 50
4.2.4 Post-Matched filter signal to interference plus noise ratio analysis . . . 51
4.3 Empirical interference model extraction . . . 52
4.3.1 Monte Carlo simulator architecture . . . 53
4.3.2 GEV parameters extraction for the interference model . . . 55
4.3.3 Result discussion . . . 59
4.4 Summary . . . 60

5 Joint communication and positioning from LEO multi-beam satellite 62
5.1 System model . . . 62
5.1.1 Beamforming network . . . 63
5.1.2 Channel model . . . 70
5.1.3 Signal models . . . 71
5.1.4 Signal to interference plus noise ratio . . . 73
5.2 System optimization . . . 75
5.2.1 Spectral efficiency for data service . . . 75

5.2.2 Range estimation accuracy for navigation service . . . 76
5.2.3 Problem formulation . . . 76
5.2.4 Pareto front definition . . . 77
5.3 Simulations . . . 80
5.3.1 Full frequency re-use scenario . . . 81
5.3.2 Frequency re-use factor 3 scenario . . . 84
5.3.3 Results discussion and models comparison . . . 85
5.4 Summary . . . 91

6 Receiver architecture for joint communication and positioning 93
6.1 System model . . . 93
6.1.1 Hybrid downlink waveform . . . 93
6.1.2 Signal to interference plus noise ratio analysis . . . 95
6.2 Receiver architecture . . . 96
6.2.1 Navigation receiver . . . 96
6.2.2 5G communications receiver . . . 103
6.3 Performance evaluation . . . 104
6.3.1 OFDM degradation after including the DSSS . . . 105
6.3.2 Receiver operating curve . . . 107
6.3.3 Observable estimation . . . 109
6.3.4 Communication receiver assisted by DSSS . . . 112
6.4 Summary . . . 112

7 Discussion and perspectives 115
7.1 Principal findings . . . 115
7.2 Planned extensions of the present work . . . 116
7.3 A vision for next joint communication and positioning services . . . 117
7.4 Concluding remarks . . . 117

A Extreme value theory 119
A.1 Preliminaries and notation . . . 119
A.2 The Fisher-Tippett-Gnedenko theorem . . . 119
A.3 Block-Maxima model for RF interference . . . 120
A.3.1 Block definition . . . 120
A.3.2 Justification via FTG theorem . . . 120
A.4 Fitness tests . . . 121

A.4.1 Kolmogorov-Smirnov / Anderson-Darling . . . 121
A.4.2 p-value . . . 122
A.5 Interpretation for RF interference . . . 122

B Dataset generation **123**
B.1 Scenario . . . 123
B.2 Dataset generation . . . 124
B.3 Channel model . . . 125
B.4 Received signal model . . . 127

C PVT engines **128**
C.1 Measurement models . . . 128
C.1.1 Pseudorange . . . 129
C.1.2 Doppler shift . . . 129
C.2 Engine performance . . . 129
C.2.1 Initial estimation . . . 129
C.2.2 First estimation using EKF . . . 130
C.2.3 Fine estimation using non linear least squares . . . 133

D List of contributions **135**
D.1 Journals . . . 135
D.2 Conferences . . . 136
D.3 Other contributions . . . 136
D.4 Book chapter . . . 137
D.5 Thesis co-supervised . . . 137
D.6 Projects involved . . . 137

E References **140**

List of Figures

1.1 Timeline of cellular communication reporting the associated 3GPP releases, and the main positioning enhancements extracted from [3]. 2
1.2 Non-Terrestrial and Terrestrial networks unification extracted from [17] . . . 3
1.3 Hybrid communications and navigation service concept presented in [29] . . . 4
1.4 OFDM+DSSS combination for data and a navigation services within the 5G frame structure. 8
1.5 Structure of the technical contributions 10

2.1 Location services architecture in 5G, from 3GPP TS 38.305 12
2.2 Location service support in 5G, from 3GPP TS 38.305 14
2.3 Split in frequency and time of the operator spectrum in different BWP 22

3.1 5G Synchronization Signal Block 30
3.2 5G PRS Resource Grid allocation. Size 1 Resource Block × 1 Slot. All PRS share the same distribution 33
3.3 5G PRS Resource Grid allocation. Size 1 Resource Block × 1 Slot 33
3.4 Comparison of the Ambiguity Function for different waveforms 38
3.5 Delay cut ($\upsilon = 0$ [Hz]) of the ambiguity function (AF) for different waveforms. 39
3.6 Doppler cut ($\tau = 0$ [s]) of the AF for different waveforms. 40
3.7 Delay cut ($\upsilon = 0$ [Hz]) of the AF and cross ambiguity function (CAF) for different waveforms. 41
3.8 Doppler cut ($\tau = 0$ [s]) of the AF and CAF for different waveforms. 42
3.9 PDF of the maximum value of the CAF for two configurations of the PRS. The 5 MHz includes all possible combinations of ID, while the 30 MHz only 1000 combinations due memory limitations. 42

4.1 A typical satellite user view, where the maximum slant range is defined by R_{MAX} at an elevation angle of 0°. It also shows the usable area as a spherical cap A in green, defined by the minimum elevation angle θ_{MASK}. At the elevation angle θ_{MASK}, the satellite is at the maximum usable distance ρ_{MAX}. The figure also displays different satellites: one of interest, three that could interfere with the satellite of interest, and one out of sight of the user. 45
4.2 Distances and angles within a satellite beam depends on the user local horizon (LH), and the altitude of the satellite h_{SAT}. 46
4.3 Parameters involved in a single satellite pass. 47
4.4 5G PRS LEO simulator architecture. 53
4.5 User's distribution of the dataset. 54
4.6 An example of a probability density function (PDF) of the interference power used to compare the results from the Monte Carlo simulation and the generalized extreme value (GEV) distribution. 56
4.7 k value for both dataset separately, k for the combined dataset and the confidence interval 58
4.8 σ value for both dataset separately, σ for the combined dataset and the confidence interval 59
4.9 μ value for both dataset separately, μ for the combined dataset and the confidence interval using $P_{\mathrm{TX}} = 10\,\mathrm{dBW}$ 60

5.1 K beams sharing data and navigation service. They all have the same color as all of them transmit the same waveform composed by the DSSS and OFDM. 64
5.2 System diagram for K beams. Each beam share a communication (green color) and a navigation (blue color) service as each beam transmission chain is composed by the same elements. The color after the waveforms aggregation represent the combination of green and blue color. 65
5.3 K different beams for data and a single beam for navigation service. 66
5.4 System Diagram. Each data beam is independent and only one beam for navigation services that is independent from the data beams. 67
5.5 full frequency re-use (FFR). Shared beam model. SINR [dB] reference for the Data beams. 82
5.6 FFR. Shared beam model. SINR [dB] reference for the Navigation beams. . . 83
5.7 FFR. Shared beam model. Complementary Cumulative Density Function of the SINR in the area of interest for different values of ρ. 84

5.8 FFR. Independent beam model. SINR [dB] reference for the Data beams. . . 85
5.9 FFR. Independent beam model. SINR [dB] reference for the Navigation beams. 86
5.10 FFR. Independent beam model. Complementary Cumulative Density Function of the SINR in the area of interest for different values of ρ. 87
5.11 frequency re-use factor 3 (FR3). Shared beam model. SINR [dB] reference for the Data and navigation beams. 88
5.12 FR3.Shared beam model. Complementary Cumulative Density Function of the SINR in the area of interest for different values of ρ. 88
5.13 FR3. Independent beam model. SINR [dB] reference for the Data and navigation beams beams. 89
5.14 FR3. Independent beam model. Complementary Cumulative Density Function of the SINR in the area of interest for different values of ρ. 89
5.15 Spectral efficiency η and Cramer-Rao lower bound (CRLB) comparison between shared beam model and independent beams in the different scenarios from Table 5.3. Also for the large bandwidth a comparison from using the 5G PRS as positioning signal. 90

6.1 Transmitter architecture for satellite q integrating direct-sequence spread spectrum (DSSS) and orthogonal frequency-division multiplexing (OFDM) waveforms for joint communication and positioning (JCAP) services. 94
6.2 Single channel navigation receiver architecture. The complete navigation receiver is composed by several channels running in parallel, each for a different DSSS. 97
6.3 2D CA-CFAR algorithm 100
6.4 5G OFDM receiver architecture. 104
6.5 error vector magnitude (EVM) for different fifth generation (5G) signals. From the minimum resource block (RB) of 1, the number of RB for the synchronization system block (SSB) as 20 and the maximum RB in frequency region 1 (FR1) as 273. It includes the EVM limits for different modulations as required by 3rd generation partnership project (3GPP). 107
6.6 Receiver operating curve for different values of DSSS signal-to-interference ratio (SIR) for a signal with RB=1. 108
6.7 Comparison of the RB to detect the DSSS for different values of interference from OFDM and receiver noise. 108

6.8 Number of epochs to reach an error in the Doppler estimation below 1 Hz for different values of signal-to-interference plus noise ratio (SINR) of the DSSS. 110
6.9 DSSS Doppler tracking using EKF. With a SIR of −10 dB. 111
6.10 DSSS Doppler tracking using EKF. With a SIR of −20 dB. 111
6.11 Absolute error for Doppler estimation from EKF using the DSSS as reference for different values of SIR. 112
6.12 Uncoded BER for the PDSCH in 5G for different values of SIR between the 5G OFDM signal and the DSSS pilots. The uncoded BER "Only AWGN" is the benchmark where no DSSS is included, and the channel is only AWGN. . 113

B.1 Starlink Delay/Doppler values for a 4-hours passes 126
B.2 Different channel model representations 127

C.1 User position estimation error using only EKF and different number of observables 132
C.2 User position estimation error using only Non Linear Least-Squares Algorithm 134
C.3 User position estimation error by initializing the Non-Linear Least-Squares Algorithm using the results from the EKF 134

List of Tables

2.1 Use cases positioning accuracy requirements 18

3.1 Waveform comparison for joint communication and positioning systems . . . 26
3.2 Summary of waveform KPIs for observable estimation 39
3.3 Summary of waveform KPIs for observable estimation 40

4.1 Scenario details 55
4.2 PRS generation details. 55
4.3 Kolmogórov-Smirnov test (KS) test and p-test result for the different distribution evaluated. 56
4.4 Comparison of GEV parameters between the Generic, Polar, and starlink scenarios. 57
4.5 R^2 metric for the fitting of the curves. 58

5.1 Comparison of shared beam model and independent beam model for Joint Communication and PNT services 70
5.2 Scenario details 81
5.3 Scenarios bandwidth 82
5.4 Minimum usable ρ to get at least $\eta \geq 1$ and the accuracy obtained in the range estimation 87

6.1 Simulations parameters 106

B.1 Structure of the starlink dataset 125

C.1 Positioning algorithms 128

Acronyms

5G	fifth generation
6G	sixth generation
3GPP	3rd generation partnership project
ADC	analog to digital converter
AF	ambiguity function
AMF	access and mobility function
AoA	angle of arrival
AoD	angle of departure
AWGN	additive white Gaussian noise
BER	bit error rate
BFN	beamforming network
BWP	bandwidth part
BWPP	bandwidth part for positioning
CA	cell averaging
CAF	cross ambiguity function
CCDF	complementary cumulative density function
CFAR	constant false alarm rate
CIR	channel impulse response
CMMB	China mobile multimedia broadcasting
CP	cyclic prefix
CRLB	Cramer-Rao lower bound

CSI channel state information

CSS chirp spread spectrum

DBF digital beamforming

DD delay-Doppler

DDM delay-Doppler map

DL downlink

DMRS demodulation reference signal

DSSS direct-sequence spread spectrum

ECID enhanced cell-ID

E-SMLC evolved serving mobile location center

EIRP equivalent isotropic radiated power

EKF extended Kalman filter

ESA European Space Agency

EVM error vector magnitude

EVT extreme value theory

FHSS frequency hopping spread spectrum

FFT fast Fourier transform

FFR full frequency re-use

FOV field of view

FSPL free space path loss

FR1 frequency region 1

FR2 frequency region 2

FR3 frequency re-use factor 3

GEV generalized extreme value

gNB next generation base station

GNSS global navigation satellite system

HAPS high-altitude platform system

HIL hardware-in-the-loop

HPA high power amplifier

ICAL integrated communications and localization

ICASSP international conference on acoustic, speech and signal processing

IDFT inverse discrete Fourier transform

IMT international mobile telecommunications

INI inter-numerology interference

ICI inter-carrier interference

ISI inter-symbol interference

ISFFT inverse symplectic finite Fourier transform

JCAP joint communication and positioning

KPI key performance indicator

KS Kolmogórov-Smirnov test

LBA link budget analysis

LBS location based services

LEO low earth orbit

LFSR linear feedback shift registers

LH local horizon

LMF location management function

LOS line-of-sight

LTE long term evolution

MNO mobile network operator

MSE mean square error

ng-eNB next generation evolved nodeB

NG-RAN new generation radio access network

NLSQ non-linear least-squares

NR new radio

NTN non-terrestrial network

OFDM orthogonal frequency-division multiplexing

OJ-COMS open journal of the Communications Society

OTA over-the-air

OTFS orthogonal time frequency space

PBCH physical broadcast channel

PCI physical cell ID

PDSCH physical downlink shared channel

PDF probability density function

PDoA phase difference of arrival

PLL phase-locked loop

PNT positioning, navigation, and timing

PRS positioning reference signal

PSS primary synchronization signal

PVT position, velocity and time

QoS quality of service

RB resource block

RE resource element

RG resource grid

RIoT remote internet of things

RMSE root mean square error

ROC receiver operating curve

RTT round trip time

RRC radio resource control

RSRP reference signal received power

RSRQ reference signal received quality

SDR software defined radio

SIC sequential interference cancellation

SIR signal-to-interference ratio

SINR signal-to-interference plus noise ratio

SFN single frequency network

SL sidelink

SLP SUPL location platform

SNO satellite network operator

SNR signal-to-noise ratio

SoO signal of opportunity

SS synchronization signal

SSB synchronization system block

SSP subsatellite point

SSS secondary synchronization signal

SUPL secure user plane location

TA timing advance

TC-OFDM time-coded orthogonal frequency division multiplexing

TDoA time difference of arrival

TF time-frequency

ToA time of arrival

TTFF time to first fix

UAV unmanned aerial vehicle

UE user equipment

UL-AoA uplink angle of arrival

UL-TDoA uplink time difference of arrival

UPA uniform planar array

WGS84 world geodetic system 84

WSS wide-sense stationary

Mathematical notation

p Scalar number.

p Boldface lowercase letters: Array or vector.

P Boldface uppercase letters: Matrix.

$(\cdot)^*$ Complex conjugate.

$\otimes$ Kronecker product.

$\mathcal{CN}(0, \sigma^2)$ Complex Gaussian random variable with zero mean and variance σ^2.

$\mathcal{N}(0, \sigma^2)$ Gaussian random variable with zero mean and variance σ^2.

$\mathcal{U}(a, b)$ Uniform random variable defined between a and b.

$\mathbb{E}\{\cdot\}$ Expectation.

$(\cdot)^{\mathsf{T}}$ Transpose matrix.

$(\cdot)^{\mathsf{H}}$ Hermitian matrix, conjugate complex, and transpose.

wrap$\{\cdot\}$ Phase wrapping. Confines the argument (angle) to $(-\pi, \pi]$.

$\mathbb{C}^{m \times n}$ The $m \times n$ dimension complex unitary space.

$\circ$ Element-wise product.

$[\mathbf{A}|\mathbf{B}]$ Matrix composed of two concatenated submatrices **A** and **B**, where the number of rows is the same.

diag$\{\cdot\}$ Diagonal matrix.

$\oplus$ denotes bitwise modulo-2 addition (XOR).

Chapter 1

Introduction

This chapter provides the context and essential background required for a comprehensive understanding of the research problem addressed in this thesis, that is, to design a joint communication and navigation service from low earth orbit (LEO) satellites that use 5G as communication system.

This chapter starts by describing the location based services (LBS) in 5G networks, then briefly describes the 5G non-terrestrial network (NTN) scenario highlighting the gap in NTN systems, the requiring the inclusion of a positioning, navigation, and timing (PNT) service. Moreover, this chapter outlines the research question and the objectives to cover this gap. Finally, the chapter summarises the main contributions of the thesis and presents an overview of its structure, organisation, and subsequent chapters.

1.1 Background and context

In 3GPP Release 16 of 5G new radio (NR), LBS features were standardised to offer these services for terrestrial networks [1]. The inclusion of LBS services within the cellular network begins as a requirement for emergency calls, to estimate the position of a caller [2]. In the 5G framework, there are different methods used for the LBS services [2], as seen in Fig. 1.1. They have evolved over time, improving their accuracy and including other methods for LBS increasing the uses cases that benefit from these services.

Among these, the use of a specific downlink signal, positioning reference signal (PRS), is notable for its wider bandwidth and higher carrier frequencies compared to previous generations (i.e., as long term evolution (LTE)), reaching up to 100 MHz in the FR1 band and up to 400 MHz in the frequency region 2 (FR2) band [4, 5]. However, the current definition of

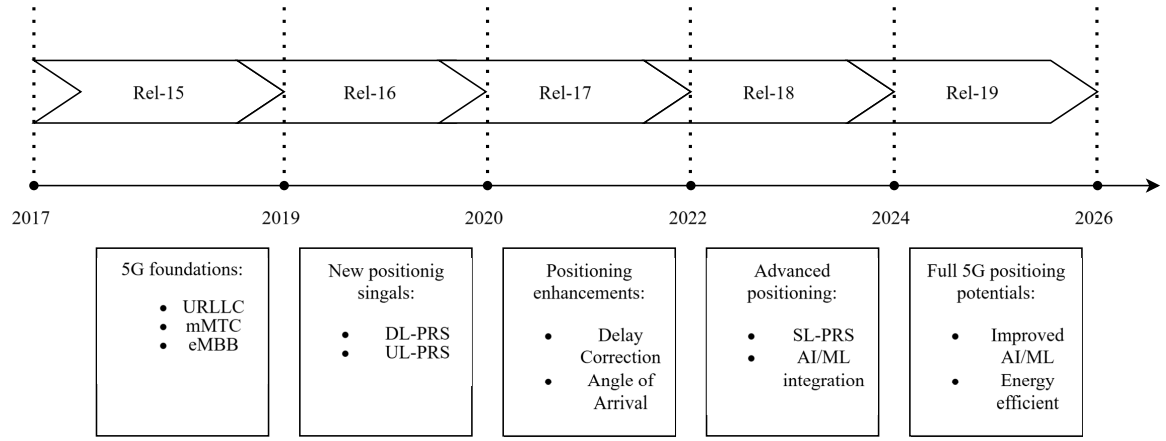

Fig. 1.1: Timeline of cellular communication reporting the associated 3GPP releases, and the main positioning enhancements extracted from [3].

5G LBS services implies that the user equipment (UE) is in the radio resource control (RRC) connected mode, i.e., a state in which the UE has established an RRC connection with next generation base station (gNB) and with the core, allowing an active communication and resource management between the UE and network. This means that the PRS is a scheduled signal, in other words, 5G LBS is an on-demand service, initiated by the UE, the core network, or a third party connected to the core network (such as emergency centers E911/E112)[6]. This on-demand service of 5G LBS contrast with global navigation satellite system (GNSS), which is a broadcast service [7]. Therefore, a first challenge appears, the 5G LBS can reach a maximum number of users, while in GNSS the number of users are unlimited. This is critical for large areas, such as those covered by satellites, where several users might need to access to 5G LBS.

Starting from Release 17, the NR architecture incorporates NTN connectivity, i.e., unmanned aerial vehicles (UAVs), high-altitude platform systems (HAPSs) or satellites, responding to the growing industry demand for global connectivity [8]. Continue from this Release 17 to Release 19, NTN is further defined, and one of the main requirement imposed at 3GPP is that the UEs should incorporate a GNSS receiver to access NTN services [9]. Besides, from Release 18, 3GPP has added a feature to verify the location of the UE independently of the GNSS to reduce the dependency on this third party system, i.e., the GNSS. Therefore, this requirement has introduced significant challenges due to inherent limitations of GNSS receivers. GNSS receivers experience considerable limitations, including signal blockage and attenuation in urban environments and dense foliage, and multipath effects caused by signal reflections from buildings and terrain. These factors

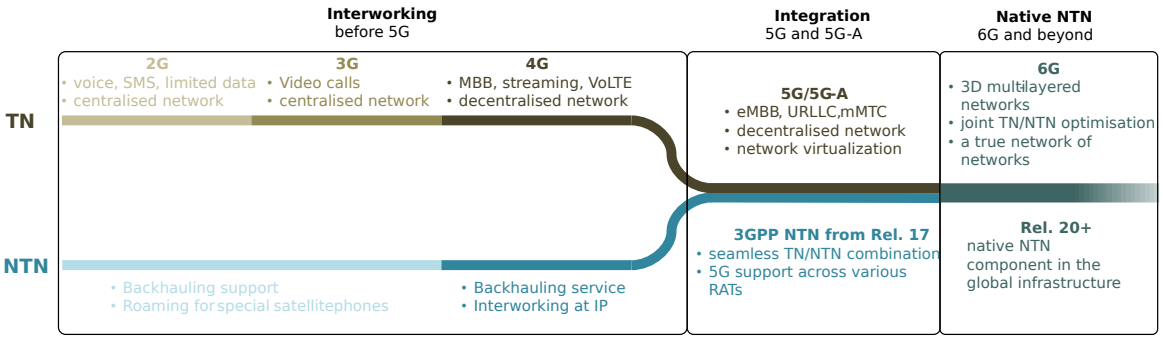

Fig. 1.2: Non-Terrestrial and Terrestrial networks unification extracted from [17]

reduce positioning accuracy and reliability [7]. Additionally, GNSS signals are vulnerable to jamming and spoofing, posing security risks for critical applications where NTN connectivity is required [10]. Moreover, in remote internet of things (RIoT) devices the substantial power consumption of GNSS receivers can compromise their commercial viability, especially in battery-powered devices that require long-term unattended operation [11]. Taken together, these limitations affect not only the positioning reliability and accuracy, but also the capability of satellite network operators (SNOs) to deliver their services in GNSS-denied areas, where despite the existence of line-of-sight (LOS) between satellites and UEs, the NTN service is compromised.

Consequently, from Release 20 the effort is put into the development of GNSS-independent UEs for NTN operation [12]. This imperative motivates the exploration of integrated PNT services alongside communication capabilities through a unified NTN infrastructure. Furthermore, integrating PNT within the 5G NTN framework could enhance resilience, improve security, and low latency positioning necessary for emerging applications [13, 14].

Looking beyond 5G, the upcoming sixth generation (6G) network is expected to establish a unified network entity as seen in Fig. 1.2. It will be characterised by multiple connectivity layers designed to meet the requirements of various devices in diverse scenarios [15]. Moreover, a GNSS-independent operation is presented in the European project 6G-NTN [16] as a key technology for 6G in LEO scenario. Another example is the European Commission project call *6G NTN-TN Unification / Integration HORIZON JU SNS 2025 01 STREAM B 03 01* where one of its objectives is *to provide GNSS-free positioning.*

Therefore, the convergence of PNT services with NTN offers numerous advantages, as Fig. 1.3 shows, including the development of a sovereign integrated communication and navigation system under a unified network infrastructure [18, 14]. Recent studies highlight the technological potential to achieve a truly integrated communication, location, and sensing

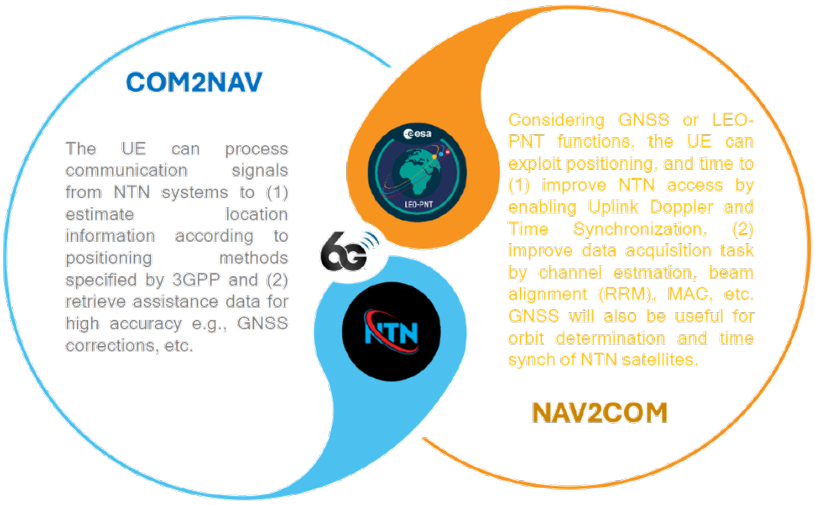

Fig. 1.3: Hybrid communications and navigation service concept presented in [29]

system [19, 20, 21, 22, 23].

The industry is also making progress with the development of PNT services such as Xona Inc. [24], the European Space Agency (ESA) LEO-PNT mission [25], the Geesat constellation from China [26] and recently, Starlink is also planning to offer PNT services to its users [27]. Furthermore, the LEO-PNT market report on [28] underscores the growing importance and potential of LEO-PNT based navigation systems as complementary alternatives to traditional GNSS. These advances are primarily driven by the demand for improved signal resilience, enhanced coverage in challenging environments, and rapid satellite upgrade cycles. However, the same report highlights critical challenges such as system interoperability, spectrum management, and governance, which necessitate coordinated efforts among commercial entities, governments, and international organisations to avoid fragmented standards and systems. In addition, most of these commercial developments do not include a communication service and those that include it, are not standardised, emphasising the need for an integrated and standardized solution.

Moreover, there are notable distinctions between GNSS and LEO-PNT systems. Specifically, the closer proximity of LEO satellites to Earth introduces complexities in orbit determination, ionospheric correction, and precise time synchronisation [30]. Recent technological developments have allowed commercial organisations to enter the market, introducing various offerings such as dedicated PNT constellations [24], signals of opportunity [31], and integrated communication-PNT systems [32]. This evolving landscape further motivates rigorous research to develop innovative LEO-PNT systems capable of

overcoming current GNSS vulnerabilities and limitations.

1.2 Problem statement

In this previous context, developing GNSS-independent PNT services integrated within the 5G NTN infrastructure is essential. Such an approach would mitigate the limitations of GNSS receivers, provide reliable and secure PNT services, and support emerging applications requiring high-precision positioning.

This study explores the feasibility and implementation of offering PNT services alongside data services through a NTN infrastructure, aiming to contribute to the advancement of integrated communication and navigation systems.

Given these considerations, the primary research question addressed in this thesis is: **Is it feasible to provide joint communication and positioning (JCAP) services compatible with actual 5G NTN systems without requiring GNSS receivers at the UE?**

To answer this question, the following objectives are established.

1.2.1 First objective

The first objective covered in this thesis is to evaluate whether current 5G LBS solutions designed for terrestrial scenarios can be effectively extended to NTN environments. Chapter 3 presents the details for the evaluation of the data waveforms used for PNT services, and discuss if they can be extended to NTN environments. This chapter provides a comprehensive definition and analysis of the ambiguity function (AF) and cross ambiguity function (CAF) derived for various waveforms and the pilot used for PNT services in the existing literature. This analysis reveals the influence of waveform parameters on the performance of signal detection and later observable estimation.

Next, Chapter 4 develops a novel empirical model that characterises the interference of the reception several PRS during the acquisition process. This interference occurs when broadcasting multiple PRS signals simultaneously from different satellites. This work adapts the terrestrial multiplexing scheme for multiple PRS signals outlined by [6] into the NTN scenario.

The proposed approach mirrors the principles of GNSS operation, wherein the satellite network operator (SNO) allocates a dedicated bandwidth part (BWP), exclusively for broadcasting PRS signals from all satellites. This strategy requires a detailed interference

analysis to ensure that interference levels remain sufficiently low, permitting detection of the signal with a certain probability of false alarm. Consequently, this research introduces a novel interference model tailored to such a waveform. The key advantage of using the proposed dedicated BWP approach is universal PRS accessibility for all users, analogous to GNSS, thus enabling UE to estimate its position without dependence on GNSS receivers, and without being connected to the network, for example before the UE starts the initial access.

The core of this objective is modelling the maximum interference power experienced by ground-based user terminals. This modelling specifically addresses the statistical characteristics of interference, which are crucial for accurate signal detection. Typically, statistical modelling emphasises central tendencies, including measures such as mean, median, and variance, highlighting common observations from the dataset. However, the statistical method used in this chapter specialises in evaluating rare and extreme events, particularly those in the distribution tails. Unlike typical outliers that might result from errors, these extremes represent valid, yet infrequent, occurrences significantly distant from central values, bearing substantial practical implications such as the miss-detection of the signal. An example of an extreme event in this context is the reception of two satellites, one with very low elevation angle and another just overhead the user; in this scenario, the differences in received power from each satellite could be very large, and the signal from the overhead satellite can mask the signal from the low elevation angle satellite.

The use of extreme value theory (detailed in Appendix A) provides an analytical tool for modelling these rare but with large impact events, allowing their estimation and forecasting. Due to the rarity of extreme interference events, extensive simulations are necessary to develop a reliable model.

The main contributions of this objective include:

1. Conduct a theoretical analysis of the received signal and the interference generated by the simultaneous reception of four PRS signals. This interference is calculated at the output of the matched filter at the receiver, before the detection step.

2. Develop a Monte Carlo simulator to evaluate the interference generated by the PRS. The simulator inputs are the different waveform parameters, and its output is a dataset with the signals power.

3. Apply extreme value statistics, specifically the block maxima approach, to characterise PRS interference from the output of the matched filter. By focussing on the extreme

values of interference, this approach not only provides a novel model for interference but also facilitates the comparison of different waveform parameters under conditions of rare but impactful interference events.

4. Extract a novel stochastic model of the interference generated by the PRS. This model is based on the configuration of the PRS, such as the transmitted power, the number of symbols, and the Comb Size used on the transmitter side. The model fitting is performed empirically using the results from the previously designed Monte Carlo simulator, confirming that the interference from other PRS follows the extreme value theorem empirically.

This method, adapted from fields where the impact of extreme events is critical, offers valuable insights into the performance and reliability of the matched filter and the detection of signals.

1.2.2 Second objective

From the analysis of the state of the art, a gap in the literature has been identified that needs to be addressed to develop a JCAP system. Therefore, the second objective of the thesis in Chapter 5 propose two novel system architectures to deliver PNT services within the 5G NTN scenario as a GNSS-independent approach, and transparent to the UE. One aggregates both services within the same beam and the second architecture develop several spot beams for data communication and a wide beam to provide a PNT service. This hybridization of services are based on the 5G NTN for the data services and a DSSS waveform for the PNT service.

The main contributions of this objective include:

1. Description and comparison of the two architectures of multi-beam satellite using digital beamforming (DBF) to provide JCAP services. The first architecture follows a similar approach to the China mobile multimedia broadcasting (CMMB) terrestrial system [33], aggregating both services within the same transmission. Furthermore, the recent work [32] has an approach similar to the first architecture. The second architecture presented in this work uses a wider beam for PNT services and spot beams for communications.

2. Inspired by the waveform used in CMMB, adapt the actual 5G NTN waveform to include a navigation component as in Fig. 1.4.

3. Compare an actual JCAP systems as the 5G PRS with these proposed architectures and discuss the trade-offs of each.

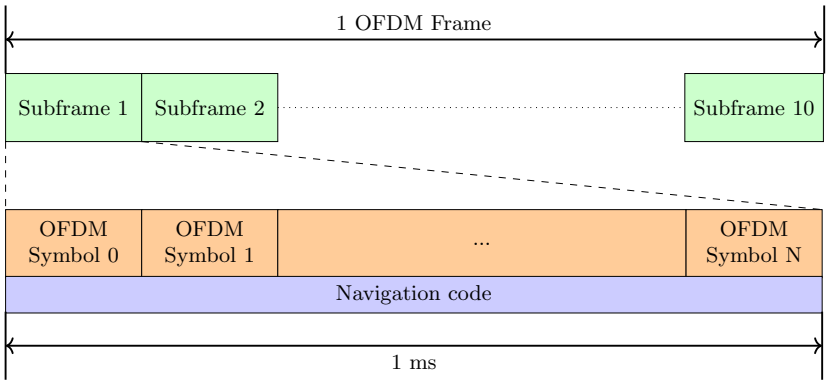

Fig. 1.4: OFDM+DSSS combination for data and a navigation services within the 5G frame structure.

4. Describe how to align both signals in time to improve the communications service. The navigation signal is used to detect the start of the OFDM symbol instead of classic algorithms used in OFDM such as [34]. In addition, the communication service is used to spread navigation and correction messages at a much higher rate as in assisted GNSS systems to achieve the concept presented in Fig. 1.3.

5. Optimisation of the SIR between the communication and navigation signals to maximise both services simultaneously by finding the Pareto front between both key performance indicators (KPIs), the CRLB for PNT and the spectral efficiency of the communication service.

This waveform aggregation depicted in Fig. 1.4 presents several benefits to the actual JCAP systems:

- The UE can use the baseband processing chain already designed for 5G, or it can use a processing chain for the DSSS for PNT services, or a combination of both. Therefore, the inclusion of PNT is back compatible with actual 5G NTN devices.

- The network operator can offer their communication service in GNSS denial areas by enabling the navigation service.

1.2.3 Third objective

The last objective of this thesis is to design, implement, and evaluate the performance of a JCAP receiver designed to hybridise communication and PNT services in 5G NTN scenarios, aiming to enhance overall service capabilities as highlighted in Fig. 1.3. Chapter 6 presents the design, implementation and performance of a JCAP receiver. It is designed to hybridise

communication and PNT services in 5G NTN scenarios. This work proposes an innovative hybrid JCAP receiver architecture that fully integrates navigation and communication processes in order to achieve the JCAP concept detailed in [29]. This integration is done by using the channel parameters estimations from the navigation component to enhance the signal used for the communication service. Once the observables are obtained in this receiver, in Appendix C is presented a position, velocity and time (PVT) engine based on extended Kalman filter (EKF) and non-linear least-squares (NLSQ) algorithm that uses only Doppler measurements to estimate the UE absolute position.

The main contributions of this objective include:

1. The introduction of a novel hybrid JCAP receiver architecture that employs the DSSS component for accurate estimation of channel parameters, subsequently utilising these estimates for channel equalisation, thus reducing pilot signals.

2. Evaluate the tracking loops in the receiver based on an EKF.

3. A detailed evaluation of the performance of the navigation receiver in terms of:

   (a) For navigation: observables estimation accuracy, explicitly considering the coexisting OFDM waveform as interference.

   (b) For data service: Analysis of the uncoded bit error rate (BER) under different DSSS interference conditions and compared with actual OFDM systems.

By addressing these three objectives, this thesis aims to significantly advance the development and implementation of integrated communication and navigation systems within existing 5G NTN infrastructures.

1.3 Thesis outline

The content of each chapter is listed below and a comprehensive list of contributions made during this thesis is provided in the Appendix D. Furthermore, Fig. 1.5 outlines the organisation of the thesis.

- Chapter 1, Introduction.
- Chapter 2, State of the art.
- Chapter 3, Suitability of data waveforms for PNT services.

- Chapter 4, Positioning Reference Signal Interference Model.
- Chapter 5, Joint Communication and Positioning from LEO Multi-Beam Satellite.
- Chapter 6, Receiver Architecture for Joint Communication and Positioning.
- Chapter 7, Discussion and perspectives.
- Appendix A, Extreme Value Theory.
- Appendix B, Dataset generation.
- Appendix C, Positioning engine.
- Appendix D, List of contributions.

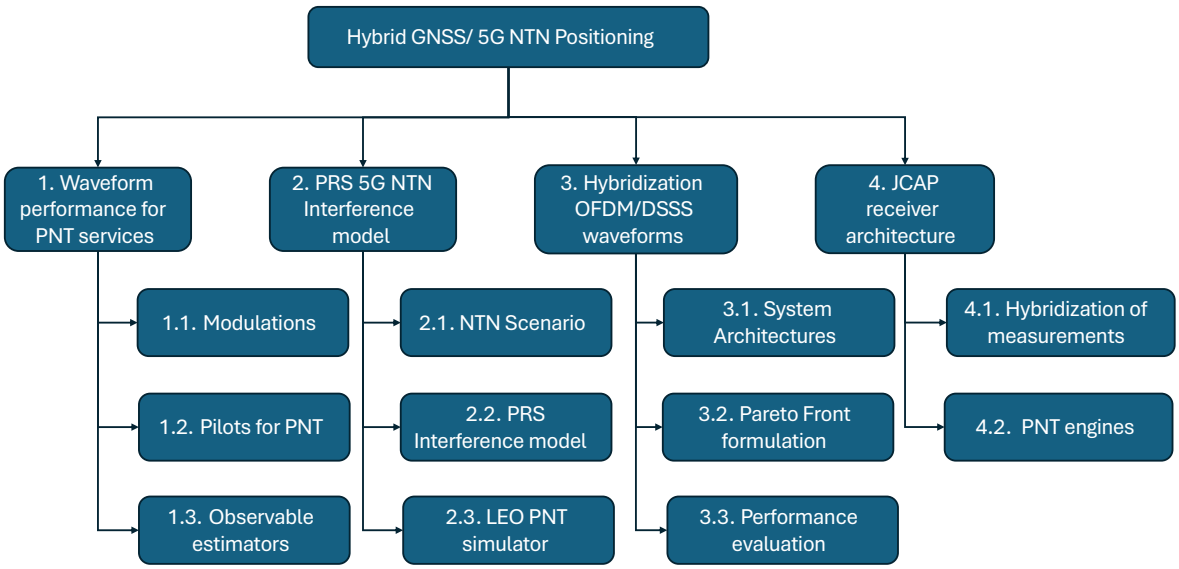

Fig. 1.5: Structure of the technical contributions

Chapter 2

State of the art

This chapter provides an extensive review of the state of the art in research and developments in the fields of 5G LBS, LEO-PNT and JCAP. Given the increasing industrial interest and advancements in these technologies, the review integrates industrial innovations in these topics. This comprehensive approach ensures a balanced perspective, capturing some of the gaps in theoretical progress and practical implementations later filled by the thesis contributions.

This state of the art is divided into the 3GPP standardised 5G LBS services, then how PNT can be offered by LEO satellites, the interference in LEO services, the analysis of JCAP systems and it concludes with a comparison of the different waveforms used for these systems.

2.1 5G localization services

There are several works that provide an overview on 5G positioning system such as [6, 2, 35, 36, 37, 38, 39], and a complete tutorial in the standardised 5G positioning in [3]. This section will briefly present the architecture for 5G LBS, the messages flow between 5G entities and the different localisation methods used.

2.1.1 5G localization based services architecture

The 3GPP standardised architecture for LBS in 5G is presented in Fig. 2.1. It is inherited from LTE [2], and was initially designed for emergency calls as a terrestrial positioning system [2, 40].

The elements of this architecture are the following.

- UE: is the user terminal.

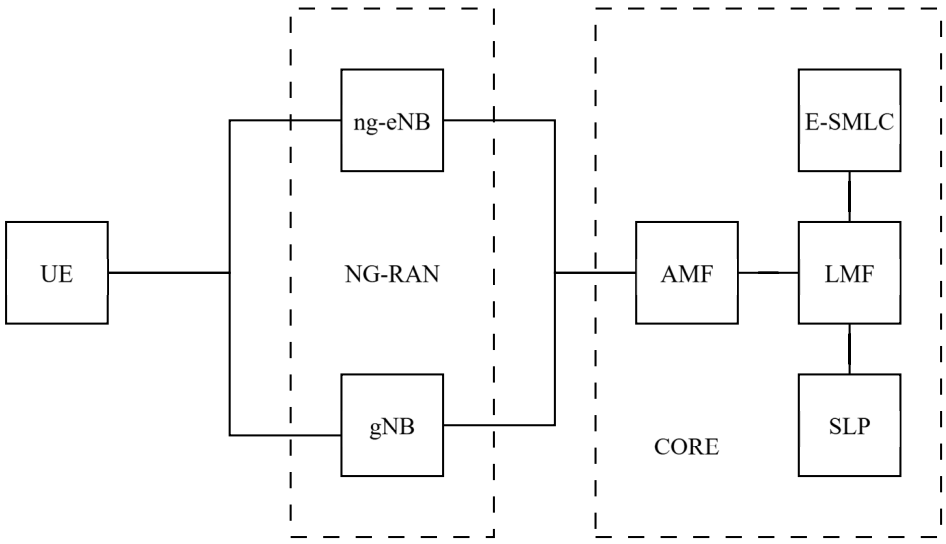

Fig. 2.1: Location services architecture in 5G, from 3GPP TS 38.305

- Next generation evolved nodeB (ng-eNB): is an LTE base station capable of connecting directly to the 5G core network.
- gNB: is a 5G native base station
- New generation radio access network (NG-RAN): is the access element that connect the UE with the 5G core.
- Access and mobility function (AMF): manages access and mobility of the UE.
- Location management function (LMF): manages the procedures related to user location within the 5G network. It is where the PVT engine is located in native 5G networks.
- Evolved serving mobile location center (E-SMLC): Its where the PVT engine is located in legacy LTE networks. Similar to the LMF in 5G networks.
- SUPL location platform (SLP): Manages the protocol called secure user plane location (SUPL) to share localisation information of the UE with the emergency services (E911/E112).

2.1.2 Messages flow for localization services

The architecture in Fig. 2.1 requires the exchange of several messages between its different entities to work. A brief summary of the messages is presented in Fig. 2.2, and the following is a summary of the messages exchanged [3, 40]:

1. The 5G LBS starts with receiving a position request at the AMF by
   (a) An external entity to the core, such as an emergency centre when receiving a distress call.
   (b) The AMF for mobility or cell handover.
   (c) The UE itself, for any internal service or application.
2. The AMF process this request and ask the LMF to start the UE positioning procedure.
3. The LMF configures:
   (a) The UE to make it ready to take the measurements and reporting them back to the LMF.
   (b) The gNBs that are close to the UE with any of the positioning methods compatible with the UE capabilities. The gNB also takes the measurements, if needed, and report them back to the LMF.
4. The LMF estimates the position based on the measurements and methods used and reports the position estimation to the AMF.
5. The AMF replies with the position estimation to the entity that asked.

This approach was designed to maximise the network resources for data services as the main source of income for mobile network operators (MNOs) is this service, not positioning. Another rationale for this design is that the expected use of positioning services is very low [2]. However, this architecture poses scalability challenges in terms of the maximum number of simultaneous users demanding PNT services e.g., in a large distress area where several users are calling emergency services. In addition, this architecture is not defined by 3GPP for NTN scenarios [41, 18]. Therefore, this thesis assumes the PRS is broadcasted and the UE can receive it even if they are not connected (yet) to the network to offer a GNSS-independent system, to help with initial access of the UE. This assumption is in line with what is proposed in the ESA project 5G-LEON (described in Appendix D) as part of this thesis is a contribution to this project.

2.1.3 Positioning technologies in 5G

The following is a list of the different positioning methods developed for the 5G networks in its different releases [2]:

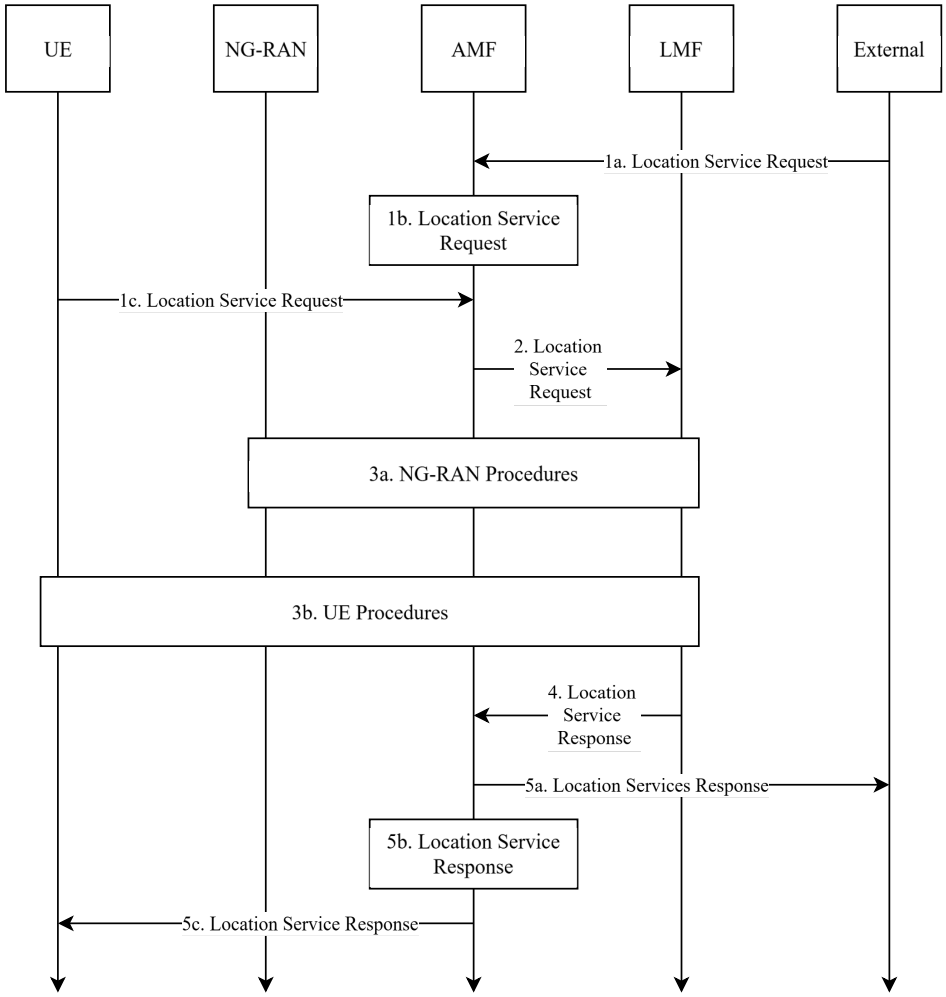

Fig. 2.2: Location service support in 5G, from 3GPP TS 38.305

- Assisted GNSS, it enhances the performance of conventional GNSS by using assistance data provided via the cellular network. This assistance data, such as satellite ephemerids, almanacs, approximate user location, and time reference, are transmitted from the 5G network infrastructure to UE. This significantly reduces the time to first fix (TTFF), improves sensitivity in challenging environments, and enhances positioning accuracy [2].
- Timing-based technologies:
  - Downlink (DL)-time difference of arrival (TDoA): the UE measures the relative arrival-time differences of downlink reference signals from multiple synchronized gNBs. By computing the time differences, hyperbolic curves representing potential UE locations are derived, and their intersection point estimates the UE's position. DL-TDoA requires precise synchronization among base stations but places minimal synchronization burden on the UE, making it suitable for low-complexity devices and scenarios with limited UE processing capabilities [4].
  - Uplink time difference of arrival (UL-TDoA): Multiple synchronized gNBs measure the arrival-time differences of uplink reference signals transmitted from the UE. These measurements also define hyperbolic curves whose intersection provides the UE's estimated location. UL-TDoA also requires strict synchronization among gNBs but imposes minimal complexity and power consumption on the UE, making it advantageous for scenarios involving battery-constrained or low-complexity devices [42].
  - Multi-round trip time (RTT): is based on measuring the round-trip propagation time of radio signals exchanged between the UE and multiple gNBs. Specifically, the UE measures round-trip times by transmitting uplink signals to gNBs and subsequently receiving corresponding downlink responses. By using these round-trip timing measurements, the distances between the UE and several gNBs are computed, allowing trilateration techniques to determine the UE's position. Multi-RTT requires less stringent synchronization among base stations compared to TDoA methods, thereby reducing synchronization complexity at network nodes [4].
- Signal power-based technologies:
  - NR-enhanced cell-ID (ECID): leverages the serving cell's identity combined with enhanced radio measurements, such as reference signal received power

(RSRP), reference signal received quality (RSRQ), and timing advance (TA), to estimate UE position. The NR-ECID method typically provides moderate localization accuracy, relying primarily on cell coverage information complemented by additional radio measurements. Although it does not require precise synchronization among base stations, the positioning accuracy depends heavily on the cell size, density, and radio propagation conditions. NR-ECID is often utilized in scenarios where precise positioning is less critical or as a fallback when other localization methods are unavailable [43].

  - PRS-RSRP: is based on the measurement of received power levels of dedicated PRS transmitted from multiple gNBs. By assessing PRS-RSRP values, the UE or network can estimate the relative proximity or signal strength relationship to various gNBs. Localization using PRS-RSRP typically involves fingerprinting or proximity-based techniques and can serve as a standalone approach or complement other positioning methods. Although PRS-RSRP alone offers moderate accuracy due to signal fluctuations and propagation conditions, its simplicity and low complexity make it practical for network-wide deployment [44].

- Angle-based technologies:

  - DL-angle of departure (AoD): exploits directional beamforming capabilities at gNBs to estimate the UE location. The method involves measuring the angle at which PRSs are transmitted from multiple gNBs toward the UE. By intersecting multiple directional beams originating from distinct gNBs, the UE's position can be computed through triangulation. DL-AoD requires precise antenna-array beamforming and angular resolution at the gNBs, providing improved localization accuracy, especially in dense urban scenarios where LOS conditions prevail [42].
  - Uplink angle of arrival (UL-AoA): relies on measuring the angles at which uplink signals transmitted by UE arrive at multiple gNBs equipped with antenna arrays. Each gNB estimates the direction from which the UE's signals originate, and the intersection of directional lines from multiple gNBs determines the UE's location through triangulation. UL-AoA requires sophisticated antenna arrays and signal processing at the base stations to achieve high angular resolution, providing robust accuracy, particularly when the UE is in clear LOS conditions [42].

- Other positioning candidates:

– Carrier-phase-based positioning: employs measurements of the phase of radio frequency carriers to achieve precise localization of UE. Unlike traditional timing or power-based methods, carrier-phase measurements offer significantly higher accuracy, often reaching centimeter-level resolution, due to the short wavelength of the radio carrier signals. This method calculates position by analyzing phase differences between transmitted and received signals from multiple synchronized gNBs. However, carrier-phase-based positioning requires advanced phase-coherent synchronization, careful handling of integer ambiguity resolution, and is more sensitive to multipath propagation effects, thus typically being suitable for scenarios demanding high-precision positioning [45].

– Phase difference of arrival (PDoA) positioning: involves estimating the UE location by measuring the phase differences of signals received from multiple synchronized gNBs. The method exploits the phase offset introduced by the different propagation distances from the UE to each gNB. Due to the short wavelength of radio signals, even minor differences in distances cause measurable phase shifts, allowing precise localization through hyperbolic trilateration. PDoA positioning offers high accuracy but requires stringent synchronization among base stations, precise phase measurements, and robust algorithms for resolving phase ambiguity, making it suitable for high-precision localization scenarios [46].

– Sidelink positioning: refers to the localization method where UE directly communicates with other UEs using sidelink (device-to-device) signals, independent of gNBs. By measuring signal metrics such as timing differences (e.g., sidelink (SL)-TDoA), received power (e.g., SL-RSRP), or angular information (e.g., SL-angle of arrival (AoA)), UEs collaboratively estimate their relative positions. This approach is particularly beneficial in scenarios where infrastructure-based localization is unavailable or limited, such as vehicular networks, disaster areas, or remote locations. Accuracy depends on the number of devices, signal conditions, and measurement precision between UEs [47].

– Hybrid positioning: combines multiple localization techniques such as A-GNSS, DL-TDoA, UL-TDoA, Multi-RTT, AoA/AoD methods, carrier phase measurements, and signal strength (e.g., PRS-RSRP), to enhance positioning accuracy, reliability, and coverage. By leveraging complementary strengths of different methods, hybrid positioning mitigates individual method limitations like multipath propagation, poor LOS conditions, synchronization errors, or coverage gaps. The fusion of

measurements from multiple sources, using advanced estimation algorithms (e.g., Kalman filtering, particle filtering, or machine learning), results in improved robustness and performance, especially in challenging environments such as urban canyons, indoors, or heterogeneous network deployments [43, 48, 49, 50].

From all the methods described previously, this work is based on DL-TDoA as it is the most suitable for the use in a NTN scenario similar to GNSS [13]. Also this method is the main technique used in the 5G-LEON project (see Appendix D), where this thesis has contributed to.

2.1.4 Use case requirements

Finally, Table 2.1 presents a summary of different use cases that make use of the 5G LBS with their required accuracy extracted from [6, 40, 51].

Table 2.1: Use cases positioning accuracy requirements

Use case	**Expected accuracy** 2σ
Emergency Services (eCall)	$\leq 1\,\mathrm{m}$
Autonomous Driving	$\leq 0.1\,\mathrm{m}$
Industrial Automation	≤ 0.1–$0.5\,\mathrm{m}$
Vehicular Navigation	$\leq 0.5\,\mathrm{m}$
Augmented Reality	$\leq 0.2\,\mathrm{m}$
Drone Navigation	$\leq 0.3\,\mathrm{m}$
Precision Agriculture	$\leq 0.5\,\mathrm{m}$
Smart City Services	$\leq 1\,\mathrm{m}$
Asset Tracking	$\leq 1\,\mathrm{m}$
Network verification	$\leq 100\,\mathrm{m}$

There are other use cases in the literature for LBS services from 5G networks. However, the use cases listed in Table 2.1 are the ones that are normally defined outdoors, as the NTN component for indoor services is still not defined by 3GPP due to the large looses for indoors.

2.2 Localization services with LEO satellites

There are a variety of approaches to implement PNT services with LEO satellites, one approach is to use dedicated LEO-PNT satellites. These satellites and the signals they transmit are operated and designed solely for this purpose [28, 52]. Another approach is to use LEO communication satellites opportunistically for PNT without any adaption of the

communication satellites to support PNT, where all the processing is at the UE side [53]. In between, there is the concept of enhancing LEO communication satellites to support PNT [54, 30, 55, 56].

Besides, in a multi-beam satellite framework, each beam typically offers a single service; consequently, a user illuminated by a beam can only receive one service at a time. Some works in the literature that cover JCAP systems with OFDM signals. However, they suffer from degradation of their communication service due to pilot overhead used for PNT [57, 58, 59]. There is a special case where pilots are embedded in symbols called superimposed pilots; in such cases, the receiver must first demodulate the received signal [60], so it is difficult to multiplex several transmissions. Another limitation of utilising pilots from OFDM for JCAP is that their application in the NTN scenario may result in reduced accuracy [13]. This reduction appears from the loss of orthogonality between subcarriers, which arises from the significant differential delay and differential Doppler effects characteristic of the satellite environment.

Typically, such concepts assume a system design optimized for communications, and the PNT capability is added by incorporating a PNT payload (piggybacking) or by implementing PNT signals in the physical layer (called fused LEO-PNT). As this work is based on fused LEO-PNT JCAP systems, it will narrow the state-of-the-art in these systems.

2.2.1 Fused LEO-PNT

Fused LEO-PNT are those satellite systems that are designed for hybrid operation, data communication and PNT. They provide a specific PNT service on top of the communications service. Due to this hybridization, these systems needs to be optimized to provide the user with relevant signals to be used for positioning apart from the communication service [30].

This thesis explores the performance of a JCAP service using 5G NR signals for communications and DSSS signals for navigation. The academic literature explores the use of 5G signals for PNT, such as [14, 3, 30] where they included a pilot signal PRS dedicated to PNT services as described in the previous section. Then, for hybrid signals, as it is a novel concept, there is little literature as [32, 61].

In general, from the available literature in fused LEO-PNT one can identify the following challenges:

- **Synchronization between satellites**: satellites are expected to share a common time and frequency; therefore, their transmitted signal is synchronised to maintain orthogonality between transmitters (satellites)[13].

- **Accuracy for the orbit determination**. This challenge is not exclusive for fused LEO-PNT. For solving the position equations, knowledge of the transmitter position is needed, and an error in this information leads to an error in the user position estimation. Depending on the user position accuracy requirement, the transmitter position accuracy should follow it [62].

- **Depth of coverage**. This is how the receiver can pick up signals from more than one satellite. It presents the trade-off between the link budget analysis (LBA) and the overlap between beams from different satellites, while keeping the levels of interference between satellites limited [14].

- **Signal multiplexing** The receiver should be able to receive the signal from several satellites at the same time, similar to GNSS. However, communication systems are designed to use an orthogonal approach to reduce interference. And in the case of 5G signals, the large differential delays and Dopplers between satellite transmissions can cause that one signal to interfere with another signal destructively [13].

2.3 Interference for LEO-PNT services

The integration of 5G communication and navigation systems within a unified network holds the promise of revolutionising PNT solutions. However, it also introduces new challenges in signal interference management as mentioned in the previous section. The literature on interference in OFDM systems focusses mainly on terrestrial communication scenarios with single transmitters, addressing inter-symbol interference (ISI) issues in multipath environments as illustrated by [63, 64, 65].

Furthermore, studies such as [66, 67] focus into inter-numerology interference (INI), inter-carrier interference (ICI) and ISI modelling and improvement strategies of INI, ICI, and ISI, again in single-transmitter scenarios.

The complexity increases when multiple transmitters and receivers interact sharing a common band of the spectrum [68]. For terrestrial networks, there are works to address this problem, such as [69], where a FFR scheme is proposed. However, none of these works are intended as a navigation or JCAP system.

In a satellite scenario, the differential delays between signals from different satellites (in the millisecond range) significantly exceed the length of the cyclic prefix (CP) of the waveform (in the microsecond range) [70]. This leads to ISI and ICI at the receiver when it is located in areas where intersatellite beams overlap [70].

Assuming that all gNB are synchronised and transmit positioning pilots synchronously in the same BWP, two strategies are considered in the literature to address interference. In the first strategy, the gNB applies a temporal guard band, called muting, where the muting duration must be long enough for the signal to reach each beam edge [36]. This is used in terrestrial scenarios, as the expected maximum delay is shorter than the CP. However, in a satellite scenario, a muting scheme does not make sense as the large propagation delay will drop the efficiency of the transmission. The second strategy is for satellites to take advantage of the low probability of signal collision due to the large differential delay between satellites [71]. However, this strategy falls when there is a continuous or high usage of the downlink. It is useful only for sporadic or burst packet transmissions.

Therefore, interference models must be developed to accurately evaluate the JCAP system performance. This gap in existing research underscores the need for comprehensive studies that extend beyond traditional interference models to address the complexities of integrated systems in future networks.

Despite some of the advancements seen in interference analysis for 5G NTN scenarios, a critical area remains underexplored as briefly mentioned before: how to model the aggregated interference effects, which are caused by PRS transmissions, within an NTN scenario. Current research does not thoroughly investigate the interference generated by differential propagation delays between satellites, which are considerably longer than the duration of the PRS slot. It is essential for system designers to ensure that interference levels between PRS and data transmissions are minimized, allowing the UE to accurately decode data symbols and extract the estimation of the positioning observables.

This area of study is crucial for the development and optimisation of LEO-PNT services. By meticulously characterising and modelling interference phenomena and understanding their impact on received signals, robust detection algorithms can be developed to effectively mitigate interference effects. This will greatly improve the accuracy and reliability of positioning services, addressing the growing demand for precision in contemporary applications.

2.4 Joint communication and positioning services

The interference challenge described in the previous section originates from the need to multiplex several transmissions within the same resources. This multiplexing can be performed on various signal domains, such as the time, frequency, or code domains, as discussed in [13].

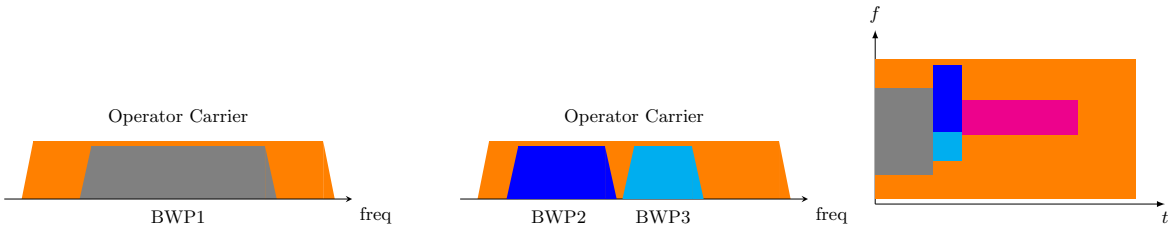

Fig. 2.3: Split in frequency and time of the operator spectrum in different BWP

In 5G the MNO can split its carrier into different BWP to serve different use cases. The multiplexing signal within a BWP is used to minimise interference. A BWP is a dynamic frequency allocation for different services or use cases in 5G terminology [72]. Fig. 2.3 represent how a MNO can split its carrier in different BWP for different services, each with different numerology, bandwidth, and user assignments.

Such allocations are dynamically adjustable on the basis of real-time network demands. For positioning services, a dedicated BWP can be established, allowing multiple satellites to transmit positioning signals simultaneously and to avoid interference with the data service.

Another way to reduce interference is to redesign the waveform used for JCAP. Therefore, the UE can use the new waveform for communication and for PNT in a GNSS-independent approach. In order to establish a JCAP system, data and navigation signals must share resources during transmission, including time, frequency, code, or space.

A JCAP can be achieved using the pilots in the satellite downlink communication signal [55]. This methodology is referenced in the literature by various terms, such as integrated communications and localization (ICAL) [73] or JCAP [74, 75, 76, 77]. The pilots embedded within the data are employed by the UE as sounding signals to extract the observables used to estimate the localisation of the user. Although there is no consensus on the acronym, the fundamental concept remains unchanged: to combine communication and navigation services within the same infrastructure and resources.

In a multi-beam satellite scenario, the designer must meticulously plan the system parameters to minimise interference between beams and services [55]. This planning is critical to ensure efficient communication, maximise system capacity, and provide precise positioning services [78].

The following outlines how interference from the different resources is managed in actual systems and the techniques used to reduce its impact in multi-beam satellites:

- *Frequency reuse with spatial isolation* [79]. Adjacent beams often use different carrier frequencies to minimise interference with typical values of 18-25 dB reduction. This is

similar to the operation of terrestrial cellular networks, where frequencies are reused in nonadjacent cells [80].

- *Beam Shaping and directional antennas* [81]. The satellite uses high-gain and narrow beams that focus signal energy toward specific areas, reducing spillover to adjacent beams. Another alternative is to use adaptive beamforming that dynamically adjusts antenna patterns to optimise coverage and minimise interference with other beams [82] The typical isolation values are about 18-25 dB.

- *Coordinated Beam Scheduling* [78, 83]. The system switches the beams on and off in a controlled manner to serve different areas at different times, reducing simultaneous interference. This also includes traffic management by prioritising and scheduling transmissions according to demand and interference conditions. In this case, aggregate interference levels can rise to 25-30 dB.

In the previous interference management techniques, each beam carries a single service defined by the transmitted waveform, whereas interference between services is managed at the beam level, independent of the waveform used. However, when the network operator wants to offer both services, communications, and navigation, the technique for JCAP is based on the inclusion of pilot sequences within the OFDM grid for localisation purposes [84, 76, 73, 85]. Therefore, the maximum goodput is limited due to the overhead associated with navigation pilots.

To reduce the overhead in OFDM transmission, there is another technique known as superimposed pilots [86, 87, 88, 60]. In this approach, the pilots are combined with the data symbols prior to the OFDM modulation, thereby eliminating the overhead associated with the navigation service. The primary drawback of superimposed pilots is that it requires the receiver to demodulate the signal in order to estimate the channel using these pilots and it works only in a high signal-to-noise ratio (SNR) scenario.

In addition, other works have also considered the integration of DSSS and OFDM within the same waveform [89, 90]. In these works, the data are first modulated using DSSS and subsequently mapped onto the OFDM resource grid (RG). Consequently, the receiver must demodulate the OFDM signal first and then recover the DSSS signal in a cascade manner. Therefore, it cannot exploit the gain of the coherent integration of the DSSS to extract the navigation observables before the OFDM demodulation.

Furthermore, there are some works related to LEO-PNT within the industry [30, 52]. However, these works only show a navigation service from LEO satellites, while other works

provide navigation services through an opportunistic approach [91, 92]. Some initiatives start appearing for JCAP services within LEO satellites such as [14, 55, 32].

In addition, there exists a standardised JCAP system designed by CMMB [61]. This standard is defined for terrestrial video broadcasting services, it uses an OFDM waveform for video broadcasting, and on top of that, it aggregates a navigation signal for localisation purposes. However, this system is standardised for terrestrial services only. Moreover, the work presented in [33] discusses the aggregation of the OFDM signal with the navigation signal, assuming a SIR of 18 dB between the two services. Other recent research [32] proposes a similar strategy to provide navigation and data services by aggregating a DSSS signal onto the OFDM signal; in this case, the author employs a SIR of 16 dB between the data and the navigation signals. Here exists a gap in the literature, the evaluation of the optimal SIR between services while maintaining the requested KPI for the different use cases.

2.5 Summary

This chapter presents the state-of-the-art of localisation services in 5G, emphasising the architecture and positioning techniques standardised by 3GPP. It details various localisation methods, including Assisted GNSS, timing based techniques, signal power based methods, angle-based technologies, carrier phase positioning, sidelink positioning, and hybrid methods. This chapter further categorises the accuracy requirements for use cases, ranging from emergency services needing about 1 m accuracy to autonomous driving requiring precision below 0.1 m.

It also discusses localisation services from LEO satellite, covering different approaches from dedicated LEO-PNT systems to opportunistic and fused solutions. The section elaborates on challenges specific to LEO systems, such as satellite synchronisation, orbit determination accuracy, depth of coverage, and interference modelling. It particularly addresses interference impacts arising from the differential delays of the satellite, Doppler effects, and the challenges posed by integrating the scenario of using the 5G PRS within a NTN environment.

Finally, the chapter outlines JCAP systems, explaining the importance of multiplexing signals within BWP for interference management.

Chapter 3

Suitability of data waveforms for PNT services

The previous chapter presents the state of the art in JCAP systems. This chapter starts with a quantitative comparison between several waveforms proposed for JCAP system such as OFDM, DSSS, hybrid DSSS-OFDM, time-coded orthogonal frequency division multiplexing (TC-OFDM), and orthogonal time frequency space (OTFS), evaluating their suitability based on precision, spectral efficiency, robustness, and complexity. The chapter continues with a quantitative analysis of the most used waveforms that are proposed for JCAP services, OFDM and OTFS, and evaluate its performance as a navigation signal. It uses the AF and CAF as performance assessment tools. Then, it is introduced some of the pilots used in the literature for PNT, including the 5G SSB (used as opportunistic PNT), 5G PRS, the waveform employed by Starlink (also used as opportunistic PNT), and the use of PRS pilots within the OTFS to compare with the OFDM version. Finally, this chapter shows the performance as the delay and Doppler resolutions, and the rejection of other signals using the CAF of these candidate signals. This work is part of the contribution to the technical note presented in the ESA project **SATNEXT Y3.3 LEO-PNT**.

3.1 Waveforms for JCAP

This section presents a qualitative analysis of different waveforms used in the literature for JCAP services.

Positioning accuracy is governed primarily by the received SINR and the effective signal bandwidth, as seen by the CRLB [93, 94]. The 5G PRS, the comb-size parameter (with

Table 3.1: Waveform comparison for joint communication and positioning systems

Waveform	**Reference**	**Accuracy**	**Spectral Efficiency**	**Robustness**	**Complexity**
OFDM	[95, 96]	Moderate (m-level)	High	Moderate-to-Low	Moderate
DSSS	[96]	High (cm-level)	Moderate-to-Low	Very High	High
DSSS-OFDM Hybrid	This work and [32]	High (sub-m-level)	Moderate-to-High	High	High
TC-OFDM	[101, 33]	Moderate-to-High	Moderate-to-High	Moderate	Moderate
CSS	[97, 98]	High (cm-level)	Low-to-Moderate	Very High (Doppler, Multipath)	Moderate-to-High
FHSS	[99]	Moderate	Low-to-Moderate	High (Interference)	Moderate-to-Low
OTFS	[100]	Moderate	High	High	High
DFT-s-OFDM	[102]	Moderate	moderate	High	High

a minimum value of 2) dictates that up to half of the subcarriers carry the PRS sequence, so the actual PRS bandwidth is, at most, 50% of the allocated bandwidth. Besides, PRS transmissions are managed by the 5G LMF and occur in dedicated slots that cannot carry any other data or control information. Consequently, the "overhead" is the fraction of time-slots scheduled for PRS, which varies dynamically with network configuration rather than being a fixed parameter [3].

In this comparison, DSSS-OFDM hybrids achieve the finest ranging accuracy at the cost of greater implementation complexity [32], while conventional OFDM offer high spectral efficiency with only moderate positioning performance [95, 96]. Other waveforms as chirp spread spectrum (CSS) and DSSS both provide centimetre-level accuracy and strong robustness against multipath and Doppler effects, although they sacrifice some spectral efficiency [97, 98]. Besides, frequency hopping spread spectrum (FHSS) delivers moderate precision and robustness with relatively high complexity [99]. And finally OTFS modulation offers moderate accuracy, while the others KPIs are high [100].

As a final overview, Table 3.1 synthesises the KPIs of the principal waveforms investigated in the literature for JCAP. Comparison of each waveform in terms of achievable range accuracy, spectral efficiency, resilience to channel impairments, and implementation complexity, including representative works where their design and performance are detailed.

3.2 Waveforms models

This section shows the mathematical models for two of the most common modulations used in actual communication systems, CP-OFDM used in 5G for example, and OTFS a novel modulation that could be proposed as a waveform for 6G systems for its performance in highly dynamic channels [103].

3.2.1 CP-OFDM

The waveform used in 5G NTN for the communication service is the CP-OFDM as defined in 3GPP TS 38.211 Section 5.3.1, with a bandwidth of BW Hz, divided into N_{scs} subcarriers. The subcarrier spacing is defined as $f_{\text{scs}} = \frac{1}{T_{\text{u}}}$ and a symbol duration of $T_{\text{s}} = T_{\text{u}} + T_{\text{cp}}$, where T_{cp} is the duration of the CP.

Each OFDM slot is composed of 14 symbols, and each OFDM subframe, depending on the numerology used in 5G, will have a different number of slots. However, the duration of the subframe is fixed to 1 ms. The RG is defined as the matrix $\mathbf{A} \in \mathbb{C}^{M \times N_{\text{scs}}}$, where each element $A[m,k]$ is called resource element (RE) and contain a symbol of the constellation used in this specific RE, depending on the upper layers. These RE can be user data, control data or pilots. In this thesis, the user and control data will be assumed to be random QPSK symbols, while the pilots depend on their definition. Some of the pilots used for this evaluation are defined in the next section.

The model in (3.1) represents the baseband transmitted signal as an OFDM signal.

$$x(t) = \sqrt{P_{\text{TX}}} \sum_{m=0}^{M-1} \sum_{k=0}^{N_{\text{scs}}-1} A[m,k] e^{j2\pi k f_{\text{scs}}(t - mT_{\text{s}})} g\left(t - mT_{\text{s}}\right), \tag{3.1}$$

where the CP window is defined as

$$g(t) = \mathbf{1}_{[-T_{\text{CP}}, T_{\text{u}})}(t) = \begin{cases} 1, & -T_{\text{CP}} < t < T_{\text{u}}, \\ 0, & \text{otherwise.} \end{cases}$$

The use of the $g(t)$ rectangular CP extended pulse is assumed because it reduces the computational complexity (compared to other pulses) and maintains the orthogonality between subcarriers; therefore, the interference is due to channel dynamics only. The transmitted signal $x(t)$ has an average power level of P_{TX}. This power level is fixed at the transmitter high power amplifier (HPA) to guarantee the minimum performance for users at the beam edge. This approach assumes, similar to GNSS, a uniform equivalent isotropic radiated power (EIRP) across the satellite beam.

3.2.2 OTFS

In high Doppler channel scenarios, channel characteristics vary rapidly, leading to a reduced channel coherence time [103]. The coherence time is inversely proportional to the variability of channel coefficients. OFDM has traditionally been the preferred modulation scheme

in wireless communications. However, in high-Doppler environments, OFDM presents significant drawbacks, including the necessity for frequent channel measurements and susceptibility to ICI. Specifically, these limitations are:

- **Frequent pilot transmission:** OFDM transmits data in the time-frequency (TF) domain, assigning each data symbol to an orthogonal frequency subcarrier. Pilots, essential for channel estimation, occupy portions of the bandwidth and must be transmitted frequently to cope with rapidly changing channel conditions, thus reducing the achievable data throughput.
- **Inter-Carrier Interference (ICI):** OFDM suffers from ICI in high-Doppler multipath environments. Different relative velocities between scatterers produce varying frequency offsets, disrupting the frequency domain orthogonality crucial for interference free symbol detection.

To address these challenges, OTFS modulation has been proposed, which transmits data in the Delay-Doppler (delay-Doppler (DD)) domain [103]. This representation explicitly captures scatterers characterized by their delay (propagation delay) and Doppler shift (relative speed to the receiver). Under the assumption of a limited number of scatterers, the resulting DD domain channel matrix is typically sparse, significantly enhancing channel estimation and equalization efficiency. Moreover, when scatterers maintain constant velocities, the channel remains quasi-stationary in the DD domain, substantially reducing the necessity for frequent pilot transmissions and thus improving effective throughput.

Given its robustness against rapid channel variations, OTFS is increasingly considered a strong candidate for future 6G modulation schemes [104], especially to fulfill high-mobility scenarios. Recent research as [105] explores the feasibility of multiplexing navigation and communication signals using OTFS. Their proposed method involves differential power allocation between navigation and communication signals at the transmitter, coupled with successive interference cancellation (sequential interference cancellation (SIC)) at the receiver to effectively separate the two signal types.

The input-output system model employing OTFS modulation. Mathematically, the baseband transmitted signal is expressed as:

$$x(t) = \sqrt{P_{\mathrm{TX}}} \sum_{k=0}^{N-1} \sum_{l=0}^{M-1} \sum_{n=0}^{N-1} \sum_{m=0}^{M-1} A[m,n] e^{j2\pi\left(\frac{nk}{N} - \frac{ml}{M}\right)} g(t-kT) e^{j2\pi l f_{\mathrm{scs}}(t-kT)} \tag{3.2}$$

where $\sqrt{P_{\mathrm{TX}}}$ denotes the transmission signal power, k indexes Doppler bins, l indexes delay

bins, n represents symbols in the time-frequency domain, and m identifies subcarrier numbers. The term $A[m, n]$ represents the pilot symbol in the time-frequency domain, and $g(t - kT)$ is the pulse shaping function, commonly implemented using a rectangular (rect) function analogous to the OFDM case.

3.3 Candidate pilots for observable estimation

Now, within both modulations, the different pilots that can be included within the RG. The different pilots selected for the analysis and their rationale are the following.

- 5G NR SSB. These pilots are broadcast and used in the literature as a signal of opportunity (SoO) for positioning [45].
- Starlink waveform OFDM, using the synchronisation pilots primary synchronization signal (PSS) and secondary synchronization signal (SSS). This is a signal that is actually in use by the Starlink constellation; therefore, it is interesting to analyse as candidate for SoO [106].
- 5G NR PRS. These pilots are already used for terrestrial positioning in 5G networks [4].
- 5G NR PRS mapped into a OTFS RG. This case its used the PRS sequence within the delay/Dopler grid. This novel modulation is designed for high mobility scenarios; therefore, the NTN is an example of high mobility of the transmitters, and the inclusion of the PRS serves as a comparison with the previous 5G PRS.

3.3.1 OFDM. 5G synchronization signal block

To provide frame timing to the UE, a gNB broadcast synchronization signal (SS) on pre-specified symbol numbers, which are known at the UE. The UE can obtain the frame start time by acquiring the SS. An SS includes a PSS and a SSS, which provide symbol and frame timing, respectively.

The PSS and SSS are transmitted along with the physical broadcast channel (PBCH) signal and its associated demodulation reference signal (DMRS) on a block called SS/PBCH block. The SS/PBCH block consists of four consecutive OFDM symbols and 240 consecutive subcarriers. Fig. 3.1 shows an SS/PBCH block structure.

The frequency location of the SS/PBCH block depends on the high-level signaling of 5G. The SS/PBCH block has a typical periodicity of 20 ms and is transmitted numerous times on

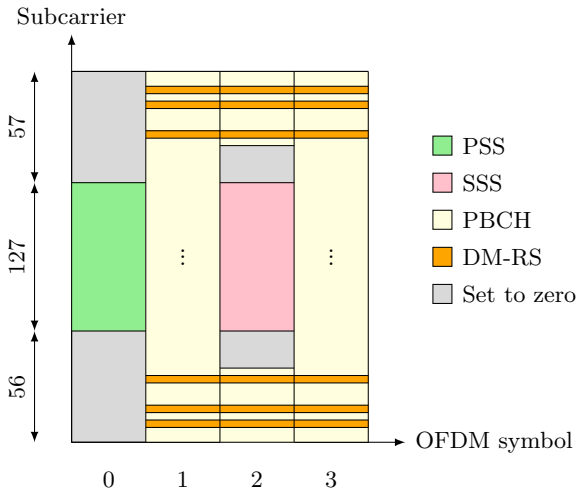

Fig. 3.1: 5G Synchronization Signal Block

one of the half-frames, which is also known as an SS / PBCH burst. Each SS/PBCH block can be transmitted in a different direction using beamforming techniques. The numbers of OFDM symbols on which the SS/PBCH block starts and the number of SS/PBCH blocks per frame depend on the numerology and transmission frequency f_c of the signal [107].

The PSS and SSS are two orthogonal maximum length sequences (m sequences) of length $N_{SS} = 127$, which are transmitted on contiguous subcarriers. The PSS is transmitted in one form of three possible sequences, each of which corresponds to an integer representing the sector ID of the gNB, i.e., $N_{ID}^{(2)} \in 0, 1, 2$

The SSS is transmitted in one of 336 possible forms, each of which maps to an integer representing the gNB group identifier, i.e., $N_{ID}^{(1)} \in 0, \ldots, 335$. The values of $N_{ID}^{(2)}$ and $N_{ID}^{(1)}$ define the physical cell identity of gNB according to

$$N_{ID}^{Cell} = 3N_{ID}^{(1)} + N_{ID}^{(2)} \tag{3.3}$$

Detailed instructions to generate the PSS and SSS sequences are provided in [108].

To determine the position of a UE, multiple downlink reference signals can be utilised by the UE. However, broadcast reference signals, such as the previously described, PSS and SSS, should be avoided for position estimation due to the following limitations [109]:

- These reference signals are not capable of detecting a sufficient number of neighbour access network nodes gNBs because of the interference from the adjacent cells when signals from multiple cells collide in both the time and frequency domains. Due to

this interference, signals from nearby cells shadow the weak signals from far away cells, causing difficulty for the UE to detect far away cells or gNBs.

- These reference signals also have weak correlation properties due to low RE density and their RE pattern might not spread across all subcarriers in the frequency domain.

3.3.2 OFDM. Starlink signal

Several works have been done for opportunistic positioning based on Starlink signals such as [31, 110, 111, 106]. In order to use these signals for positioning, it is needed to have a model of them. The work in [112, 106] shows the modulation used and its structure.

The channel layout is composed of $8\times$ F_s MHz channels for the Starlink Ku band downlink allocation. Each OFDM The Starlink frame consists of 302 intervals of length $T_{sym} = 4.4\mu$ s plus a frame guard interval T_{fg}, for a total frame period of $T_f = 1/750$ s. Each frame begins with the PSS, which is natively represented in the time domain, followed by the SSS, which is formatted as a standard 4QAM OFDM symbol. Each frame ends with the CM1SS followed by the CSS and the frame guard interval. A subsequent frame may be present immediately or not, depending on user demand.

The known information symbols of the SSS and CSS allow a receiver to perform channel estimation across all subcarriers at the beginning and end of each frame, permitting within frame interpolation. The purpose of CM1SS, which arrives just before CSS and is only partially populated with information symbols that repeat from frame to frame, is unclear, but its predictable elements are, without a doubt, also useful for channel estimation.

The PSS and SSS sequences estimated in [112] are used to estimate the time. The Starlink signal can be generated following the work in [105].

3.3.3 OFDM. 5G positioning reference signal

3GPP has reintroduced from LTE a reference signal known as PRS in Release 16 of the 5G specification [2]. This signal exhibits a higher RE density and improved correlation properties compared to existing reference signals such as PSS/SSS, owing to the implementation of the diagonal or staggered PRS RE pattern.

The PRS sequence generation follows a mathematical formulation similar to other reference signals in the system, such as the DMRS and the channel state information (CSI). The PRS is generated using a Gold sequence. The Gold sequence is a pseudorandom sequence that can be efficiently generated by combining two maximum-length sequences

(m-sequences). These m-sequences are produced by Linear Feedback Shift Registers linear feedback shift registerss (LFSRs), each defined by a generator polynomial.

A Gold sequence, denoted as $c(n)$, is defined by combining two m-sequences, $x_1(n)$ and $x_2(n)$, as follows:

$$c(n) = x_1(n) \oplus x_2(n + N_c), \tag{3.4}$$

where $c(n)$ is the Gold sequence, $x_1(n)$ and $x_2(n)$ are two m-sequences, N_c is a cyclic shift applied to $x_2(n)$ to generate different sequences for different gNBs or PRS configurations.

The m-sequences $x_1(n)$ and $x_2(n)$ are generated using primitive polynomials of degree 31, corresponding to the taps of a 31-stage LFSR. The recursive relations for generating these sequences are the following.

$$x_1(n + 31) = (x_1(n + 3) \oplus x_1(n))\text{mod } 2, \tag{3.5}$$

$$x_2(n + 31) = (x_2(n + 3) \oplus x_2(n + 2) \oplus x_2(n + 1) \oplus x_2(n))\text{mod } 2, \tag{3.6}$$

The choice of these specific feedback taps ensures that the sequences have a maximum length and are thus pseudorandom. The initial states of the m-sequences are crucial for generating different PRS sequences for different base stations. The initial states are determined on the basis of the cell ID ($N_{\text{ID}_{\text{cell}}}$), PRS ID, and other configuration parameters defined in the 3GPP specification TS 38.211. For $x_1(n)$, the initial state $x_1(0), x_1(1), \ldots, x_1(30)$ is typically set to a predefined value that is not all zeros. For $x_2(n)$, the initial state $x_2(0), x_2(1), \ldots, x_2(30)$ is a function of the cell ID and PRS configuration, ensuring that each cell can transmit a unique PRS.

The shift N_c is determined by the physical cell ID (PCI) or the PRS occasion index. This ensures that the PRS sequences transmitted by different gNBs or for different PRS occasions are unique, reducing the likelihood of interference between different PRS signals.

The sequence $c(n)$ is then mapped onto the RG in accordance with *3GPP TS 38.211 Section 7.4.1.7.3* [108] as $\mathbf{A}_i \in \mathbb{C}^{M \times N_{\text{SCS}}}$, where M represents the OFDM symbols and N_{SCS} is the total number of subcarriers of the RG.

Once the sequence is generated, there are several approaches to populate the RG when there is more than one transmitter. Here will show two of them that represent the worst and the best case in terms of interference with their limitations.

The worst case is shown in Fig. 3.2, where the PRS sequence is located within the same RE for all transmissions. The receiver will detect what PRS has been transmitted due to the correlation gain. The reader can see that this approach will have the worst performance in

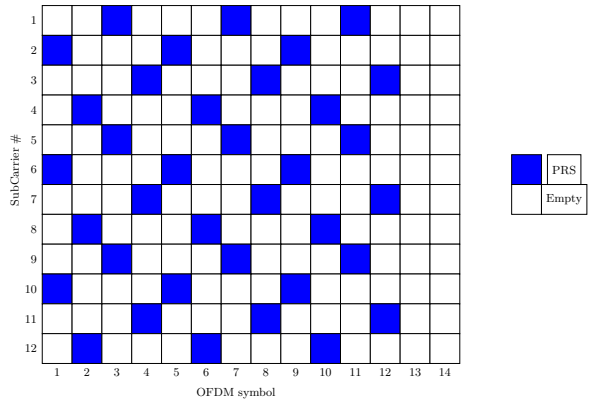

Fig. 3.2: 5G PRS Resource Grid allocation. Size 1 Resource Block × 1 Slot. All PRS share the same distribution

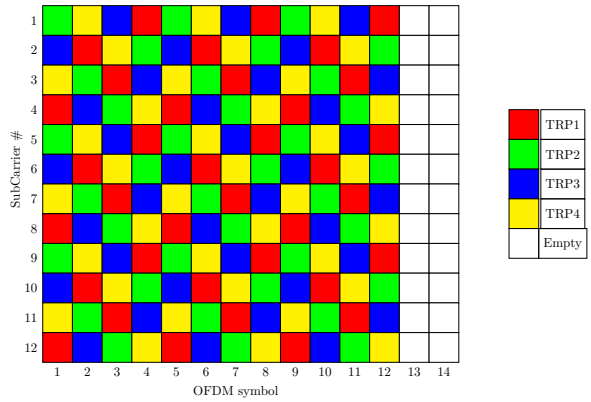

Fig. 3.3: 5G PRS Resource Grid allocation. Size 1 Resource Block × 1 Slot

terms of interference as all transmissions share the same resources. However, from a network management perspective, this is the easiest approach to use, as all gNB transmit their PRS in the same RE.

On the other hand, an option that reduces interference between transmissions is to distribute each PRS in different RE as seen in Fig. 3.3. However, this approach requires a good coordination/synchronisation between the gNBs to be sure there is no overlap in the RG for all transmitters.

3.3.4 OTFS. Positioning reference signal

The last waveform to evaluate is the PRS mapped into the DD as the input of the OTFS modulation as in (3.2). This will serve as a comparison between the OFDM and OTFS transmitting the same sequence.

3.4 Data waveform evaluation for PNT observable estimation

This section evaluates the different signals used for position estimation by using the AF defined by (3.7).

$$\chi_{xx}(\tau, \upsilon) = \int_{-\infty}^{+\infty} x(t)x^*(t-\tau)e^{j2\pi\upsilon t}dt \tag{3.7}$$

This function is used to extract the KPI to evaluate the waveform capabilities in terms of delay and frequency resolution and their robustness in the presence of interference / noise.

The ideal AF is a delta function in both domains, mathematically represented as $\chi_{xx}(\tau, \upsilon) = \delta(\tau - \tau_i)\delta(\upsilon - \upsilon_i)$. However, this function is not physically realisable [103], therefore, the non-idealities in the AF come from the waveform design. Then, using AF one can get insights of the waveform in terms of:

1. **Time-Frequency Duality**: The shape of the ambiguity function in time is related to the shape in frequency and vice versa. If a signal is narrow in time, its ambiguity function will be broad in frequency.

2. **Resolution**: The peak of the ambiguity function indicates the best time and frequency match between the transmitted and received signals. The width of the main lobe around this peak indicates the resolution capabilities of the signal.

3. **Sidelobes**: These are secondary peaks in the ambiguity function that can interfere with the main peak and are undesirable as they interfere with other signals that are close in the delay/Doppler domain.

Furthermore, the CAF is defined by (3.8) and will be used later in this thesis as part of the acquisition step in a receiver, between a local copy of the signal, and the received signal.

$$\chi_{xy}(\tau, \upsilon) = \int_{-\infty}^{+\infty} x(t)y^*(t-\tau)e^{j2\pi\upsilon t}dt \tag{3.8}$$

3.4.1 Theoretical ambiguity function for an OFDM waveform

Starting with the OFDM signal model in (3.1)

Also write

$$x^*(t-\tau) = \sqrt{P_{\mathrm{TX}}} \sum_{n=0}^{M-1} \sum_{l=0}^{N_{\mathrm{scs}}-1} A^*[n,l]e^{-j2\pi l f_{\mathrm{scs}}(t-\tau)} g\left(t - \tau - nT_{\mathrm{s}}\right), \tag{3.9}$$

The AF for a CP-OFDM is obtained by substituting (3.1) and (3.9) into (3.7) as

$$\chi_{xx}(\tau,\upsilon) = P_{\mathrm{TX}} \sum_{m,n=0}^{M-1} \sum_{k,l=0}^{N_{\mathrm{scs}}-1} A[m,k]A^*[n,l]e^{j2\pi l f_{\mathrm{scs}}\tau} I_{mn}(\tau,\Omega_{kl}), \tag{3.10}$$

where

$$\Omega_{kl} \triangleq \upsilon + \frac{k-l}{T_{\mathrm{u}}}$$

and the windowed exponential integral is

$$I_{mn}(\tau,\Omega) \triangleq \int g(t-mT_{\mathrm{s}})g(t-\tau-nT_{\mathrm{s}})e^{j2\pi\Omega t}dt.$$

The integrand is nonzero only in the overlap interval.

$$I_{mn}(\tau) = [mT_{\mathrm{s}} - T_{\mathrm{CP}}, mT_{\mathrm{s}} + T_{\mathrm{u}}) \cap [\tau + nT_{\mathrm{s}} - T_{\mathrm{CP}}, \tau + nT_{\mathrm{s}} + T_{\mathrm{u}}),$$

whose length is

$$W_{mn}(\tau) = T_{\mathrm{s}}\Lambda\left(\frac{\tau}{T_{\mathrm{s}}} + (n-m)\right)$$

with the triangular function defined as $\Lambda(u) = \max\{1-|u|, 0\}$. When $W_{mn}(\tau) > 0$ the midpoint of the overlap is

$$\mu_{mn}(\tau) = \frac{(m+n+1)T_{\mathrm{s}} + \tau + T_{\mathrm{u}} - T_{\mathrm{CP}}}{2}$$

and a standard exponential integral gives

$$I_{mn}(\tau,\Omega) = e^{j2\pi\Omega\mu_{mn}(\tau)} W_{mn}(\tau)\mathrm{sinc}\left(\Omega W_{mn}(\tau)\right)$$

Combining the above the analytical form of the OFDM AF is

$$\begin{aligned}\chi_{xx}(\tau,\upsilon) = P_{\mathrm{TX}} \sum_{m,n=0}^{M-1} \sum_{k,l=0}^{N_{\mathrm{scs}}-1} & A[m,k]A^*[n,l]e^{j2\pi l f_{\mathrm{scs}}\tau} \\ & \times \left[T_{\mathrm{s}}\Lambda\left(\frac{\tau}{T_{\mathrm{s}}} + (n-m)\right)\mathrm{sinc}\left(\left[\upsilon + \frac{k-l}{T_{\mathrm{u}}}\right] T_{\mathrm{s}}\Lambda\left(\frac{\tau}{T_{\mathrm{s}}} + (n-m)\right)\right)\right. \\ & \left. \times \exp\left\{j2\pi\left(\upsilon + \frac{k-l}{T_{\mathrm{u}}}\right)\frac{(m+n+1)T_{\mathrm{s}} + \tau + T_{\mathrm{u}} - T_{\mathrm{CP}}}{2}\right\}\right]\end{aligned} \tag{3.11}$$

Remarks from (3.11):

- Delay support: for each pair (m, n), the contribution is non-zero only when $|\tau + (n - m)T_{\mathrm{s}}| < T_{\mathrm{s}},$, that is, τ lies in a width-$2T_{\mathrm{s}}$ window centred at $(m - n)T_{\mathrm{s}}$. In particular, the terms $m = n$ (the same symbol) produce the familiar triangular support $|\tau| < T_{\mathrm{s}}$.
- Doppler structure: the Doppler argument appears as $\upsilon + (k-l)/T_{\mathrm{u}}$; the same-subcarrier terms $k = l$ produce a mainlobe $\mathrm{sinc}(\upsilon W_{mn})$, while inter-subcarrier terms are shifted in Doppler by integer multiples of T_{u}.

3.4.2 Theoretical ambiguity function for an OTFS waveform

Starting with the OTFS signal model as a Heisemberg transform:

$$x(t) = \sqrt{P_{\mathrm{TX}}} \sum_{n=0}^{N-1} \sum_{m=0}^{M-1} X[m, n] e^{j2\pi m f_{\mathrm{scs}} t} g(t - nT), \tag{3.12}$$

where

$$X[m, n] = \frac{1}{\sqrt{MN}} \sum_{d=0}^{M-1} \sum_{l=0}^{N-1} A[l, d] e^{j2\pi \left(\frac{md}{M} - \frac{nl}{N}\right)}. \tag{3.13}$$

Now, using the definition of AF, we substitute (3.12) into (3.7) as

$$\begin{aligned} \chi_{xx}(\tau, \upsilon) =& P_{\mathrm{TX}} \sum_{n,n'=0}^{N-1} \sum_{m,m'=0}^{M-1} X[m, n] X^*[m', n'] \\ & \times e^{j2\pi(m' f_{\mathrm{scs}} \tau + \upsilon n T)} A_g\left(\tau + (n' - n)T, \upsilon + (m - m') f_{\mathrm{scs}}\right), \end{aligned} \tag{3.14}$$

where the pulse ambiguity function has been defined as

$$A_g(\tau, \upsilon) \triangleq \int_{-\infty}^{+\infty} g(t) g^*(t - \tau) e^{j2\pi\upsilon t} dt. \tag{3.15}$$

In the case of a rectangular pulse, it leads to

$$A_g(\tau, \upsilon) = \begin{cases} e^{j2\pi\upsilon \frac{T+\tau}{2}} (T + |\tau|) \mathrm{sinc}(\upsilon(T + |\tau|)), & |\tau| < T, \\ 0, \qquad \text{otherwise} \end{cases} \tag{3.16}$$

With a rectangular pulse, A_g has large sidelobes (sinc in Doppler and triangular in delay), so lattice-shift leakage is unavoidable and appears directly in χ_{xx} as elevated sidelobes. Both OTFS and OFDM yield AFs composed of shifted copies of A_g along a TF lattice. In OFDM

the data live natively in TF, so AF structure aligns directly with subcarrier differences $(k-l)$ and symbol differences $(m-n)$. In OTFS, the TF coefficients $\mathbf{X}$ are coherent mixtures inverse symplectic finite Fourier transform (ISFFT) of DD data. This is precisely the mechanism in OTFS that spreads each DD symbol over TF to gain robustness against doubly-selective channels.

3.4.3 Empirical ambiguity function evaluation for the selected waveforms and pilots

From (3.11) it is clear that the shape of the AF will depends on the pilots A_i and their arrangement in the RG, and also there is a sinc function and exponential functions that will enlarge the ideal AF. Fig. 3.4 shows a 3D visual representation of the AF for the different waveforms. The axis are normalized with the symbol time T_{Symbol} in the Doppler axis, and with the signal bandwidth in the delay domain to make a fair comparison between the signals. There are some differences between the different waveform. For example, the Starlink signal has a very wide lobe in the Doppler axis, while the others are much narrower. Another difference are the number of peaks, their distance to the main peak, and how high are they compared to the main peak. In the 5G PRS, SSB and OTFS there are one large peak and two secondary lobes.

To have a better comparison of the different waveforms AF it has been created two cuts on the 3D plots, one in the delay axis in Fig. 3.5 when the Doppler is 0 Hz and another in the Doppler axis in Fig. 3.6 when the delay is 0 s.

Then, it is compared also the AF with the CAF in Fig. 3.7 and Fig. 3.8. They represent an example of the AF and CAF when $\mathbf{A}^{(i)}$ is the Resource Grid with the PRS, the SSB, the Starlink transmission of the PSS and SSS, or the PRS transmitted using OTFS.

For the comparison between waveforms the following KPI are used:

- Sequence gain. This parameter compares the signal of interest power as the maximum on the AF with the maximum power of the CAF. This KPI gives an idea on how good the waveform is able to reject other signals with the same power. In the GNSS literature is called correlation gain. The higher this gain is, the detector at the receiver will detect the peak between the noise and interference.

- Vertical distance between secondary lobes (in delay and Doppler). This KPI measures the performance of the waveform AF as its ability to have a distinct peak in the domain selected. As seen in the previous Fig. 3.5 and Fig. 3.6 each waveform have different lobes sizes and this could impact the later detection and probability of false alarm at

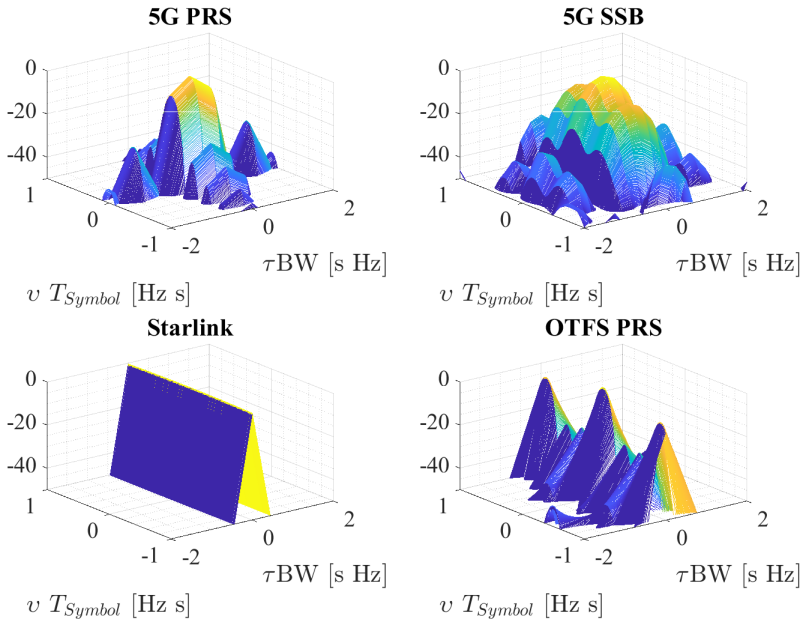

Fig. 3.4: Comparison of the Ambiguity Function for different waveforms

the receiver. In a scenario with high noise and interference, the larger this vertical distance is the better for the receiver detector to not miss-detect the secondary lobe as the main lobe.

- Main lobe width. This KPI measures the resolution achievable given a certain waveform. As noise and interference will impact the detection at the receiver, the narrower the peak, the more accurate estimation can be achieved. It is measured between the peak value of the lobe and its wide at -20 dB, Fig. 3.5 and Fig. 3.6 shows a comparison between different waveforms.

Table 3.2 shows a summary of the different KPIs for the different waveform analysed. From Table 3.2 the reader can evaluate the capabilities of one signal or another to estimate an observable. It can be seen that Starlink gives the best resolution for delay estimation (due to it wide bandwidth of 250 MHz), while it is not recommended for Doppler measurements. On the other hand, the PRS gives similar performance in the delay resolution in both modulations OFDM and OTFS. Both modulations offer similar gain against interference signals, while the worst signal for this is the SSB. The OTFS transmitting the PRS offer the best performance for delay estimation while maintaining the same bandwidth than OFDM. However, for Doppler estimations the best resolution is given by OFDM.

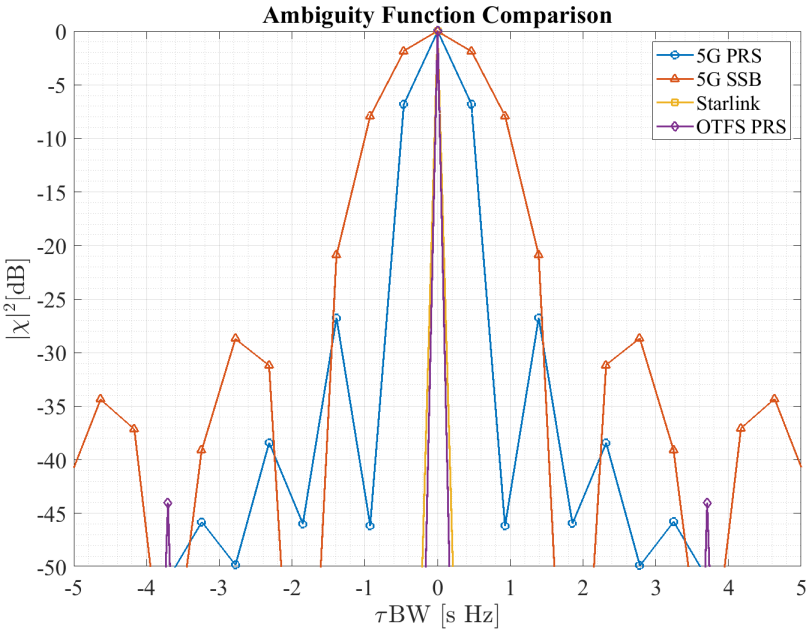

Fig. 3.5: Delay cut ($\upsilon = 0$ [Hz]) of the AF for different waveforms.

Table 3.2: Summary of waveform KPIs for observable estimation

Waveform	Gain respect to the CAF [dB]	Secondary lobe AF [dB]	Δ delay [ns]	Δ Doppler [kHz]	Resolution delay [ns]	Resolution Doppler [kHz]
5G PRS	43.15	26.74	390	2.48	520	1.13
5G SSB	34.56	28.69	781	2.96	781	1.57
Starlink	56.37	20.04	533	N/A	8.33	¿30
OTFS PRS	44.06	39.49	3125	6.88	260	1.16

Moreover, it has been computed the maximum value of the CAF for each PRS sequence (i.e., 1008 possible sequences) and show it in Fig. 3.9. This CAF is used to evaluate how the interference from other sequences has an impact in the detection of a specific PRS sequence.

Finally, Table 3.3 presents the mean and standard deviation of the interference power from the possible combinations. It serve to have an estimation of the interference rejection from other PRS transmissions.

3.5 Summary

This chapter focuses on a detailed waveform analysis for PNT services, evaluating several modulation schemes and pilot signals such as 5G PRS, 5G SSB, Starlink synchronization signals, and OTFS modulation. Using the AF and CAF, the performance of each waveform

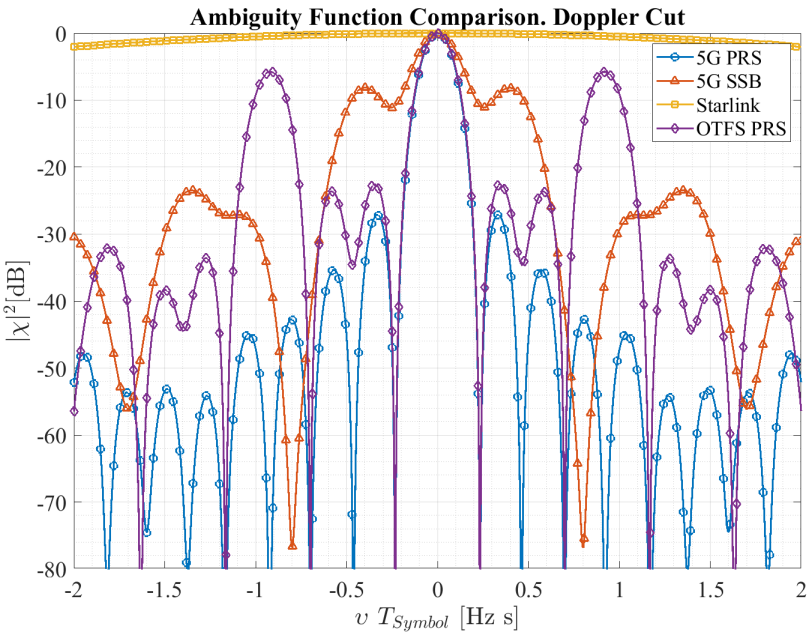

Fig. 3.6: Doppler cut ($\tau = 0$ [s]) of the AF for different waveforms.

Table 3.3: Summary of waveform KPIs for observable estimation

KPI	Value
CAF max mean for all PRS combinations [dB]	27 dB@5MHz -60 dB@30MHz
CAF max std for all PRS combinations [dB]	15 dB for both configurations
AF Sidelobe Level (SLL) [dB]	26 dB

was characterized in terms of resolution capabilities, interference robustness, and detection potential under various Doppler and delay conditions. The analysis revealed that waveform like OTFS offered improved robustness and accuracy in high-mobility scenarios, significantly outperforming traditional OFDM-based signals, particularly in the context of delay resolution and Doppler resilience.

The results indicated clear performance trade-offs: while OFDM-based signals like the 5G PRS provide moderate resolution suitable for typical terrestrial applications, they exhibit limitations when applied to NTN due to significant Doppler and delay variations inherent to satellite communications. By contrast, OTFS signal demonstrated superior resilience to such channel impairments, maintaining robust performance even under highly dynamic NTN conditions. The Starlink waveform, despite its excellent delay resolution due to its wide bandwidth, exhibited poor Doppler estimation performance, suggesting its limited

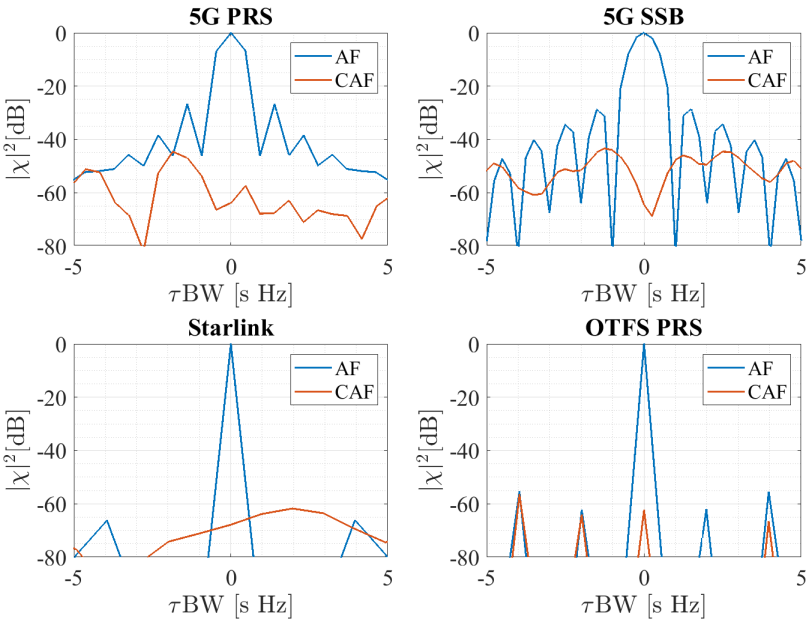

Fig. 3.7: Delay cut ($v = 0$ [Hz]) of the AF and CAF for different waveforms.

applicability in scenarios requiring precise velocity estimation.

These findings highlight the critical importance of waveform selection in NTN environments, directly influencing interference management and system design. Building upon these conclusions, Chapter 4 further explores interference modelling for the 5G PRS, establishing empirical statistical models tailored to NTN scenarios. This modelling approach directly addresses the challenge identified in this regarding interference impact and waveform reliability, thus enabling precise link-budget analysis and optimal waveform configuration for robust satellite-based positioning services.

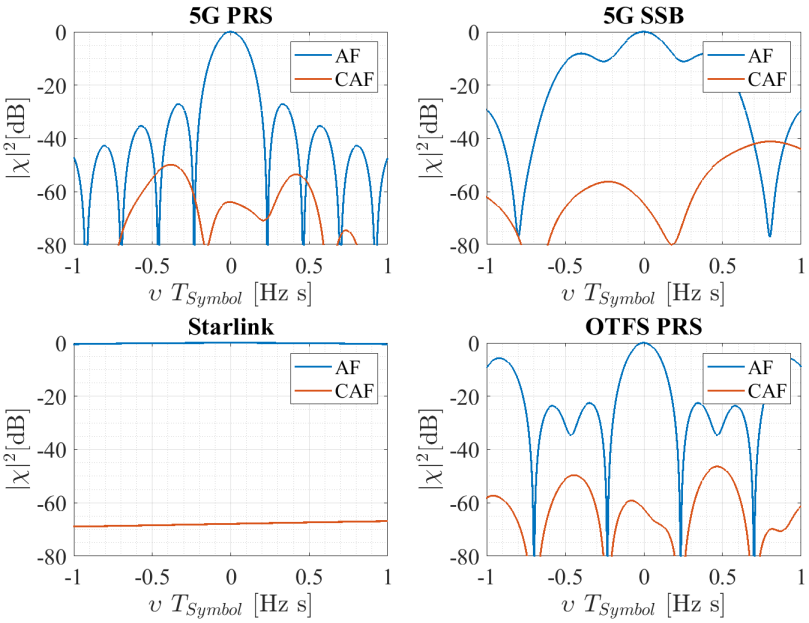

Fig. 3.8: Doppler cut ($\tau = 0$ [s]) of the AF and CAF for different waveforms.

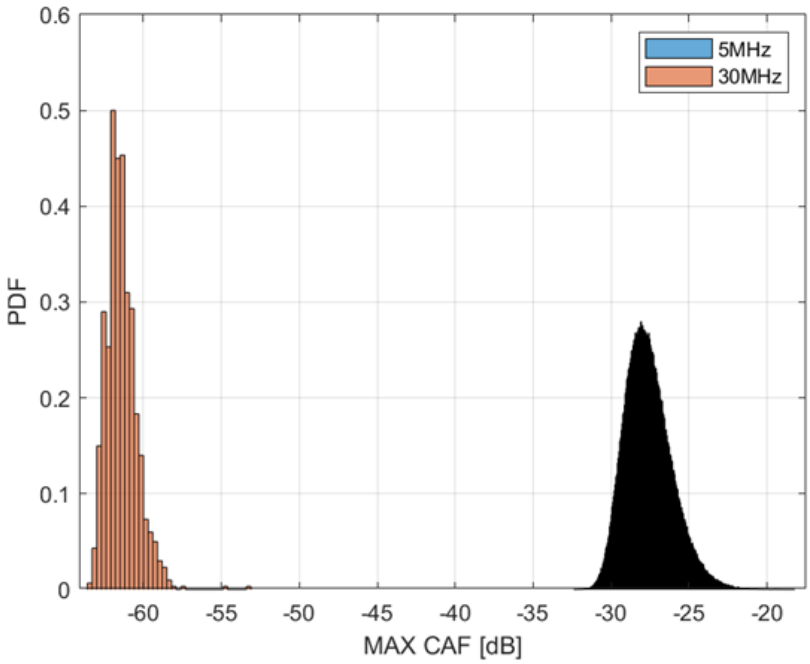

Fig. 3.9: PDF of the maximum value of the CAF for two configurations of the PRS. The 5 MHz includes all possible combinations of ID, while the 30 MHz only 1000 combinations due memory limitations.

Chapter 4

Interference model extraction for the positioning reference signal in an NTN scenario

This chapter shows an empirical model for the interference generated by the multiple reception of PRS in an NTN scenario. This model is extracted from a synthetic dataset generated by simulating several satellite passes over several positions and extracting each received signal power from each satellite in LOS with the UE. It uses a similar approach seen in the previous chapter to evaluate the performance of the PRS in 5G NTN. This work is published in the open journal of the Communications Society (OJ-COMS) as [113], in the international conference on acoustic, speech and signal processing (ICASSP) [114] and the model developed has been used in a specific scenario for LEO-PNT presented in the conference paper [115].

4.1 Scenario for 5G satellite positioning

This section outlines the framework and scenario definition for PNT service provision via 5G NTN using the PRS. It involves a detailed examination of the assumptions, simplifications, and the reasoning behind them. The proposed model requires that the signal from at least four distinct NTN gNBs, similar to GNSS, reaches the user terminal.

In GNSS systems, all satellites carry on board a very precise atomic clock. These clocks are used to maintain a common clock reference in the system, and the user is notified of any deviation through the navigation message. In this particular scenario, it is assumed that all satellites are perfectly synchronized, as solving this challenge is beyond the scope of this

work. An initial approach is presented in [30].

In this study, is adopted an Earth-moving beam configuration as defined in 3GPP TR 38.821, where the satellite beam moves along with the satellite, as the interference will be analyzed for single snapshot receivers. For multibeam satellites, the satellite implements pre-compensation at a reference ground point for each beam, effectively reducing the maximum delay/Doppler range experienced by the signal. Consequently, a single-beam satellite represents a worst-case scenario from this perspective, which is focused this analysis.

Nowadays, beam overlapping can be achieved by massive constellations such as Starlink (in this case, it is assumed a single shell where all satellites are at the same altitude). There are examples in the literature, such as [116], on how to achieve this beam overlapping for a data service.

In this study, it is implemented the PRS multiplexing design used for terrestrial applications [6], as depicted in Fig. 3.3. This design facilitates the transmission of multiple PRS signals within a single OFDM slot, whereby the empty REs left by one transmitter, due to the steps of the subcarrier ("Comb Size" parameter), are used by another gNB for its PRS allocation.

Unlike the terrestrial channel, the NTN channel experiences larger differential delays and Doppler shifts. Therefore, this analysis focuses on the interference generated by different transmissions in this scenario, where each satellite's signal travels through a wireless channel that can be assumed to be independent and uncorrelated for each satellite. A challenge in this scenario is modeling the maximum interference between transmissions from different satellites.

4.1.1 Satellite scenario

The initial step in evaluating a satellite system involves determining the service requirements, which, in turn, establishes a minimum SINR at the perimeter of the service beam. Achieving this required SINR primarily depends on mitigating the link loss, with the key factor being the distance between the satellite and the user at the edge of the beam, denoted as ρ_{MAX} in Fig. 4.1. This distance is essential for closing the link budget.

Futhermore, Fig. 4.1 shows a typical satellite user view, where the maximum slant range is defined by R_{MAX} at an elevation angle of $0°$. It also shows the usable area as a spherical cap A in green, defined by the minimum elevation angle θ_{MASK}. At the elevation angle θ_{MASK}, the satellite is at the maximum usable distance ρ_{MAX}. The figure also displays different satellites: one of interest, three that could interfere with the satellite of interest, and one out of sight

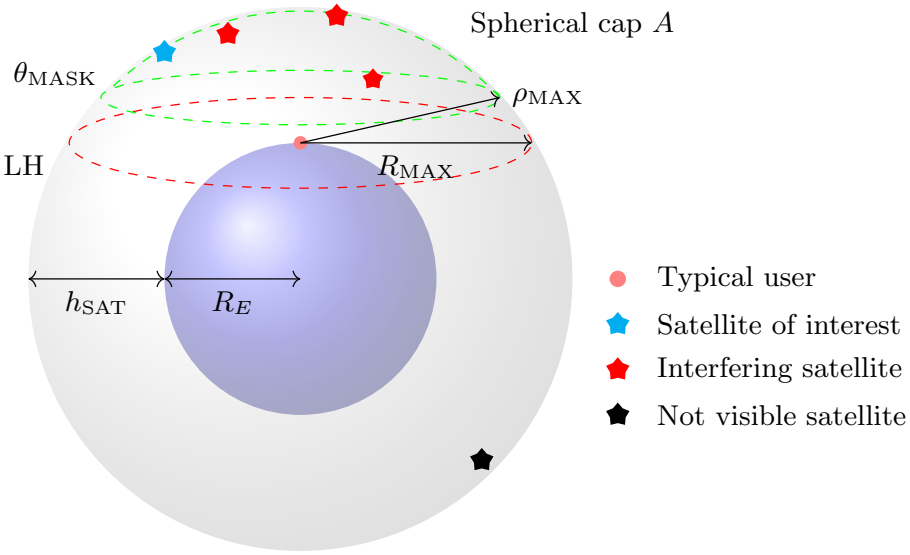

Fig. 4.1: A typical satellite user view, where the maximum slant range is defined by R_{MAX} at an elevation angle of 0°. It also shows the usable area as a spherical cap A in green, defined by the minimum elevation angle θ_{MASK}. At the elevation angle θ_{MASK}, the satellite is at the maximum usable distance ρ_{MAX}. The figure also displays different satellites: one of interest, three that could interfere with the satellite of interest, and one out of sight of the user.

of the user. In Fig. 4.1, the elevation angle mask θ_{MASK} delimits the coverage area when the user limits its operation due to link budget constraints. The value of θ_{MASK} is crucial, as it significantly impacts the maximum signal propagation time between the satellite and the ground station, as well as the maximal losses incurred due to free space path loss (FSPL). This parameter represents the minimum elevation angle required to achieve a certain quality of service, as below this value, the slant range (distance between the user and satellite) is too large, and the channel losses are too high to guarantee the quality of service.

Then, Fig. 4.2 shows a perpendicular cross section of the plane illustrated in Fig. 4.1, aiding in understanding the trigonometric calculations leading to (4.1). This figure demonstrates the direct relationship between θ_{MASK} and ρ_{MAX} in relation to the altitude of the satellite h_{SAT} plus the radius of the Earth R_{E}.

$$\rho_{\text{MAX}} = (R_E + h_{\text{SAT}}) \frac{\sin\left(\frac{\pi}{2} - \Psi\right)}{\sin\left(\frac{\pi}{2} + \theta_{\text{MASK}}\right)}, \tag{4.1}$$

Here, it is defined (4.2) to simplify the mathematical notation of (4.1), where the value of Ψ is defined as:

$$\Psi = \theta_{\text{MASK}} + \arcsin\left(\frac{R_E \sin\left(\frac{\pi}{2} + \theta_{\text{MASK}}\right)}{R_e + h_{\text{SAT}}}\right), \tag{4.2}$$

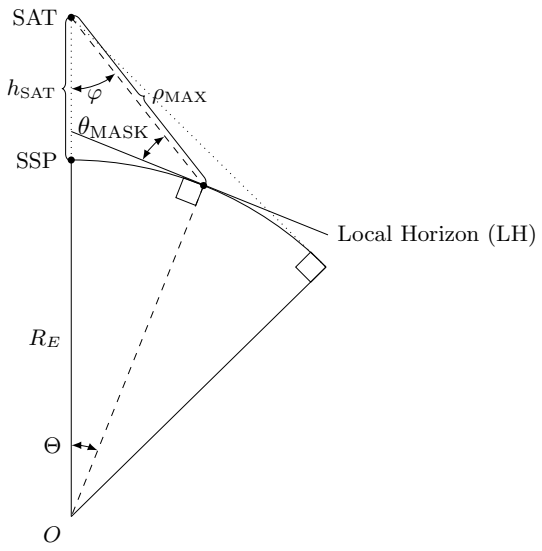

Fig. 4.2: Distances and angles within a satellite beam depends on the user LH, and the altitude of the satellite h_{SAT}.

Additionally, the LH is the tangential plane to the Earth's surface at the user's location, used to define the parameters of a satellite pass over this user.

Moreover, Fig. 4.3 presents a three-dimensional representation of a single satellite pass, expanding the concept of the LH from Fig. 4.2. This depiction emphasizes that the LH depends on the geographical coordinates of the user, defined by latitude ϕ, longitude λ, and altitude above mean sea level h. This implies that for a moving user, the LH will change. However, for this analysis, since the user's speed is much smaller than the satellite's speed $\mathbf{v}_{\mathrm{UE}}(t) \ll \mathbf{v}_{\mathrm{SAT}}(t)$, it is assumed the user is static.

Finally, Fig. 4.3 highlights various parameters that play a critical role in understanding satellite dynamics from the perspective of a ground user, which are integral to the channel model. Among these parameters, θ_{MAX} stands out as particularly significant. It represents the maximum elevation angle that the satellite will attain during a specific pass over the user. This parameter is vital because it influences several other factors, such as the duration of the satellite pass and the minimum distance between the satellite and the user, represented by ρ_{min}. The range of θ_{MAX} is defined as being between $[\theta_{\mathrm{MASK}}, \pi/2]$ if the user's latitude ϕ is smaller than the satellite inclination i, and $[\theta_{\mathrm{MASK}}, \Phi]$ if $\phi > i$, where $\Phi = \pi/2 - \theta_{\mathrm{MASK}} - \phi_{\mathrm{MAX}}$. Here, ϕ_{MAX} is the maximum user latitude where the satellite's maximum elevation angle reaches, at least, the elevation angle mask $\theta_{\mathrm{MAX}} \geq \theta_{\mathrm{MASK}}$. The value of ϕ_{MAX} can be

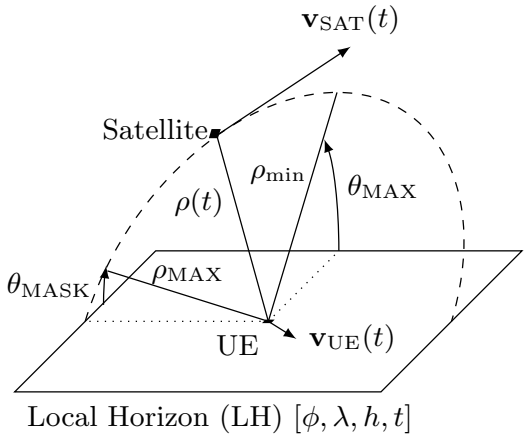

Fig. 4.3: Parameters involved in a single satellite pass.

obtained using the law of cosines:

$$\phi_{\mathrm{MAX}} = \arccos\left(\frac{2R_E^2 + h_{\mathrm{SAT}}^2 + 2R_E h_{\mathrm{SAT}} - \rho_{\mathrm{MAX}}^2}{2R_E\left(R_e + h_{\mathrm{SAT}}\right)}\right) \tag{4.3}$$

It should be noted that each satellite pass will have a unique value of θ_{MAX}, determined by orbital dynamics, the user location, and the time, while:

$$\max\left(\theta_{\mathrm{MAX}}\right) = \begin{cases} \pi/2 & \text{if } i \geq \phi \\ \Phi & \text{if } i < \phi \end{cases} \tag{4.4}$$

is the maximum value achievable for θ_{MAX}.

As a summary of the previous analysis, its provided a numerical example to give the reader a clear understanding of the concepts previously described. Assuming a satellite with $h_{\mathrm{SAT}} = 600$ km, an orbit inclination of $i = 60°$, and an elevation angle mask of $\theta_{\mathrm{MASK}} = 10°$, users within a latitude range of $\phi \in \pm i$ will experience a maximum elevation angle of $\pi/2$ at some point, while users up to latitudes of $\pm 75°$ will be able to close the link budget, as the satellite will reach at least an elevation angle equal to the elevation angle mask at some point. Users above these latitudes and up to $\pm 84°$ will have the satellite in LOS, but it will never exceed θ_{MASK}. Finally, for users located above $\pm 84°$, the satellite will never appear above the horizon. This example only represents the values for the line of sight between the user and satellite and does not take into account any antenna pattern.

From the previous example, there is a time dependency between the user location, the satellite movement, and θ_{MAX}, as both the satellite and Earth move. Stochastic models have

been developed in the literature to remove the time dependency, such as the work in [117], where the authors present a statistical model to estimate the elevation angle of a satellite, and the work in [118] presenting a statistical model for the maximum elevation angle of a satellite pass.

For wireless communications, the main parameters of the satellite are the slant range between the i-th satellite and the user, $\rho_i = \|\mathbf{r}_{\text{SATi}} - \mathbf{r}_{\text{UE}}\|$, and the relative speed between the satellite and the user, $\mathbf{v}_{\text{SATi,UE}} = (\mathbf{v}_{\text{SATi}} - \mathbf{v}_{\text{UE}})$. These two parameters determine the delay, path loss, and Doppler shift that the signal will experience at the receiver, as defined by the channel model. To obtain these parameters, there are stochastic models such as those in [119, 120, 121]. However, those models assume that the number of satellites in view follows a Poisson Point Process, while in this scenario, it is assumed that there are always 4 satellites in view at random positions on the spherical cap A. This assumption is grounded in projections for future PNT service constellations, which are designed to provide continuous coverage with an average of four satellites visible to users in these regions [122]. The anticipated orbital configurations and satellite densities of these constellations support this level of satellite visibility, making this assumption both feasible and representative for this analysis.

4.1.2 Wireless channel model

This is the wireless channel in a delay/Doppler spread representation [103], i.e.,

$$\gamma_i(\upsilon, \tau) = \sqrt{L_i}\; h_i \delta(\upsilon - \upsilon_i)\delta(\tau - \tau_i). \tag{4.5}$$

The channel representation in (4.5) depends on four parameters: the free space path loss $L_i = \left(\frac{c}{4\pi f_c \rho_i}\right)^2$, a random phase rotation h_i, a delay $\tau_i = \frac{\rho_i}{c}$, and a Doppler shift defined as $\upsilon_i \triangleq -\frac{f_c}{c}\frac{d}{dt}\rho_i$, where $\frac{d}{dt}\rho_i = \hat{\mathbf{u}}_{\text{SATi}}^T \mathbf{v}_{\text{SATi,UE}}$ is the relative speed between the UE and the i-th satellite, calculated as the projection of $\mathbf{v}_{\text{SATi,UE}}$ onto $\hat{\mathbf{u}}_{\text{SATi}}$. Then, $\hat{\mathbf{u}}_{\text{SATi}} = \frac{\mathbf{r}_{\text{SATi}} - \mathbf{r}_{\text{UE}}}{\|\mathbf{r}_{\text{SATi}} - \mathbf{r}_{\text{UE}}\|}$ is a unit vector that points from the user to the i-th satellite. Finally, h_i represents the initial random phase and is constant for the received signal. Since it is a constant value, it will not affect the correlation process during the acquisition step in the receiver; therefore, it is assumed an initial phase of 0.

Furthermore, it is assumed that the channel is wide-sense stationary (WSS) for the duration of the slot (0.5ms using 30kHz of subcarrier spacing); thus, the values of L_i, τ_i, and υ_i can be considered constant for the duration of the slot. The mean variation of the delay is on the order of 3ns for 0.5ms of satellite movement, and after one slot, the assumed

error is less than 0.001%. This is a realistic assumption that does not compromise the results, as similar NTN models use it [123].

The channel FSPL is modeled by L_i assuming unit gain on both the TX and RX antennas, i.e., isotropic. L_i depends on the carrier frequency f_c and ρ_i. A more realistic NTN channel would include other losses, such as tropospheric effects (e.g., gas absorption, rain/cloud attenuation), antenna beam/polarization misalignment, etc. These effects are assumed negligible, as these attenuations are much lower compared to FSPL for transmissions in the L/S frequency bands.

The signal delay τ_i is also considered constant, as the change during a slot is negligible. A more accurate model would include additional ionospheric and tropospheric delays due to signal refraction. These effects have been extensively studied for GNSS receivers and are modeled by the Klobuchar model [124] or the NeQuick model [125, 126]. However, the inclusion of these models could obscure the theoretical analysis of this work, as the model for the interference does not depend on specific values for the effects of satellite dynamics but rather on the differential values of delay and Doppler between satellites, as it will be show later.

The model of v shows that the measured Doppler is proportional to the relative speed of the satellite-user link in an ideal scenario, where its value is only affected by the dynamics of the satellite and the user. The channel model in (4.5) serves as a baseline for the generation of a dataset published in [127]. This dataset generation is described in Appendix B.

4.2 Transmitted and received signal model

This section presents the transmitted signal model based on the models in Chapter 3 and the theoretical framework for analysing interference between satellites transmitting the PRS.

The focus is on analysing the impact of the NTN channel on transmissions from S satellites, assuming LOS conditions and no multipath effects.

4.2.1 Downlink signal model

The 5G downlink signal model begins with the generation of the PRS sequence for each i-th satellite, as seen in the previous chapter. The CP-OFDM modulation is applied as explained also in the previous chapter. The transmitted signal from satellite i is thus expressed in its complex baseband form, as described by

$$x_i(t) = \sqrt{P_{\mathrm{TX}}} \sum_{m=0}^{M-1} \sum_{k=0}^{N_{\mathrm{SCS}}-1} A_i[m,k] e^{j2\pi k \Delta f t} \mathrm{rect}\left(\frac{t - mT_s}{T_s}\right). \tag{4.6}$$

The transmitted signal $x_i(t)$ has an average power level of P_{TX}. This power level is fixed at the satellite's HPA to guarantee minimum performance for beam-edge users. This approach assumes, similar to GNSS, a uniform EIRP across the satellite beam.

4.2.2 Received signal model

The channel model outlined in (4.5) describes a channel between the i-th satellite gNB and the UE. In a positioning system, the user typically receives all downlink signals within the same bandwidth part for positioning (BWPP) spectrum. Thus, the received signal model is an aggregation of different NTN signals, each affected by a distinct channel γ_i. The received signal is modeled by

$$y(t) = \sqrt{L_i} \sum_{i=0}^{\mathrm{S}-1} e^{j2\pi \upsilon_i t + \varrho} x_i(t - \rho_i/c) + w(t), \tag{4.7}$$

as the aggregation of the signal received by the S satellites in LOS. The model (4.7) is essential for subsequent analyses, including SINR evaluations and performance assessments of the delay estimator.

4.2.3 Matched filter

In the receiver architecture, the matched filter operation is based on the CAF defined previously in (3.8). The received signal is compared against the different local copies of the PRS, one per satellite. Therefore, the receiver will perform at least four different CAF computations.

Substituting the received signal $y(t)$ into the CAF, and following a similar analysis as done in [128], the matched filter output for the i-th PRS is given by

$$\chi_{yx}^{(i)}(\upsilon,\tau) = \sqrt{L_i} e^{j2\pi(\upsilon-\upsilon_i)\tau_i} \chi_{xx}^{(i)}(\upsilon-\upsilon_i, \tau-\tau_i) + \sum_{s\neq i s=0}^{\mathrm{S}-1} \sqrt{L_s} e^{j2\pi(\upsilon-\upsilon_s)\tau_s} \chi_{x_s x}^{(i)}(\upsilon-\upsilon_s, \tau-\tau_s) + \chi_{wx}^{(i)}(\upsilon,\tau). \tag{4.8}$$

4.2.4 Post-Matched filter signal to interference plus noise ratio analysis

This subsection concludes the modeling discussion by presenting SINR as a critical KPI for analyzing receiver performance. Assessing SINR is paramount for the effective detection of the peak in the receiver's detector.

The maximum value of the AF is at the origin $\tau = 0, \upsilon = 0$. By applying a variable change in (4.8) as $\tau' = \tau - \tau_i$ and $\upsilon' = \upsilon - \upsilon_i$, is shifted the origin to the peak, then evaluate the CAF in relation to the difference in delay and Doppler of interference signals. For this, it has been applied the following change of variables in (4.8): $\Delta\tau_s = \tau_i - \tau_s$ and $\Delta\upsilon_s = \upsilon_i - \upsilon_s$, yielding

$$\chi_{yx}^{(i)}(\tau', \upsilon') = \sqrt{L_i} e^{j2\pi\upsilon'\tau_i} \chi_{xx}^{(i)}\left(\upsilon', \tau'\right) + \sum_{\substack{s\neq i \\ s=0}}^{S-1} \sqrt{L_s} e^{j2\pi(\upsilon'-\Delta\upsilon_s)\tau_s} \chi_{x_s x}^{(i)}(\upsilon'-\Delta\upsilon_s, \tau'-\Delta\tau_s) + \chi_{wx}^{(i)}(\upsilon', \tau'). \tag{4.9}$$

Therefore, it can find the contribution to the SNR of the signal of interest i from the other s satellites. As mentioned above, the peak of the displaced CAF corresponds to $\upsilon' = 0$ and $\tau' = 0$. Therefore, it is defined the SINR by setting $\upsilon' = 0$ and $\tau' = 0$ in the CAF:

$$\begin{aligned} \mathrm{SINR}_i &= \frac{L_i P_{\mathrm{TX}}}{\sum_{s\neq i}^{S-1} P_{\mathrm{TX}} L_s |\chi_{x_s x}\left(\Delta\upsilon_s, \Delta\tau_s\right)|^2 + |\chi_{wx}\left(\upsilon_i, \tau_i\right)|^2} \\ &= \frac{P_{\mathrm{TX}} \rho_i^{-2}}{\sum_{s\neq i}^{S-1} P_{\mathrm{TX}} \rho_s^{-2} |\chi_{x_s x}\left(\Delta\upsilon_s, \Delta\tau_s\right)|^2 + \sigma^2}, \end{aligned} \tag{4.10}$$

where it is assumed the same transmission power across all satellites, denoted as P_{TX}, and the CAF of the receiver noise as $|\chi_{wx}\left(\upsilon_i, \tau_i\right)|^2 = \sigma^2$. This simplification incorporates the concept that the noise power is attenuated by the transmitted power normalized by the FSPL at the i-th satellite, represented as $P_{\mathrm{TX}} L_i$.

Consequently, the interference contribution of the remaining satellites to the i-th satellite SINR depends on the distance ρ_s and the CAF, and is expressed as

$$I_i = P_{\mathrm{TX}} \sum_{s\neq i}^{S-1} \rho_s^{-2} |\chi_{x_s x}\left(\Delta\tau_s, \Delta\upsilon_s\right)|^2. \tag{4.11}$$

This assumption is valid under the approximation that all satellites transmit at the same frequency carrier f_c, which is the characteristic scenario when using a common BWP for transmitting the PRS. Moreover, interference is further influenced by the values of the CAF for the differential delay, denoted as $\Delta\tau_s$, and the differential Doppler shift, represented as

Δv_s, between the satellite of interest i and the interfering satellite s.

Satellite positions are required to compute their distance to the user, ρ_s. However, a closed form for ρ_s is complex and has several dependencies, such as the time of observation, the position of the user on Earth, the satellite constellation design, the orbit model, etc. In Fig. 4.1 is presented that all satellites are located on a spherical cap, called A. The satellites' azimuth and elevation angles can be considered as uniform random variables, where the azimuth angle is between $[0, 2\pi]$ and the elevation is between $[\theta_{\text{MASK}}, \pi/2]$. However, the distance to the user is not random, as it depends on the azimuth, elevation, and the spherical cap where the satellites lie.

Therefore, to evaluate the interference, a statistical approach is taken. The interest is in the extreme (maximum) values of the interference, as they have a very high impact on receiver performance. In extreme value theory, there are two fundamental approaches, both widely used: the block maxima (BM) method and the peaks-over-threshold (POT) method.

The BM approach consists of dividing the observation period into non-overlapping periods of equal size and focuses on the maximum observation in each period. This approach fits this analysis, as each block can be seen as an OFDM slot, and is evaluated the maximum value of the interference per slot.

Using the Fisher–Tippett–Gnedenko theorem detailed in Appendix A, which establishes that the distribution of the maximum value of the BM converges to the GEV defined in (4.12).

$$F_{\text{Interference}}(x) = \exp\left(-\left[1 + k\left(\frac{x-\mu}{\sigma}\right)\right]^{-1/k}\right). \tag{4.12}$$

This GEV distribution is defined by three parameters: k (shape), σ (scale), and μ (location). However, obtaining a closed-form expression for these parameters based on the PRS configuration is not feasible analytically; for this reason, is followed an empirical approach to estimate these parameters. In the next section there is an extraction of the different expressions to model the interference based on the PRS configuration.

4.3 Empirical interference model extraction

This section describes the Monte Carlo simulator developed, the methodology used to extract the interference model empirically, and the parameter models based on the PRS waveform configuration.

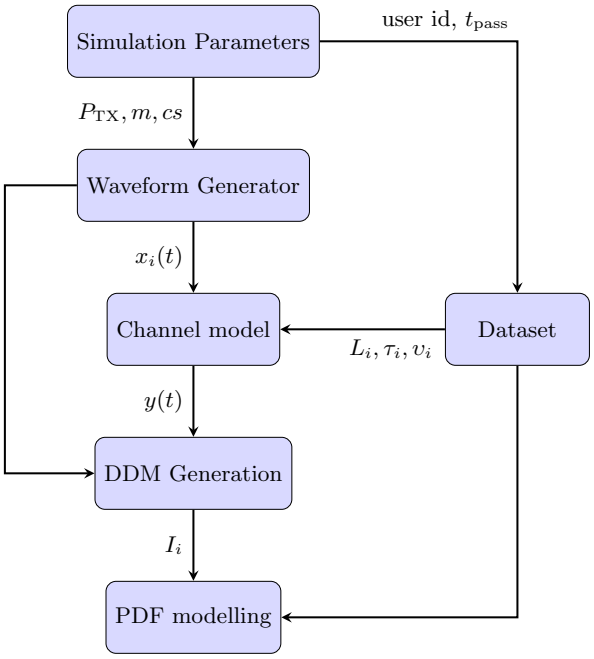

Fig. 4.4: 5G PRS LEO simulator architecture.

4.3.1 Monte Carlo simulator architecture

Fig. 4.4 shows the simulator developed to extract the model for the PDF of the interference as seen in equation (4.11). This simulator follows a Monte Carlo technique, evaluating the system for different user locations and signal configurations from the public dataset [127] and from a different constellation proposed in [122] for the future LEO-PNT mission by ESA. This constellation proposed consists of 11 orbital planes, with 19 satellites per plane, evenly distributed using polar orbits at an altitude of 1200 km. The interference model will be compared with each constellations and find a common model that generalizes it, to be independent of the constellation design.

The assumption made for the simulator is that all satellites are synchronized and transmit the PRS at the same time using the RG arrangement shown previously in Fig. 3.3.

The simulator starts with the definition of the simulation parameters, such as the signal configuration and the dataset [127] for the satellite passes. Then, it generates the requested waveforms. The next step is to apply the corresponding channel to each waveform i, where the delay τ_i, losses L_i, and Doppler υ_i are tightly coupled due to satellite movement. The simulator then performs the signal acquisition by computing the delay-Doppler map (DDM) of the received signal, composed of the signal of interest and the other interference signals

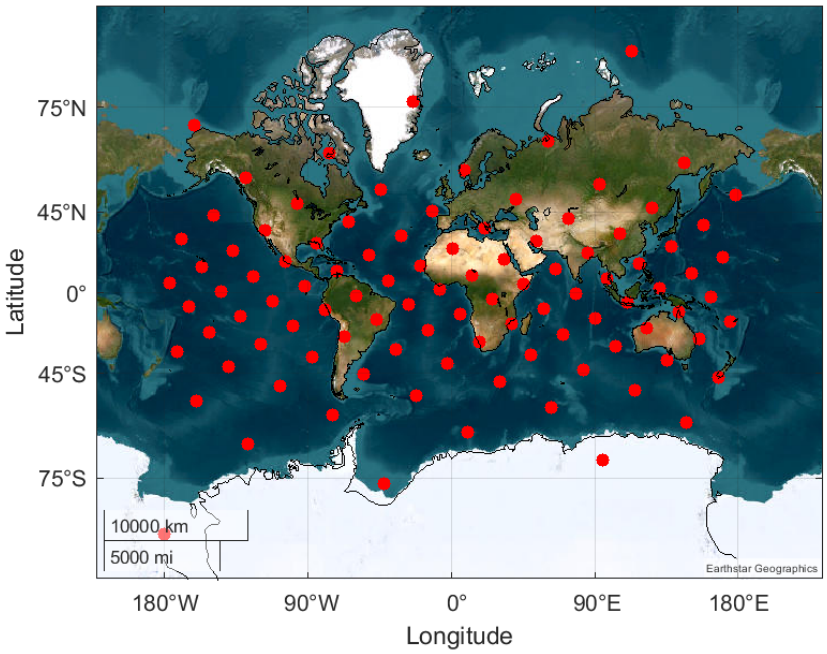

Fig. 4.5: User's distribution of the dataset.

plus noise. Finally, from the DDM, the simulator generates the interference power samples used to analyze its probabilistic behavior.

Both datasets used contain 100 users uniformly spread across Earth's surface (using a Fibonacci lattice). For each user location, 10 minutes of satellite passes are stored with a 1-second resolution. Fig. 4.5 shows the locations of the users on Earth from the dataset used to compute the satellite passes.

The Monte Carlo simulator performs 10,000 iterations per user location and transmitted waveform parameters (number of symbols, Comb Size, and transmitted power). To compute the interference, the procedure illustrated in Fig. 4.4 is followed. For each user in the dataset, it is generated the transmitted signal and apply a channel model at a randomly selected time, thereby assigning specific values of slant range and velocity to the satellites. After applying the channel model, the acquisition process begins. This process is analogous to the acquisition step in GNSS receivers, wherein a bank of correlators processes the signal using local replicas. A threshold is then applied to ascertain the presence of the signal of interest. If the signal is not detected, the process is repeated with different local replicas. If the signal is detected, the simulation environment is used to evaluate the power of the signal of interest and the power of other signals, which are treated as interference. The obtained interference power

Table 4.1: Scenario details

Description	Symbol	Value
Number of satellite in LOS	S	4
Maximum signal bandwidth	BW_{MAX}	8.64 MHz
Satellite's constellation 1	Starlink	Inclination of 53 deg at 554 km
Satellite's constellation 2	LEO-PNT	Polar 11x19 at 1200 km
Carrier frequency	f_c	n256 (2.2 GHz)
Number of MC iterations	N_{index}	10000
Doppler Max value	$\pm v_{\text{MAX}}$	40 kHz
Doppler resolution	v_{step}	500 Hz

Table 4.2: PRS generation details.

Description	Symbol	Value
Number of Symbols	m	1 to 12
Number of Subcarriers	N_{SC}	288
Subcarrier Spacing	Δf	30 kHz
Comb Size	cs	4, 6 and 12
Transmitted power	P_{TX}	1 to 30 dBW

values are then used to develop the interference model.

Table 4.1 enumerates the parameters relevant to the scenario described in Section 4.1. In this scenario, the number of concurrent satellites in LOS is set to four, which represents the minimum required for 3D position estimation. The bandwidth is set to the minimum permissible for the transmission of the PRS. Similarly, the carrier frequency is chosen as the highest allowed within the n256 band.

Table 4.2 shows the various parameter values used to generate the PRS in the simulation. It has been done a comparison using different numbers of OFDM symbols, various Comb Size values, and different transmission powers.

4.3.2 GEV parameters extraction for the interference model

As seen in Section 4.2, the statistical interference model in (4.11) used in the SINR analysis can be modeled by a GEV. However, an analytical evaluation of the GEV parameters μ, σ, k is not feasible in this satellite scenario. Therefore, it is presented the methodology for using the Monte Carlo approach to extract the distribution parameters of the interference created by the PRS.

Table 4.3 shows the KS fitness test and p-value for the different commonly known

Table 4.3: KS test and p-test result for the different distribution evaluated.

Distribution	**KS**	**p-test**
Normal	0.0382	0
LogNormal	0.0256	0
Gamma	0.0298	0
Rayleigh	0.5295	0
Rician	0.0382	0
GEV	0.0142	0.368

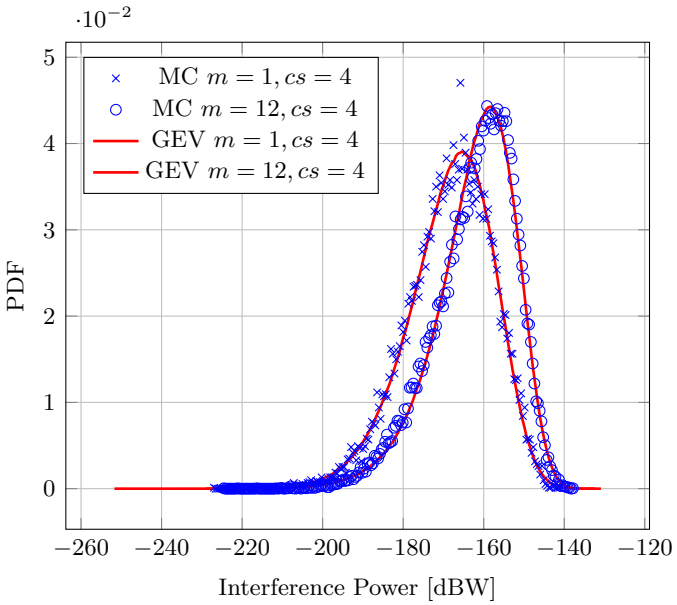

Fig. 4.6: An example of a PDF of the interference power used to compare the results from the Monte Carlo simulation and the GEV distribution.

distributions used to compare the fitness of the data extracted. As predicted by the Extreme Value Theorem in Appendix A, the distribution that best fits the measurements corresponds to the GEV distribution, which has the lowest KS statistic of 0.0142 and the highest p-value of 0.3688.

Furthermore, Fig. 4.6 shows, in discrete blue, the empirical PDF for two different waveform configurations (using 1 and 12 OFDM symbols) from the simulator and, in continuous red, the fitted PDF using a GEV model.

Once it is evaluated the model that best fits the maximum values of interference, it is identified the relationship between the waveform parameters—number of symbols m, Comb Size cs, and transmission power P_{TX}—and the distribution parameters—shape k, scale σ, and

Table 4.4: Comparison of GEV parameters between the Generic, Polar, and starlink scenarios.

Scenario	a_1	a_2	a_3	b_1	b_2	b_3	b_4	c_1	c_2	c_3
LEO-PNT	8.5535	0.0237	-0.0042	199.994	-1.909	8.571	-0.0143	-0.1428	-0.1061	0.0042
Starlink	8.8366	-0.1809	0.0087	195.402	-1.950	13.826	-0.0086	-0.0674	-0.1572	0.0004
Generic	8.6951	-0.0786	0.0023	197.698	-1.929	11.198	-0.0114	-0.1051	-0.1316	0.0023
Residual (LEO-PNT)	0.1416	0.1023	0.0065	2.296	0.020	2.627	0.0029	0.0377	0.0255	0.0019
Residual (Starlink)	0.1415	0.1023	0.0064	2.295	0.021	2.628	0.0028	0.0377	0.0256	0.0019

location μ. A compromise was found between the complexity of the model and the fitness of the data.

- Scale:

$$\sigma(m) = a_1 + a_2 m + a_3 m^2 \tag{4.13}$$

- Location:

$$\mu(m, P_{\text{TX}}) = b_1 + b_2 P_{\text{TX}} + b_3 m^{-1/2} + b_4 m P_{\text{TX}} \tag{4.14}$$

- Shape:

$$k(m) = c_1 + c_2 m^{-1/2} + c_3 m \tag{4.15}$$

A curve fitting process is followed to obtain the parameters of (4.13), (4.14) and (4.15) using the Levenberg-Marquardt algorithm for least squares minimization. The following table 4.4 shows the numerical values of the parameters for both constellations and a third scenario called "Generic", where fit the parameters from both scenarios to make the model agnostic of the scenario. Besides, it has added the fitting error as R^2 for each parameter. Furthermore, it also show the residuals between the "Generic" constellation values and the other two to show that this generic model can be used for any constellation design, having into account the error obtained. This is a trade off between the complexity of the model and accuracy of it.

The results from Table 4.4 show that the parameter $k < 0$, indicating that the GEV is a bounded distribution (Weibull), suggesting a **upper limit to interference power**. This upper limit arises from the output of the DDM when comparing two different signals. Furthermore, the low values of k suggest a low risk of extreme interference power.

Figures 4.7, 4.8, and 4.9 show the models used for the parameters k, σ, and μ using data from the LEO-PNT, Starlink, or both. They also include the 95% confidence interval for the model of both constellations.

- LEO-PNT Model: The R^2 value is higher for all parameters in the LEO-PNT model

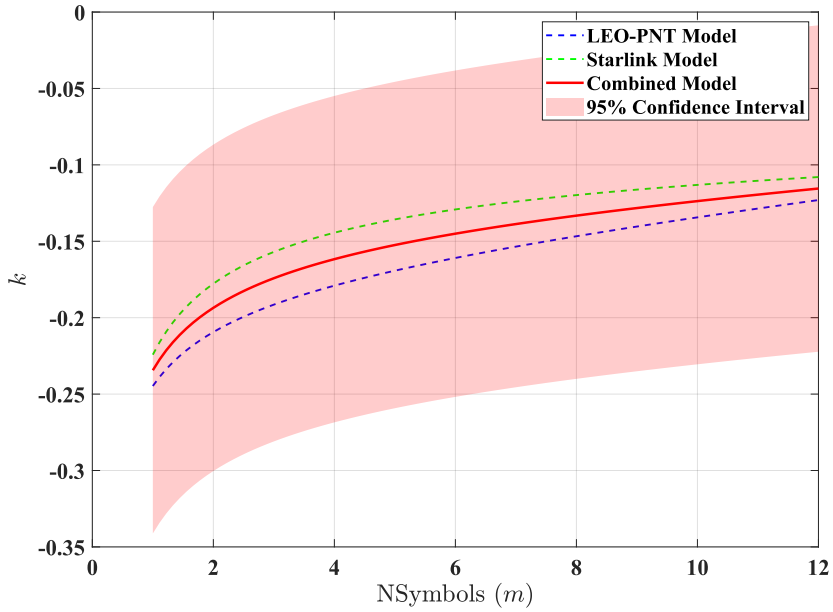

Fig. 4.7: k value for both dataset separately, k for the combined dataset and the confidence interval

Table 4.5: R^2 metric for the fitting of the curves.

Constellation	R_k^2	R_σ^2	R_μ^2
LEO-PNT	0.91	0.95	0.93
Starlink	0.88	0.92	0.89
Combined	0.90	0.94	0.91

when applied to its own dataset.

- Starlink Model: The Starlink model has a lower R^2 than the combined model, indicating that the combined model is able to generalize better than the Starlink-specific model in this case.

- Combined Model: The combined model, which fits both the LEO-PNT and Starlink data, has a lower error than the Starlink-specific model, particularly for the parameter μ. This suggests that the combined model provides a good balance in fitting both datasets, sometimes even outperforming one of the specific models (Starlink, in this case).

The combined model benefits from exposure to both datasets, allowing it to find patterns that generalize well across different scenarios, while the Starlink-specific model may overfit

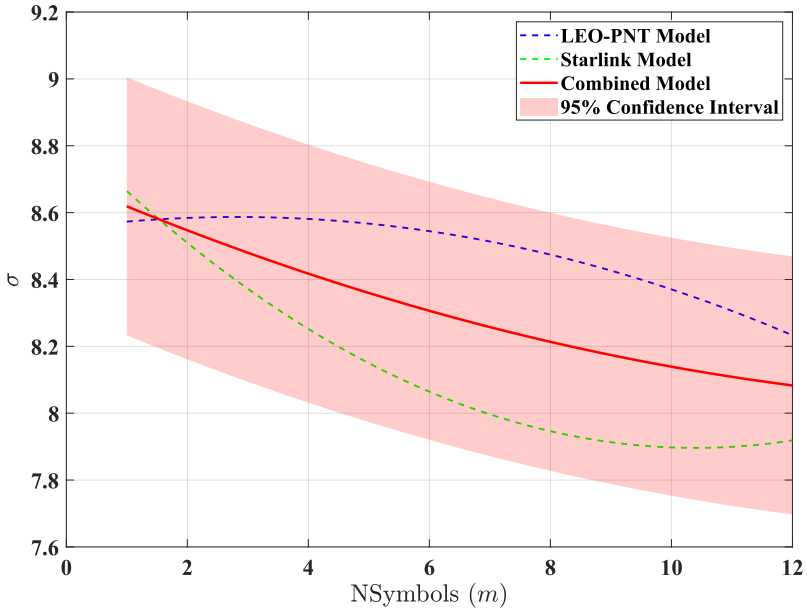

Fig. 4.8: σ value for both dataset separately, σ for the combined dataset and the confidence interval

to the nuances of the Starlink data, leading to a lower R^2. This explains why the combined model can outperform a model fitted on just one dataset. The combined model generalizes well, making it a robust choice across both datasets.

4.3.3 Result discussion

This model extraction can be used in future designs to evaluate the interference power that a PRS pilot will generate in a typical scenario with reception from four satellites. It can be used to calculate the exceedance probability that the interference power exceeds a certain threshold x, as shown in (4.16).

$$P(M > x) = 1 - F_{\text{GEV}}(x). \tag{4.16}$$

By formulating the interference power, it is possible to:

- Quantify Extreme Events: Provide mathematical expressions for the probability and magnitude of extreme interference events.
- Inform Decision-Making: Aid in the design of satellite communication systems that can withstand rare but severe interference events.

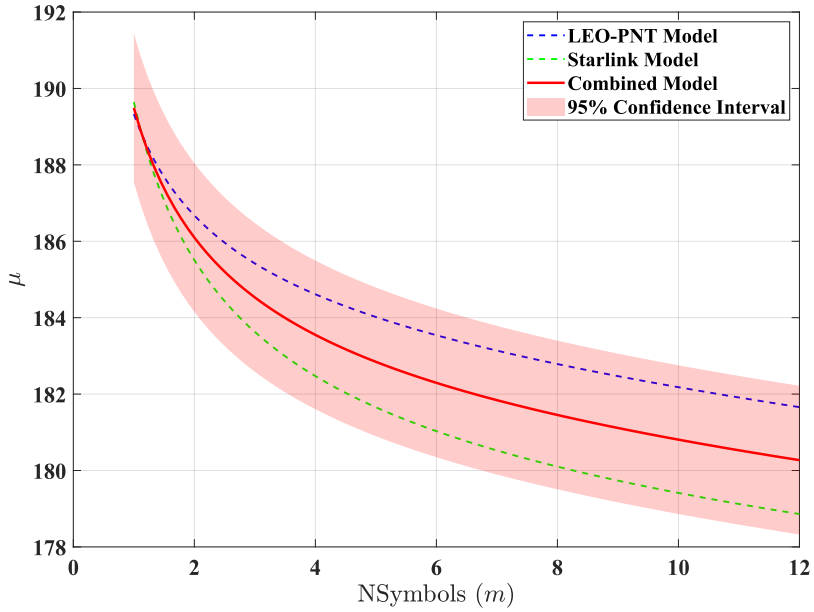

Fig. 4.9: μ value for both dataset separately, μ for the combined dataset and the confidence interval using $P_{\mathrm{TX}} = 10\,\mathrm{dBW}$

- Enhance Reliability: Improve overall performance and reliability by proactively managing the risks associated with extreme interference.

4.4 Summary

This chapter addresses interference modeling specifically for the PRS within 5G NTN scenarios. It introduces an empirical statistical approach, applying the extreme value theory (EVT) framework, particularly using the GEV distribution, to characterize interference impacts arising from multiple concurrent satellite transmissions. Extensive Monte Carlo simulations of realistic satellite passes were performed, capturing the statistical behavior of interference power in NTN scenarios. The resulting interference model effectively quantifies rare but critical interference events, crucial for designing robust link budgets and reliable detection algorithms for NTN-based positioning systems.

From the simulation results, it was concluded that interference in NTN scenarios can be accurately modeled using the GEV distribution, with interference power strongly influenced by the waveform configuration (such as number of symbols and transmitted power). This analysis enables precise optimization of PRS configuration for improved detection reliability

and robust system performance, mitigating interference-related risks that significantly affect positioning accuracy and service continuity in satellite environments.

Recognizing the inherent challenges of integrating dedicated PRS signals into existing 5G NTN deployments, particularly due to high interference and complexity in synchronization, Chapter 5 proposes a JCAP solution. It maintains OFDM as the primary data waveform to ensure seamless backward compatibility with legacy 5G terrestrial and NTN systems, leveraging the extensive existing infrastructure and standardization. To enhance positioning capabilities, an overlay DSSS signal is introduced, combining both signals into a single, unified waveform. This hybrid approach provides robust PNT services, as the DSSS component exhibits superior resilience to Doppler and interference, while preserving the proven spectral efficiency and reliability of OFDM for data communication.

Chapter 5

Joint communication and positioning from LEO multi-beam satellite

The previous chapter shows a model of the interference when using the PRS in a NTN scenario. This chapter shows two novel architectures for a JCAP system that no need to use the PRS pilots. This chapter start showing the system models. Then, the KPIs used to evaluate the performance of this JCAP system and the pareto front for the SIR between the navigation and communications waveforms. It continue with simulations to evaluate the KPIs for the different architectures in two different scenarios and finalize with a discussion of the results. The work presented in this chapter has been published in the OJ-COMS as [23].

5.1 System model

This section presents two architectures, referred to as "Shared beam" ("A" for the mathematical notation) for the model who share the beam for both services, this model is a superposition of both waveforms in baseband. The second model called "Independent" ("B" for the mathematical notation) for the model where the communication and navigation services are at independent beams, but the beams share most of the common illuminated area. In this model, both signals are aggregated at RF, known as over-the-air (OTA).

Each model architecture is presented. Then, a detailed description of the channel model is provided, as well as the signals models for both transmission and reception, and the SINR models.

A general assumption is that the beams are intended to be in a fixed AoD, known in the literature as *Earth moving beams* [129].

5.1.1 Beamforming network

Start by assuming that each model employs a DBF, where the signals for data and navigation can be aggregated in two distinct ways, depending on the model. This DBF control an uniform planar array (UPA) that is oriented always to the subsatellite point (SSP) on the ground. This UPA has $N_t = N_x^{\text{UPA}} \times N_y^{\text{UPA}}$ isotropic radiating elements, where, N_x^{UPA} and N_y^{UPA} are the number of elements on the x and y axis of the UPA. For the sake of simplicity, it is assumed a square UPA $N_x^{\text{UPA}} = N_y^{\text{UPA}}$. The elements are separated by $\lambda/2$, with λ the wavelength of the transmitted signal.

The UPA response is characterized by the steering vectors $\mathbf{a}(\theta, \phi)$, where the pair $[\theta, \phi]$ represents the AoD of the signal, determined by the azimuth $\theta \in [0, 2\pi)$ and the elevation angle $\phi \in [0, \pi/2]$ from the UPA plane [73]. The steering vector is defined by $\mathbf{a}(\theta, \phi) = \mathbf{a}^x(\theta, \phi) \otimes \mathbf{a}^y(\theta, \phi)$ as the Kronecker product between the array response in the x axis and the array response in the y axis. Each axis n-th element response is defined as:

$$a_n^x(\theta, \phi) = \frac{1}{\sqrt{N_x^{\text{UPA}}}} \exp\Big\{ j\pi n u_x \Big\} \tag{5.1}$$

$$a_n^y(\theta, \phi) = \frac{1}{\sqrt{N_y^{\text{UPA}}}} \exp\Big\{ j\pi n u_y \Big\} \tag{5.2}$$

where $u_x = \sin(\theta)\cos(\phi)$, $u_y = \sin(\theta)\sin(\phi)$ and $n \in \{0, \ldots, \sqrt{N_t} - 1\}$ is the number of elements per row or column in the UPA.

Shared beam model

This model also serves as a reference, as the CMMB uses the same approach to combine both signals before their transmission. It has been called *shared beam model*, and it is described in Fig. 5.1 and Fig. 5.2. The rationale for this model lies in its compatibility with existing designs, as no modifications are required in the DBF. It can work even as a single beam system.

In this first model, the aggregation of communication and navigation signals is done before the DBF. Consequently, the coverage of the data and navigation service will share the same beam because the aggregated signal uses the same transmission chain (see Fig. 5.2).

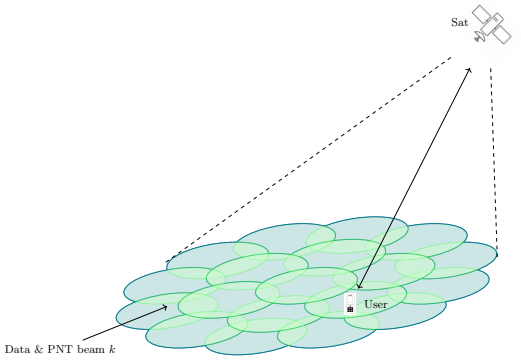

Fig. 5.1: K beams sharing data and navigation service. They all have the same color as all of them transmit the same waveform composed by the DSSS and OFDM.

Additionally, both services experience identical hardware impairments at the transmitter side. This solution facilitates the possibility of having distinct DSSS sequences in the navigation waveform, with one sequence allocated per beam. Moreover, it is cost-effective, as the DBF do not require any dedicated input port for the navigation signal.

The input for the beam k in the DBF can be defined as

$$s_k[n] = [\sqrt{\rho} \cdot z^{(k)}[n] + \sqrt{1-\rho} \cdot \tilde{z}[n]] \in \mathbb{C}, \tag{5.3}$$

where $\rho \in [0, 1]$ is the relative power level between the data $z^{(k)}[n]$ and the navigation $\tilde{z}[n]$ signal. All K beams inputs are collected side-by-side into an array $\mathbf{s}_{\mathrm{A}}[n] = [s_1[n], s_2[n], \ldots, s_K[n]]^T \in \mathbb{C}^{K\times 1}$.

Each of the N_t antennas transmits a linear combination of the K input signals, which is defined in matrix form as

$$\mathbf{x}[n] = \mathbf{W}^{(A)}\mathbf{s}_A[n] \in \mathbb{C}^{N_t\times 1}, \tag{5.4}$$

where $\mathbf{W}^{(A)} \in \mathbb{C}^{N_t\times K}$ is the steering matrix of the beamforming network (BFN) used to preserve the phase alignment at the reference point of the beams. It has been choose $\mathbf{W}^{(A)} = \mathbf{A}^*$ as the conjugate of the UPA response for K beams in predefined directions $[\theta_k, \phi_k]$, with $k \in \{1, \ldots, K\}$ defined as $\mathbf{A} = [\mathbf{a}_1, \ldots, \mathbf{a}_K] \in \mathbb{C}^{N_t\times K}$. Here, the notation of the array response is simplified to $\mathbf{a}_k(\theta_k, \phi_k) \triangleq \mathbf{a}_k \in \mathbb{C}^{N_t\times 1}$ by removing the angle dependencies, as each beam k can be distinctly identified solely by the beam number.

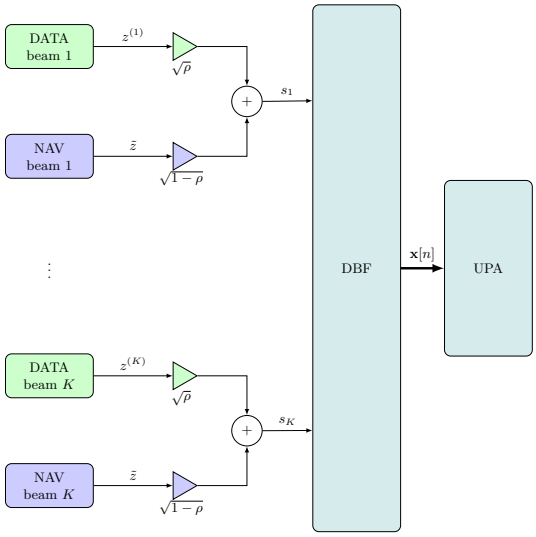

Fig. 5.2: System diagram for K beams. Each beam share a communication (green color) and a navigation (blue color) service as each beam transmission chain is composed by the same elements. The color after the waveforms aggregation represent the combination of green and blue color.

Independent beam model

This model follows a similar scheme designed in [32]. This second model is called *independent beams model*. In contrast to the shared beam model, it uses an additional input at the DBF for the navigation service while maintaining the same N_t elements at the UPA. Within this model, the beam designated for the navigation service is considerably wider than the communication beams, with the intent of illuminating as much area as possible. This design choice also indicates that the power received on the ground will be less than that of a spot beam. However, the processing gain of DSSS is very high for sequences like the ones used in GNSS [7]. By leveraging this characteristic the receiver can effectively use the navigation signal even with very low values of SINR.

Fig. 5.3 and Fig. 5.4 illustrates the independent beam model. In this scenario, the signals are transmitted across distinct beams (refer to Fig. 5.3), and the aggregation is considered done OTA, as both waveforms still share the same resources (time, frequency, and space).

The independent beam model generates $K + 1$ beams, K for the communication service and 1 extra for the navigation service. In this work, it is assumed that the navigation beam and the central beam for communication (the beam aimed at the SSP) has the same AoD $[\theta_1, \phi_1] = [\theta_{\text{NAV}}, \phi_{\text{NAV}}]$. The rationale behind this assumption is to maximize the coverage area for the navigation beam, and pointing towards the SSP will provide the largest field of view (FOV) from the satellite's perspective. However, each of these services have a different

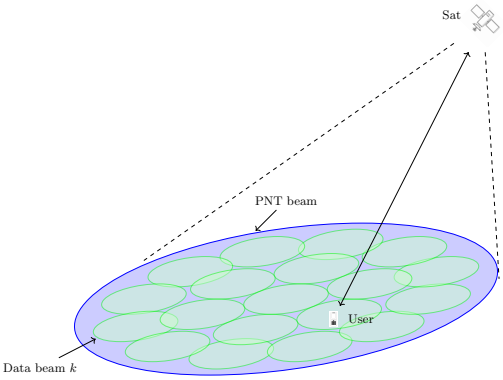

Fig. 5.3: K different beams for data and a single beam for navigation service.

beamwidth.

By using different spatial distributions in the UPA, the shape and width of the beam can be customized, even when both beams point in the same direction. Consequently, a narrow beam can be produced by utilizing the full aperture with a uniform amplitude distribution, whereas a wider beam can be generated by modifying the amplitude distribution across the array. There are two methods to accomplish this:

- **Tapering** [130, 131]: Apply an amplitude taper (e.g., a Hamming or Kaiser window) that progressively reduces the amplitude towards the edges of the array. This reduces the effective aperture in a soft manner, broadening the main lobe.

- **Subaperture Use** [132, 133]: Another approach is to effectively use only a central subset of elements to reduce the effective aperture size. A smaller effective aperture leads to a wider beam.

For the design of the steering matrix $\mathbf{W}^{(B)} \in \mathbb{C}^{N_t \times K+1}$ it is used the conjugate of the array response, similar to the shared beams model $\mathbf{W}^{(B)} = \mathbf{A}^*$. Then, for this model it is chosen the *subaperture use* method for the navigation beam, as it generally provides better overall HPA efficiency, allowing subarray's amplifiers to run closer to saturation [134, 135]. Therefore, the steering matrix $\mathbf{W}^{(B)}$ can be defined as $\mathbf{W} = [\mathbf{w}_1, \ldots, \mathbf{w}_K, \mathbf{w}_{\text{NAV}}]$, where each $\mathbf{w}_k \in \mathbb{C}^{N_t \times 1}$ are the weights for each beam. The navigation beam is now defined as $\mathbf{w}_{\text{NAV}} = [0, \ldots, w_u, w_{u+1}, \ldots, w_{u+j}, \ldots, 0]^T$, where most of the elements are be 0, except for the subset $\mathcal{U}$ of $j < N_t$ radiating elements used for the wide beam.

Then, as the navigation beam intentionally interferes with the communication beam, different power levels should be applied to each beam to control this intentional interference

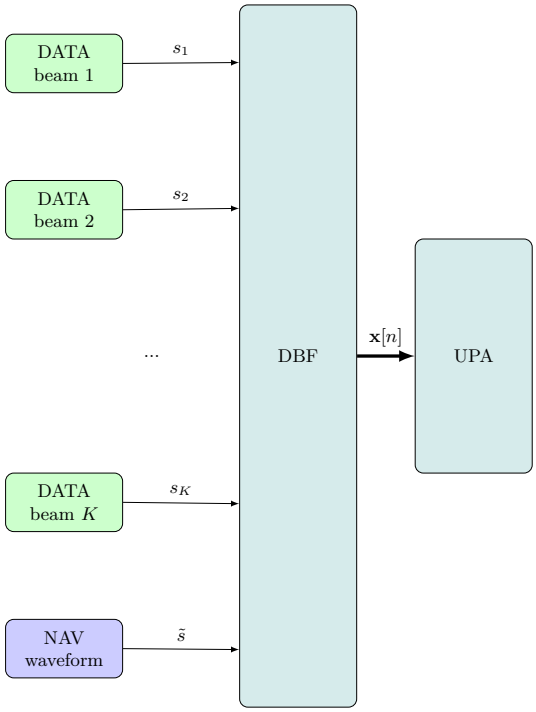

Fig. 5.4: System Diagram. Each data beam is independent and only one beam for navigation services that is independent from the data beams.

between services. Here, to achieve a specific SINR at the more distant receiver it is assumed that each beam transmits sufficient power, which is considered the worst-case scenario that needs to be addressed. Therefore, the DBF is defined as $\mathbf{W}^B = [\rho_1 \mathbf{w}_1, \ldots, \rho_K \mathbf{w}_K, \rho_{\text{NAV}} \mathbf{w}_{\text{NAV}}] \in \mathbb{C}^{N_t \times K+1}$, where ρ_k is the relative power for beam k such that $\sum_{k=1}^{K+1} \rho_k = 1$ (including ρ_{NAV}). The notation is simplified as $\mathbf{W}^{(B)} = \boldsymbol{\rho} \circ \mathbf{W}$, where $\boldsymbol{\rho} = [\boldsymbol{\rho}_{\text{DATA}} | \boldsymbol{\rho}_{\text{NAV}}] \in \mathbb{R}^{N_t \times K+1}$ is the matrix with the relative power for each beam and the elements of each column are equal.

The aggregation of both waveforms is done by adding a new port to the DBF input for the navigation signal $\mathbf{w}_{\text{NAV}}$; therefore, for the input to the DBF a matrix is created putting them side-by-side $\mathbf{s}_{\text{B}}[n] = [s_1[n], s_2[n], \ldots, s_k[n], \tilde{s}[n]]^T \in \mathbb{C}^{(K+1)\times 1}$.

Each of the N_t antennas transmits a linear combination of the $K+1$ input signals, in matrix form is defined as

$$\mathbf{x}[n] = \mathbf{W}^{(B)} \mathbf{s}_B[n] \in \mathbb{C}^{N_t \times 1}. \tag{5.5}$$

Model comparison and challenges

This subsection presents a comparison and the trade-offs for each architecture. It begin with the common benefits, then it describes each architecture particularities and challenges to

implement them and finalizing with the trade-offs.

One of the benefits from the aggregation of the DSSS and the OFDM waveforms is the time alignment of both signals, as seen in Fig. 1.4. The receiver can exploit this alignment to detect the start of the OFDM symbol. Classic algorithms such as [34] are widely used to detect the symbol start by using the CP of the OFDM symbol. However, the duration of the CP is usually kept very short to avoid inefficiencies in the transmission, and this short correlation is not reliable in scenarios with low SINR [136]. Therefore, by adding a DSSS aligned with the symbol start, a much larger sequence can be used to find the beginning of the OFDM symbol, improving detection in low-SINR scenarios such as satellite links.

Any multi-beam model can result in frequent handovers since each beam covers a small area and the satellite's motion quickly pushes users from one beam to another [137]. The downside of the shared beam is the potential need to re-acquire or adjust to the new navigation signal, which increases the reacquisition time. Therefore, the independent-beam model provides a wide-area beam for navigation that remains available across multiple spot beams [138]. This can enhance robustness during communication handover. When a user switches communication beams, the broad synchronization beam overlaps and provides a continuous reference, seamlessly transferring their timing lock and facilitating "make-before-break" handovers [138].

As a LEO satellite passes, the path loss and link geometry change constantly. When the satellite is low on the horizon, the range is longer and the signal may pass through more atmosphere. As it comes overhead, the range shortens. These variations can be on the order of dozens of dB over a pass [139]. Additionally, users might experience blockage at low angles. Beamforming networks are often designed for the worst-case (edge of beam, lowest elevation) and ensure "each beam transmits sufficient power to achieve a certain SINR at the most distant receiver" [138]. But with digital control, one can do better than a fixed worst-case design: beams can borrow power or resources from others if needed. This is related to coordinated scheduling; if one beam's link is temporarily bad (e.g. heavy rain or low elevation), the system might allocate it more time slots or concentrate array gain there, while neighboring beams back off [140].

Furthermore, both shared-beam and independent-beam models face common implementation challenges, but they manifest in slightly different ways:

- **Hardware & Complexity:** Shared beams keep hardware count lower (fewer total RF-chains/DACs). Independent beams use an extra beamformer chain increasing the hardware requirements yet offering design flexibility (different beam shapes, separate

optimization per service). Mitigation for both lies in advanced DBF, and modular array architectures to manage complexity [141].

- **Power Usage:** Fully digital payloads strain the power budget; shared beams risk extra inefficiency due to multi-signal HPA back-off, whereas independent beams need an additional amplifier but can optimize each beam's power independently. The independent model showed advantages in HPA efficiency by tailoring the nav beam transmission. Mitigation strategies include digital pre-distortion and power control to improve amplifier performance, and intelligent power sharing across beams (whichever model is used) to meet but not far exceed link requirements [142].

- **Synchronization:** Both models must tackle Doppler and timing, a challenge unique to fast LEO orbits. Shared beams deliver per-beam sync, meaning users always get a timing signal from their current beam. Independent beams can broadcast a common nav signal across the coverage, simplifying UE beam handover, but large differential Doppler must still be pre-compensated [138].

- **Interference:** In shared beams, interference is primarily inter-beams as in any multi-beam system. In independent beams, inter-service interference becomes an inter-beam issue. Notably, independent beams has a reduced interference, yielding better accuracy for the navigation service. Traditional interference countermeasures (frequency reuse patterns, polarization isolation) benefit both models [140].

- **Dynamics & Robustness:** The moving satellite scenario stresses both models. Shared beams concentrate all functions in one link, more complex handover [137]. Independent beams distribute functions, which can improve robustness (e.g. continuous nav coverage during comm handover) but adds complexity in time alignment. The independent model's wider beam inherently cover more area, which can be an advantage for providing consistent coverage during beams transitions.

Fully digital beamforming is a double-edged sword for LEO constellations [143]: it provides the tools to address LEO challenges, yet it introduces its own challenges in hardware, power, and design complexity. The shared-beam model leans toward simpler payloads, it piggybacks multiple signals in one beam, but must carefully balance their interaction and might sacrifice some performance to interference and less flexible resource allocation. The independent-beam model grants more freedom, each beam can be optimized and interference between services is reduced, yielding better overall performance at the expense of additional payload resources and coordination of parallel beams.

Table 5.1: Comparison of shared beam model and independent beam model for Joint Communication and PNT services

KPI	Shared beams	Independent beams	Rationale
Cost	✓	×	1 Less DACs and HPAs in the BFN
Flexibility	×	✓	The navigation beam can have a different shape regardless of the data beams
Compatibility	✓	×	It can work with actual payloads without adding new hardware
Performance	×	✓	The aggregated interference created by the navigation beam sidelobes is smaller.
Channel estimation	✓	×	Shared beam transmissions share the effect of the channel for both services.
Reacqusition latency	×	✓	Smaller beams require more re-aquisition of the navigation signal.

Finally, Table 5.1 summarizes the advantages and disadvantages of each model.

5.1.2 Channel model

This subsection present a channel model that differs from the channel model presented in the previous Chapter 4 as the framework defined for this and the next chapter is different. The main difference is that in the previous work there is no multiple beams, while here, yes. This important difference requires a new definition of the channel and the received signal model.

Assuming a narrowband signal that $B/f_c \ll 1$ with B being the signal bandwidth, and f_c the carrier frequency. A discrete M-tap delay line model is adopted for the channel response of path m from satellite q of beam k sampled at T_s samples per second. Where $g_{q,k,m} = |g_{q,k,m}| \exp(j\varphi_{q,k,m}) \in \mathbb{C}$ denotes the complex channel gain composed by the path loss $|g_{q,k,m}| = \sqrt{L}$ and $\varphi_{q,k,m} \in \mathcal{U}[0, 2\pi)$; $\nu_{q,k,m}$ is the Doppler frequency from path m for satellite q and beam k, $d_{q,k,m}$ represents the delay, and $(\theta^{(\mathrm{rx})}_{q,k,m}, \phi^{(\mathrm{rx})}_{q,k,m})$ are the angles of departure for path m from beam k towards the UE.

$$\mathbf{h}_{q,k,m}[n] = g_{q,k,m}\, e^{j\nu_{q,k,m} n T_s} \mathbf{a}(\theta^{(\mathrm{rx})}_{q,k,m}, \phi^{(\mathrm{rx})}_{q,k,m}) \delta[n - d_{q,k,m}] \tag{5.6}$$

As this work is on of the first of its kind (the hybridization of two waveforms), it start by evaluating only the system for a single satellite transmission. It also consider a LOS-dominated propagation scenario, typical for satellite-to-ground communications with elevation angles exceeding 30°, and a UE with an antenna with a radiation pattern similar to those found in GNSS antennas [144]. Therefore, the channel can be simplified substantially. The UE antenna is primarily a spatial filter to elevate the SINR of LOS signals from satellites, by suppressing multipath from ground. Due to the high reduction of multipath components by using these type of antenna in the UE [145, 144], and limited angular spread of the ground reflections [123], the LOS component overwhelmingly dominates, leading to

$$|\mathbf{h}^{\mathsf{H}}_{q,k,0} \mathbf{w}_{q,k}| \gg |\mathbf{h}^{\mathsf{H}}_{q,k,m} \mathbf{w}_{q,k}|, \quad m > 0, \tag{5.7}$$

Other assumption made for the channel are that the user's position and velocity remain constant throughout the measurement interval (1 ms per OFDM subframe in 5G). And, the next assumption is that the receiver has a single antenna, therefore, no beamforming from the UE side, as expected by 3GPP in its NTN scenario [146].

Therefore, this thesis reasonably adopts the simplified assumption of a single-tap LOS channel model ($M = 1$), which remains valid given the primary focus on JCAP performance analysis under LOS conditions. To reduce notation from the channel model the subindex m is removed. The notation is also further reduced from the renaming parameters driving the model between the UPA and the user u. It is defined $\mathbf{a}(\theta^{(\mathrm{rx})}_{q,k,m}, \phi^{(\mathrm{rx})}_{q,k,m}) \triangleq \mathbf{a}^T(\theta_u, \phi_u) \triangleq \mathbf{a}^T_u$. The channel model between the UPA and the user u is redefined as $\mathbf{h}_u[n] \in \mathbb{C}^{1\times N_t}$, and described by

$$\mathbf{h}_u[n] = g_u e^{j2\pi\nu_u[nT_s]}\delta[n - d_u]\mathbf{a}^T_u. \tag{5.8}$$

5.1.3 Signal models

Communication service

The waveform used for the communication service is the CP-OFDM used in 5G NTN, with a bandwidth of BW Hz, divided in N_{SC} subcarriers. The subcarrier spacing is f_{scs} and the symbol duration is $T_{\mathrm{s}} = \frac{1}{f_{scs}} + T_{\mathrm{cp}}$, where T_{cp} is the duration of the CP. Each OFDM subframe, depending on the numerology used in 5G, will have different number of OFDM symbols. However, the duration of the subframe is fixed to 1 ms. The OFDM carry only user data, modeled as a complex Gaussian random variable with 0 mean and σ^2_{OFDM} variance. Defining $\{Z^{(k)}_f\}^{N_{\mathrm{sc}}-1}_{f=0}$ as the frequency-domain data symbols (e.g., QAM symbols) assigned to each subcarrier f for the beam k. The discrete-time OFDM signal $\mathbf{z}^{(k)}$ of length N_{OFDM} for beam k is then given by the inverse discrete Fourier transform (IDFT) of the frequency-domain vector $Z^{(k)}_f$ as $\tilde{\mathbf{z}}^k = \left[z^{(k)}_0, z^{(k)}_1, \ldots, z^{(k)}_{N_{\mathrm{FFT}}-1}\right]^T \in \mathbb{C}^{N_{\mathrm{FFT}}\times 1}$. Then, it has appended the CP at the beginning of the signal, and considering a rectangular window as pulse shaping, the discrete time data signal is defined as $\mathbf{z}^k = \left[z^{(k)}_{N_{\mathrm{FFT}}-N_{\mathrm{CP}}}, \ldots, z^{(k)}_{N_{\mathrm{FFT}}-1}, z^{(k)}_0, z^{(k)}_1, \ldots, z^{(k)}_{N_{\mathrm{FFT}}-1}\right]^T \in \mathbb{C}^{N_{\mathrm{OFDM}}\times 1}$. Finally, the complete input to the BFN for all beams can be written as $\mathbf{Z} = \left[\mathbf{z}^0, \mathbf{z}^1, \ldots, \mathbf{z}^{K-1}\right]^T \in \mathbb{C}^{K\times N_{\mathrm{OFDM}}}$.

Navigation service

Now, the waveform used for the navigation service is a DSSS, composed by a low data rate service $\mathbf{b}$, a spread code $\boldsymbol{\Upsilon}$ and a pulse shaping function ξ. The low data rate service bitstream

can be modeled as a uniform random variable, defined as $\mathbf{b} = [b_0, b_1, \ldots, b_{N_b-1}]^T \in \mathbb{R}^{N_b-1\times 1}$, where N_b is the number of bits of the navigation message. The spreading code is generated by a Gold sequence, similar to GNSS. It is defined as a block code matrix $\boldsymbol{\Upsilon} \in \mathbb{C}^{N_b N_\kappa \times N_b}$, where each column κ_i corresponds to the spread code for bit i. As the spreading code is fixed for all bits (each satellite or beam has its own code), $\boldsymbol{\Upsilon}$ is constructed by repeating the spreading code along the diagonal. Let $\kappa = [\kappa_0, \kappa_1, \ldots, \kappa_{N_s-1}]^T \in \mathbb{R}^{N_\kappa-1}$ the spreading code for one bit, with $N_\kappa - 1$ as the length of the code, the block diagonal matrix is defined as $\boldsymbol{\Upsilon} = diag\{\kappa\} \in \mathbb{R}^{N_s N_\kappa \times N_s}$

The model for the DSSS waveform is $\tilde{\mathbf{z}} = \boldsymbol{\Upsilon}\mathbf{b}\xi \in \mathbb{C}^{N_s N_\kappa \times 1}$.

Considerations for the signal aggregation

Something to take into account before the aggregation of the OFDM and DSSS signals, is that they must ensure that are compatible in terms of:

- **Sampling rate** The sampling rate should be aligned at baseband. Defining the sampling rate $f_{s,\text{OFDM}}$ for the OFDM signal, and $f_{s,\text{DSSS}}$ for the navigation signal, it is possible to combine both signals by resampling at the maximum common divisor of $(f_{s,\text{OFDM}}, f_{s,\text{DSSS}})$.
- **Signal length (duration)** the signal is designed in such a way that the duration of a DSSS sequence and the duration of an 5G OFDM sub-frame are the same; therefore, after the upsampling both signals have the same number of samples.
- **Time alignment (starting point of the signals)** This is designed so that the start of the 5G sub-frame corresponds to the start of a DSSS sequence. Therefore, finding the beginning of one, the receiver knows the start of the other.

In order to have both signal synchronized and aligned, it is chosen the minimum time unit of 5G as Time Unit or T_c. Besides, using the concept of T_c defined in *TS 38.211 Section 4.1*, it is defined the duration of a navigation chip as a multiple of this $T_\text{chip} = N_\text{c} * T_\text{c}$, in this way both waveforms are synchronized at sample level.

Furthermore, to make both waveforms compatible in terms of the length, the duration of the navigation sequence is the same as the 5G subframe $T_\text{seq} = T_\text{subframe} = N_\text{chip} T_\text{chip} = N_\text{chip} N_\text{c} T_u = 1\,ms$, where N_chip are the number of chips in the sequence and N_c are the number of T_c. The value of this two parameters N_chip and N_c should be calculate in such way that also comply with the bandwidth of the DSSS waveform as [7]

$$\mathrm{BW}_{\mathrm{DSSS}} \approx \frac{2(1+\alpha)}{N_{\mathrm{c}} T_{\mathrm{c}}}. \tag{5.9}$$

Received signal model

The discrete-time received baseband signal, sampled at T_s samples per second, can be expressed as the contributions from the Q satellites in LOS and the K beams from each satellite as

$$r_u^{(\mathrm{M})}[n] = \sum_{q=1}^{Q} \sum_{k=1}^{K} r_{q,k}[n] + w[n], \tag{5.10}$$

where $r_{q,k}[n] = \mathbf{h}_{q,k}^{\mathsf{T}}[n]\mathbf{w}_{q,k}s_{q,k}[n - d_{q,k}]$ represent the signal received from satellite q and beam k, $\mathbf{w}_{q,k}$ is the steering vector for beam k at satellite q, $s_{q,k}$ is the downlink stream from satellite q and beam k, and $w[n] \sim \mathcal{CN}(0, \sigma_n^2)$ is additive Gaussian noise at the receiver.

This thesis assumes that there is only a single satellite $Q = 1$ for this initial system evaluation, as mentioned also in the previous section about the channel model. Now, it is defined the contributions of the different beams to the signal received by used u. Starting from the UPA transmission as $\mathbf{x}[n] = \mathbf{W}^{(\mathrm{MODEL})}\mathbf{s}[n]$, where $\mathbf{W} \in \mathbb{C}^{N_t \times K}$ is the DBF steering matrix, and $\mathbf{s}[n] \in \mathbb{C}^{K \times 1}$ are the K or $K+1$ data streams depending on the model. Therefore, the received signal for user u (that has a single antenna as seen in the channel model) is modeled as

$$r_u^{(\mathrm{M})}[n] = g_u e^{j2\pi \upsilon_u [nT_s]} \mathbf{a}_u^T \mathbf{W}^{(\mathrm{M})} \mathbf{s}^{(\mathrm{M})}[n - d_u] + w_u[n], \tag{5.11}$$

where $w_u[n] \in \mathcal{CN}(0, \sigma^2)$ is the receiver noise. The received signal model in (5.11) depends on the model used (M in (5.11)), it can be the shared beams or the independent beams as the steering matrix $\mathbf{W}^{(M)}$ and the modulated signal $\mathbf{s}^{(M)}$ are different.

5.1.4 Signal to interference plus noise ratio

From (5.11) the received signal can be split into three terms, the signal of interest for user u as the beam k with the better performance as $r_{u,k}$; the rest of the beams sidelobes are treated as interference as $r_{u,:}$ and the receiver noise w_u. Therefore, the expression from (5.11) is rewritten as

$$r_u^{(\mathrm{MODEL})}[n] = r_{u,k}[n] + r_{u,:}[n] + w_u[n] \tag{5.12}$$

where the signal of interest defined as

$$r_{u,k}[n] = g_u e^{j2\pi \upsilon_u [nT_s]} (\mathbf{a}_u^T \mathbf{w}_k^{(\mathrm{MODEL})}) s_k^{(\mathrm{MODEL})}[n - d_u], \tag{5.13}$$

and the interference term are the rest of the beams defined as

$$r_{u,:} = g_k e^{j2\pi\upsilon_u(nT_s)} \sum_{\substack{k=1 \\ k\neq u}}^{K} (\mathbf{a}_u^T \mathbf{w}_k) s_k[n - d_i]. \tag{5.14}$$

Assuming $\mathbb{E}\{|s_u|^2\} = P_u$ as the transmitted signal power from beam u, the signal power received is then

$$\mathbb{E}\{|r_{u,k}[n]|^2\} = L_u |\mathbf{a}_u^T \mathbf{w}_k|^2 P_u, \tag{5.15}$$

the interference from all other beams (assuming that the signals are uncorrelated)

$$\mathbb{E}\{|r_{u,:}|^2\} = L_u \sum_{\substack{k=1 \\ k\neq u}}^{K} |\mathbf{a}_u^T \mathbf{w}_k|^2 P_k, \tag{5.16}$$

and the noise power $\mathbb{E}\{|w[n]|^2\} = \sigma^2$.

The SINR received is

$$\mathrm{SINR}_u = \frac{L_u |\mathbf{a}_u^T \mathbf{w}_u|^2 P_u}{L_u \sum_{\substack{k=1 \\ k\neq u}}^{K} |\mathbf{a}_u^T \mathbf{w}_k|^2 P_k + \sigma^2}. \tag{5.17}$$

Now, depending on the signal of interest such as data, or navigation, and the model used, the expressions for the SINR can be further simplified.

SINR for shared beams model

This model is characterized by the input signal to the DBF as $\mathbf{s}^k = [\sqrt{\rho} \cdot \mathbf{z}^k + \sqrt{1-\rho} \cdot \tilde{\mathbf{z}}]$. Assuming that both signals are normalized before applying the relative weight ρ. If the interest is the communication service, $P_u = \rho$ and the navigation signal is an extra interference to the previous SINR definition. Therefore, the SINR for the communication service using this model is

$$\mathrm{SINR}_u^{(\mathrm{data})} = \frac{\rho L_u |\mathbf{a}_u^T \mathbf{w}_u|^2}{L_u |\mathbf{a}_u^T \mathbf{w}_u|^2 (1-\rho) + \rho L_u \sum_{\substack{k=1 \\ k\neq u}}^{K} |\mathbf{a}_u^T \mathbf{w}_k|^2 + \sigma^2}, \tag{5.18}$$

The SINR for the navigation service follows a similar definition

$$\mathrm{SINR}_u^{(\mathrm{nav})} = \frac{(1-\rho) L_u |\mathbf{a}_u^T \mathbf{w}_u|^2}{\rho L_u \sum_{k=1}^{K} |\mathbf{a}_u^T \mathbf{w}_k|^2 + \sigma^2}, \tag{5.19}$$

SINR for independent beams model

For this model, the definition of the SINR for each service, assuming that all signal are normalized at the input to the DBF $P_k = 1$, is just the previous definition done in (5.17), as the navigation beam is in a different beam than the communication beams.

The definition of the SINR for the communications or the navigation beams is:

$$\mathrm{SINR}_u^{(\mathrm{service})} = \frac{L_u |\mathbf{a}_u^T \mathbf{w}_u^{(\mathrm{service})}|^2}{L_u \sum_{\substack{k=1 \\ k \neq u}}^{K} |\mathbf{a}_u^T \mathbf{w}_k^{(\mathrm{service})}|^2 + \sigma^2}, \tag{5.20}$$

In this case, the weights for each service are within the respective column $\mathbf{w}_i$ at the steering matrix $\mathbf{W}^{(\mathrm{B})}$.

5.2 System optimization

As described in the previous section, to aggregate both services, it is applied different weights to each waveform, resulting in (5.18), (5.19), (5.20) for the SINR. The primary challenge addressed in this work is to determine the optimal values of the signals relative power ρ while maintaining a specific level of quality of service (QoS) for both services and then compare both systems.

This section formulates the KPI to evaluate, outline the optimization problem formulation, specify the constraints that the solution must satisfy, and present the multi-objective optimization problem by finding the Pareto front.

5.2.1 Spectral efficiency for data service

For the communication service, it is used the spectral efficiency as a key metric for optimizing the system. Considering the navigation signal and the other beams signals to be an external source of interference. The spectral efficiency is defined by Shannon as

$$\eta = \log_2 \left(1 + \mathrm{SINR}^{(\mathrm{data})}\right). \tag{5.21}$$

While spectral efficiency provides a system-level metric that is agnostic to the specific receiver implementation, it is important to note that the SINR can also be used to estimate the BER for a given modulation and coding scheme. In particular, standard analytical expressions exist that relate SINR to BER under idealized channel models, such as additive white Gaussian noise (AWGN) or Rayleigh fading, for common modulation formats (e.g.,

BPSK, QPSK, QAM). These mappings are widely used in link-level evaluations and provide a means to approximate BER from SINR. However, actual BER performance is also influenced by receiver design aspects such as synchronization, channel estimation, and decoding algorithms, which are not addressed in this system-level analysis. Therefore, while SINR-to-BER relationships are well known and could be used for approximate BER estimation, the focus on spectral efficiency in this study offers a more general and receiver-independent performance measure.

5.2.2 Range estimation accuracy for navigation service

For the navigation service, the receiver must first estimate the delay τ from the received signal, and later convert it to range. To evaluate its performance, the utilized metric is the CRLB. Following the development on [147], the CRLB for the DSSS received waveform is defined as follows:

$$\mathrm{CRLB}_{\mathrm{range}} = \frac{3T_{\mathrm{chip}}^2 c}{2\pi^2 T_{\mathrm{seq}} \left(1 - \frac{24}{\pi^2}\alpha^2 + 3\alpha^2\right) \mathrm{SINR}^{(\mathrm{nav})}}, \tag{5.22}$$

where T_{chip} is the duration of a chip, T_{seq} is the duration of the DSSS, and c is the speed of light.

5.2.3 Problem formulation

This chapter aims to design optimal values for two distinct services utilizing two different metrics: communication and navigation. To address this problem, it is defined a multi-objective function in which spectral efficiency is maximized while CRLB is minimized. Consequently, the multi-objective function is represented as $f : \chi \rightarrow \mathbb{R}^2, f(\rho) = [-\eta, \mathrm{CRLB}_{\mathrm{range}}]$, where χ denotes the feasible solution space, $\rho \in \chi$ represents the valid solutions (i.e., Pareto optimal solutions), and $f(\rho)$ is the multi-objective function to be optimized simultaneously. The negative sign in η indicates the interest in minimize it.

If one observes the metrics in (5.21) and (5.22) the reader can see that the optimization parameters depend solely on the SINR of the service. Therefore, the objective function can be minimized by directly maximizing the SINR of the communication and navigation services simultaneously. It is redefined the objective function as $f' : \chi' \rightarrow \mathbb{R}^2, f'(\rho) = \left[\mathrm{SINR}_u^{(\mathrm{MODEL,DATA})}, \mathrm{SINR}_u^{(\mathrm{MODEL,NAV})}\right]$, wherein "MODEL" is employed to distinguish the expressions for the SINR relevant to the shared beam model or the independent beam model. The optimization problem is defined as follows:

$$\rho = \arg\max_{\rho \in \chi'} f'(\rho), \tag{5.23}$$

where the constraints associated with this problem are $0 < \rho < 1$ and $\eta > 1$ as a smaller value of η does not makes sense in modern broadband communication systems.

Later for the visualization of the results, it is changed back to the original KPI, the spectral efficiency and the CRLB.

5.2.4 Pareto front definition

The Pareto front represent the tradeoff between both KPIs, where there is no room for improvement of one KPI while decresing the quality of the other. From the problem formulation in (5.23), it is used the definitions of the SINR for each model. Then, it is described the Pareto front for each model as the optimal solution. Furthermore, the following parameters are defined to reduce the notation, $\Lambda = L_u|\mathbf{a}_u^T\mathbf{w}_u|^2$, $\Xi = L_u \sum_{\substack{k=1 \\ k\neq u}}^{K} |\mathbf{a}_u^T\mathbf{w}_k|^2$, and $\Phi = L_u \sum_{k=1}^{K} |\mathbf{a}_u^T\mathbf{w}_k|^2$.

Shared beams model

By substituting the expressions (5.18) and (5.19) into (5.23), and using the notation of the previous paragraph, the Pareto curve is defined as,

$$\left\{ \left[\frac{\Lambda\rho}{\Lambda(1-\rho) + \rho\Xi + \sigma_u^2}, \quad \frac{\Lambda(1-\rho)}{\rho\Phi + \sigma_u^2} \right], \; \Big| \; \rho \in [0,1] \right\}. \tag{5.24}$$

The expression in (5.24) correspond to a Pareto front, where there is no room to improvement to one service while decreasing the quality of the other. This indicates that once the minimum SINR is established for one service (either communications or navigation), the maximum achievable SINR, and consequently the performance, for the other service is upper-bounded. Therefore, a trade-off must be determined by the system designer based on the use case requirements to meet.

Independent beam model

The Pareto front for the independent beam model is defined similarly to (5.24) in (5.25), where it is substituted the SINR functions from (5.20) with those of the independent beam model.

$$\left\{ \left[\frac{\Lambda_{\text{DATA}}}{\Xi_{\text{DATA}} + \sigma_u^2}, \quad \frac{\Lambda_{\text{NAV}}}{\Xi_{\text{NAV}} + \sigma_u^2} \right], \; \middle| \; \rho \in [0,1] \right\}, \tag{5.25}$$

where the subindex DATA or NAV correspond to the steering matrix for the data or navigation beam.

To have a common way to compare both models, it is used the parameter ρ to weight the power for each service as it is done in the shared beam model. The independent beam model has the steering weights $\mathbf{w}_i$, therefore, the parameter ρ can be extracted from each weight such that $\mathbf{w}_i = \rho_i \tilde{\mathbf{w}}_i \forall i \in \{1, \ldots, K+1\}$ in such way that $\sum_i \rho_i = 1$ and choose the navigation weight as $\mathbf{w}_{\text{NAV}} = (1 - \sum_{i=1}^{K} \rho_i)\tilde{\mathbf{w}}_{\text{NAV}}$. This way the performance of each model can be compared using only one parameter.

Pareto front description

Previously, it has been described the joint expressions for the optimal SINR for both services. These expressions define a Pareto front dependent on a single power allocation parameter, ρ, which determines the performance balance between communication (spectral efficiency) and navigation (range estimation accuracy). While ρ is often arbitrarily selected in the literature, not all values are practical. For instance, values of ρ that yield $\eta < 1$ result in very inefficient communication services.

By definition, $0 < \rho < 1$, with:

- Higher values of ρ favor communication by allocating more power to the CP-OFDM signal.
- Lower values of ρ favor navigation by allocating more power to the DSSS signal.

Although ρ can theoretically be tuned continuously, practical system constraints impose bounds on its feasible range:

- **Link budget constraints:** The navigation signal requires a minimum power to maintain lock, limiting how high ρ can be.
- **Service-level agreements:** A minimum required data throughput sets a lower bound on ρ.
- **Payload limitations:** In LEO satellites, limited transmit power restricts extreme values of ρ that might starve one service entirely, violating QoS requirements.

The selection of ρ should start from target QoS thresholds, such as:

- A minimum spectral efficiency for data service.
- A maximum allowable positioning error for navigation service.

The optimal operating point lies on the Pareto front, where any deviation degrades at least one service. In real systems, ρ can be dynamically adapted based on mission requirements or user needs. For example:

- In **GNSS-denied environments**, the network can command a lower ρ to boost navigation.
- During **data-intensive periods**, ρ can be increased to favor communication.

Concrete use cases include:

- **Communications-priority mode:** A high $\rho \to 1.0$ prioritizes data throughput, reducing positioning accuracy. This is acceptable in typical broadband services.
- **Navigation-priority mode:** A low ρ improves positioning, as needed in emergency or search-and-rescue operations, accepting lower data rates.

To implement this trade-off in real-time, the system can adopt adaptive power allocation strategies:

- The satellite's beamforming network applies weights to the composite waveform based on optimized ρ values.
- Telemetry and feedback from users allow the network to update ρ periodically to match current demands.

Additional considerations include:

- **Granularity of adjustment:** LEO dynamics require rapid adaptation, but onboard processing is limited.
- **Lookup table approach:** A pre-computed table of Pareto-optimal ρ values indexed by channel/SINR conditions can reduce computation burden.

- **Navigation continuity:** A minimum DSSS power must always be guaranteed for stable tracking, imposing a lower limit on ρ.

In summary, the parameter ρ acts as a control knob navigating the trade-off between communication and navigation. Its optimal value slides along the Pareto front and can be adjusted in real time to meet mission-specific QoS requirements under practical system constraints.

5.3 Simulations

The simulations begin with a visualization of the SINR for the optimal beam within a defined coverage area. Then it shows the complementary cumulative density function (CCDF) for the same setup but different values of ρ to evaluate its performance. Finally, it finds the Pareto fronts for different scenario by taking the best SINR (other values of SINR are suboptimal) and evaluating the KPIs.

The simulations will make use of the 3GPP 5G NTN framework, by using the parameters in their document *TS 38.821 Solutions for NR to support non-terrestrial networks (NTN) (Release 16)*. For the satellite parameters it uses the set-2 LEO-600, where the antenna model pattern is changed for an UPA. For the UE, it is used the handheld model.

To compare two reference scenarios, defined by 3GPP in its document TR 38.821 as *Scenario 24* (SC24) and *Scenario 25* (SC25), the main difference between them is that in *Scenario 24* the satellite use FFR between the beams (all beams use the same carrier frequency) and in *Scenario 25* the satellite use FR3 (the operator bandwidth is divided in three subchannels to avoid that contiguous beams transmit at the same carrier). To distinguish them easily instead of using SC24 or SC25 it will denote scenarios by FFR and FR3. The details of this system are provided in the following Table 5.2.

The 3GPP framework in Table 5.2 one can obtain:

- Number of radiating elements. $N_{t,\mathrm{DATA}} = 16 \times 16$.
- Angular separation of 6 surround beams. $\theta = 7.66°, \phi \in [0, 60, \ldots, 300]°$.

Table 5.3 shows the different scenarios with the signal bandwidth where both models have been evaluated. The rationale for these values is twofold, the larger bandwidth (30 MHz) correspond to the scenarios defined by 3GPP in its document TS 38.821, and the lower BW values correspond to the proposed work [32] as having 30 MHz, as operator, in the n256 NTN band is quite challenging in terms of licensing. Therefore in the FFR mode, the bandwidth

Table 5.2: Scenario details

Description	**Symbol**	**Value**
Satellite altitude	h	600 km
Area of observation	A	$15° \times 15°$
Carrier frequency	f_c	n256 (2.2 GHz)
Satellite EIRP density	δ_P	28 dBW/MHz
3GPP Scenario		C2
Number of beams generated	K	7(+1)
UPA Gain	G_{SAT}	24 dBi
Beam spacing in UV plane		0.1334
Number of radiating elements NAV. Independent beam model only	$N_{t,\text{NAV}}$	2×2
Radiating elements distance	$[d_x, d_y]$	$\frac{\lambda}{2}$
Data beams separation	$[\theta_k, \phi_k]$	$\theta = 0.1334$ in uv plane $\phi_k \in \{0, 60, \ldots, 300\}$
Power ratio	ρ	$0, \ldots, 1$
Total Signal bandwidth	BW	5-15-30 MHz
UE Noise Figure	NF	7 dB
UE Rx Gain	G_{Rx}	0 dBi
Duration of the sequence	T_{seq}	1 ms
5G Time unit	T_{c}	0.504 ns
DSSS pulse shaping roll-off	α	0.20
Frequency re-use factor	FRF	Option 1:1 FFR and Option 2:3 FR3

for the data service and navigation is the same, while in the FR3 mode the navigation signal use the total bandwidth and the data is divided between the beams. The main impact in the results is that the noise power levels of the receiver will be different for each scenario and service. This table also includes the parameters to generate the DSSS signal for different bandwidth, this values are obtained to meet $T_{\text{seq}} \approx N_{\text{chip}} T_{\text{chip}}$ and $T_{\text{chip}} \approx 2/BW$ (the 2 in the formula is because the DSSS sequence is real).

5.3.1 Full frequency re-use scenario

Based on the 3GPP *Scenario 24* in TS 38.821, below are the simulation results for the performance of the joint communication and navigation signal using the parameters in Table 5.2 for each payload model. In this scenario, there is FFR, therefore all beams transmit a signal using the 30 MHz of bandwidth. This scenario is known as single frequency network (SFN), and it is normally used as a broadcasting system [148].

Table 5.3: Scenarios bandwidth

Scenario	BW data	BW NAV	Number of 5G Time units per chip N_c	Number of chips per sequence N_{chip}	$T_{\text{chip}} = N_c T_c$
FFR	30 MHz	30 MHz	160	12288	81.44 ns
FFR	5 MHz	5 MHz	960	2066	483 ns
FR3	10 MHz	30 MHz	160	12288	81.44 ns
FR3	5 MHz	15 MHz	320	6200	161 ns

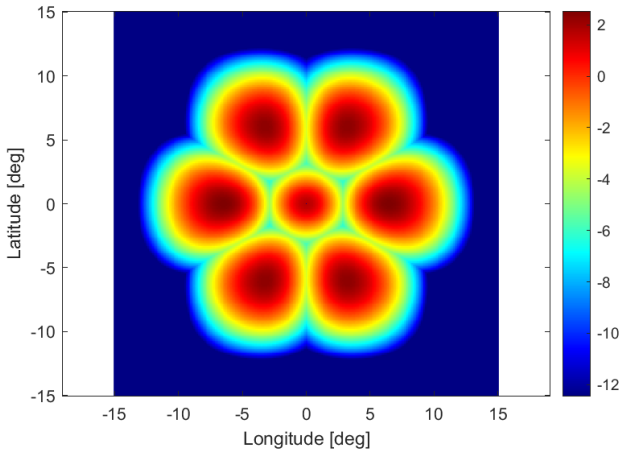

Fig. 5.5: FFR. Shared beam model. SINR [dB] reference for the Data beams.

Shared beam model

Two reference simulations are used as starting point, Fig. 5.5 shows one when $\rho = 1$, there is no navigation signal. Therefore, this system is the standardized by 3GPP as *Scenario 24* where there is FFR in the beams; and a second simulation in Fig. 5.6 with $\rho = 0$, when only the navigation signal is transmitted through this model. As the system is symmetric from (5.24), both Fig. 5.5 and Fig. 5.6 are the same.

Then, to evaluate the performance with different values of ρ, Fig. 5.7 shows the CCDF of the SINR in the area of coverage of the beams for different values of ρ. This CCDF represent the percentage of users with a SINR higher than a certain value. The areas with a SINR $\geq -7\ dB$ are selected as is the minimum value to work with before the channel coding gain. Furthermore for the navigation part they have added the correlation gain, that for the sequence length used is 30 dB. It is interesting to see how the CCDF for the data beams remain almost the same for the different values of ρ, while the navigation beams shows an improvement while decreasing ρ.

The improvement in the navigation SINR decreasing the value of ρ can be seen in Fig. 5.7

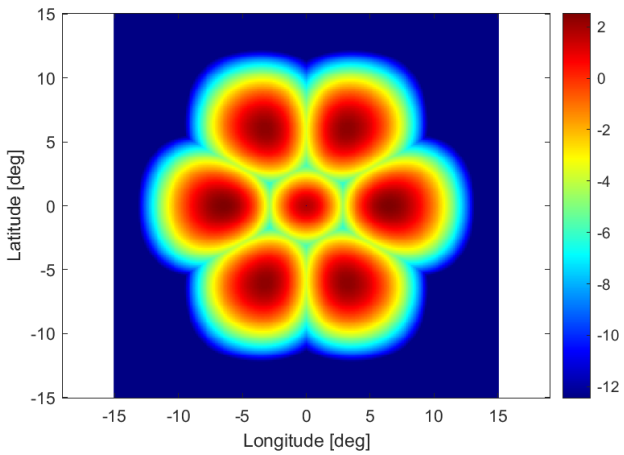

Fig. 5.6: FFR. Shared beam model. SINR [dB] reference for the Navigation beams.

from the shape of the Pareto front from (5.24).

Independent beam model

The analysis done for the independent beam model is similar to the analysis done for the shared beam model, it differs as now the navigation beam is much wider and this single wide beam generates interference in all data beams.

Fig. 5.8 shows one when $\rho = 1$, there is no navigation signal. Therefore, this system is the standardized by 3GPP as *Scenario 24* where there is FFR in the beams; and a second simulation in Fig. 5.9 with $\rho = 0$, when only the navigation signal is transmitted through this model. As the system is asymmetric from (5.25), both Fig. 5.8 and Fig. 5.9 are the now different showing each service a different coverage area.

Then, to evaluate the performance with different values of ρ, Fig. 5.10 shows the CCDF of the SINR in the evaluated area for different values of ρ. It is interesting to see how the CCDF for the data beams remain almost the same for the different values of ρ, while the navigation beams shows an improvement while decreasing ρ. They have a lower SINR than Fig. 5.7 as the surface covered by large power of the navigation beam is larger than in the shared beam model. This can be solved in a future research by designing a isoflux beam for navigation, similar to the ones used by GNSS [149].

The improvement in the navigation SINR decreasing the value of ρ can be seen in Fig. 5.10 from the shape of the Pareto front from (5.25).

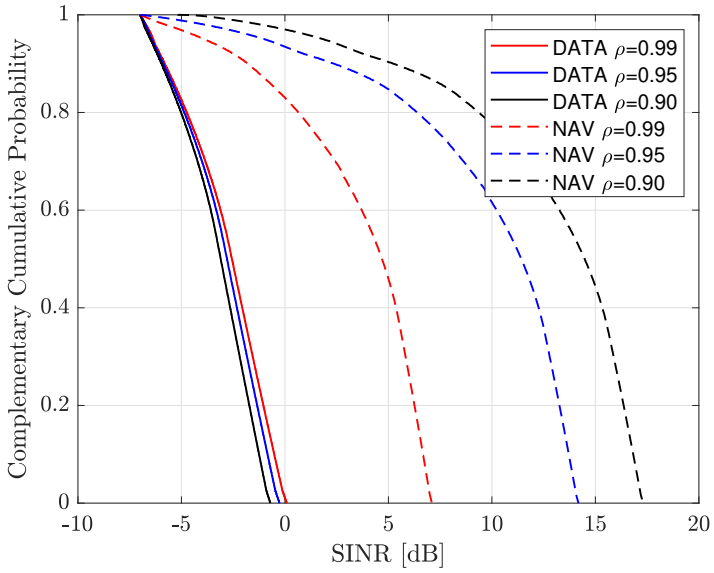

Fig. 5.7: FFR. Shared beam model. Complementary Cumulative Density Function of the SINR in the area of interest for different values of ρ.

5.3.2 Frequency re-use factor 3 scenario

In this scenario 25, there is a three color frequency reuse or FR3, therefore the total 30 MHz of the bandwidth is divided in three blocks of 10 MHz according to the *Option 2* from TS 38.821. Still use the 30 MHz for the navigation signal, in the independent beam model.

Shared beam model

A reference simulation is used as beginning, Fig. 5.11 shows one when $\rho = 0.98$. Therefore, this system is the standardized by 3GPP as *Scenario 25* where there is a FR3 in the beams.

Then, to evaluate the performance with different values of ρ, Fig. 5.12 shows the CCDF of the SINR in the evaluated area for different values of ρ. It is interesting to see how the CCDF for the data beams remain almost the same for the different values of ρ, while the navigation beams shows a larger improvement while decreasing ρ.

The improvement in the navigation SINR decreasing the value of ρ can be seen in Fig. 5.12.

Independent beam model

Reference simulation in Fig. 5.13 shows when $\rho = 0.98$. Therefore, this system is the standardized by 3GPP as *Scenario 25* where there is a FR3 in the beams.

Then, to evaluate the performance with different values of ρ, Fig. 5.14 shows the CCDF

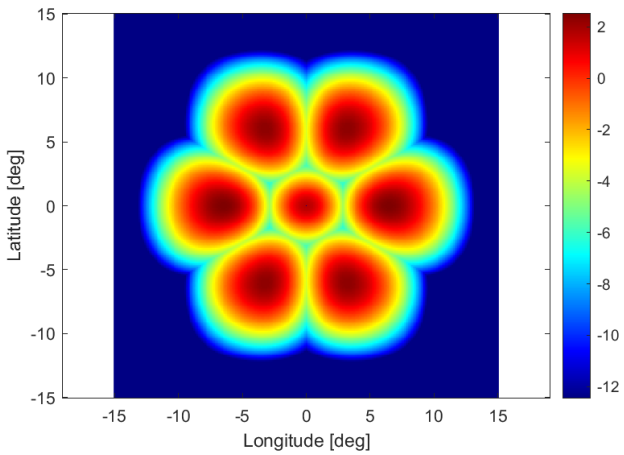

Fig. 5.8: FFR. Independent beam model. SINR [dB] reference for the Data beams.

of the SINR in the evaluated area for different values of ρ. It is interesting to see how the CCDF for the data beams remain almost the same for the different values of ρ, while the navigation beams shows an improvement while decreasing ρ.

The improvement in the navigation SINR decreasing the value of ρ can be seen in Fig. 5.14.

5.3.3 Results discussion and models comparison

The previous simulations to generate Figures 5.5, 5.6, 5.8, 5.9, 5.11, and 5.13 were performed utilizing specific values for ρ. To conduct a comprehensive evaluation of the system, the simulation has been repeated with a range of values for ρ.

The best SINR is obtained at the user terminal for both services for each value of ρ to obtain the spectral efficiency η and the CRLB for the range estimation using the navigation signal. Fig. 5.15 shows the results of the simulation for each model, different values of ρ and the scenario configurations from Table 5.3. It presents the best spectral efficiency achieved for the data signal and the best accuracy on the range estimation using the navigation signals. This result provides insights into the impact of the different parameters on system performance. Furthermore, the performance with a JCAP system that uses the PRS as a positioning pilots within 5G communication service is compared. The plots of the reference JCAP system are generated by using the definition of spectral efficiency η and the CRLB for the OFDM PRS system, defined as $\eta = \left(1 - \frac{N_{\text{pilots}}}{N_{\text{total}}}\right) \log_2(1 + \text{SINR})$ where N_{pilots} are the subcarrier in a symbols dedicated to pilots and N_{total} are the total number of subcarriers.

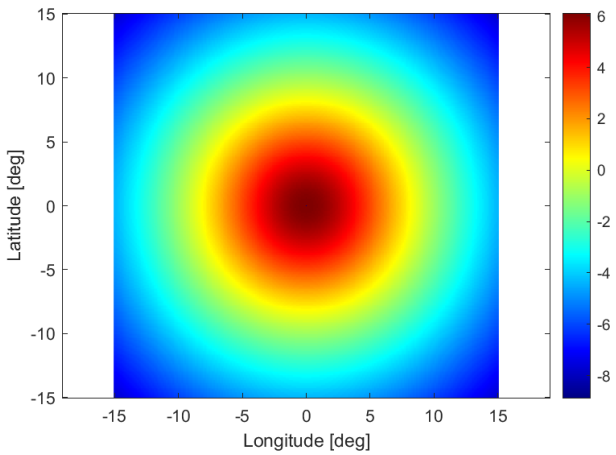

Fig. 5.9: FFR. Independent beam model. SINR [dB] reference for the Navigation beams.

Then for the range estimation it is used $\sigma^2_{CRLB} = \frac{6c}{8\pi^2 \text{SINR} \Delta f^2 M N_{\text{pilots}}(N_{\text{pilots}}-2)(N_{\text{pilots}}-1)}$, where c is the speed of light, Δ_f^2 is the subcarrier spacing, and M is the number of symbols with the PRS. It is assumed a subcarrier spacing $\Delta f = 30$ kHz (the one standardized for n256 NTN band), and the number of subcarriers $N = [165, 500, 1000]$ for 5 MHz, 15 MHz and 30 MHz.

The results in Fig. 5.15 emphasizes that improving one metric comes at a cost to the other. Solutions below the curve are infeasible, they would require more power than available. Solutions above the curve are sub-optimal. The goal of the multi-objective optimizer is to output the Pareto front, so that system designers can pick an operating point appropriate for the mission (or even schedule different points at different times). For instance, one end of the Pareto front corresponds to maximum navigation accuracy (but poor data rate), and the opposite end to maximum data rate (but poor accuracy). Fig. 5.15 shows this trade-off explicitly: spectral efficiency vs. ranging CRLB is plot for various ρ and highlights how one model or scenario dominates another in different regions. Such Pareto front diagrams are invaluable for designers to visually grasp the compromise and select ρ according to current needs.

Furthermore, the results in Fig. 5.15 only show the values where $\eta > 1$, as values with a spectral efficiency below 1 [bps/Hz] are hardly justifiable by design in modern broadband wireless communications systems. Table 5.4 shows the minimum value for ρ_{min} to achieve a minimum efficiency of 1 [bps/Hz] and the CRLB achieved at that value of ρ_{min}.

Table 5.4 shows a summary of the results: for a FFR scenario with 30 MHz signals (FFR 30/30), to maintain at least 1 bps/Hz data efficiency the power split had to be $\rho \approx 0.78$

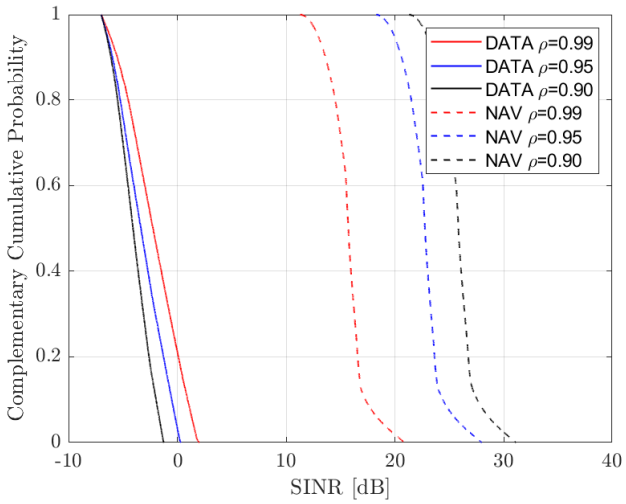

Fig. 5.10: FFR. Independent beam model. Complementary Cumulative Density Function of the SINR in the area of interest for different values of ρ.

(shared-beam model), resulting in a CRLB implying about 3.5 cm range error. Pushing ρ any lower in that scenario caused spectral efficiency to dip below 1 bps/Hz (unacceptable for broadband service).

On the other hand, in a more benign interference scenario (FR3 with 15 MHz data and 5 MHz nav), a balance was found around $\rho \approx 0.54$ for the shared-beam case, yielding 1.9 cm range accuracy at 1 bps/Hz. If ultra-high accuracy were needed, ρ would be tuned even lower – but then the spectral efficiency would drop below the 1 bps/Hz threshold. These numbers demonstrate the practical performance variations: shifting ρ by a few tens of percentage points can swing the spectral efficiency from sub-1 to over 2 bps/Hz. Operators can use such

Table 5.4: Minimum usable ρ to get at least $\eta \geq 1$ and the accuracy obtained in the range estimation

Scenario	Signal BW	**Model**	$\rho_{\min}$	σ_{range}[cm]
FFR	30/30	Shared beams	0.78	3.49
FFR	30/30	Independent beams	0.94	2.84
FFR	5/5	Shared beams	0.55	1.71
FFR	5/5	Independent beams	0.875	**1.61**
FR3	30/10	Shared beams	0.59	2.36
FR3	30/10	Independent beams	0.88	2.10
FR3	15/5	Shared beams	0.54	1.90
FR3	15/5	Independent beams	0.87	1.77

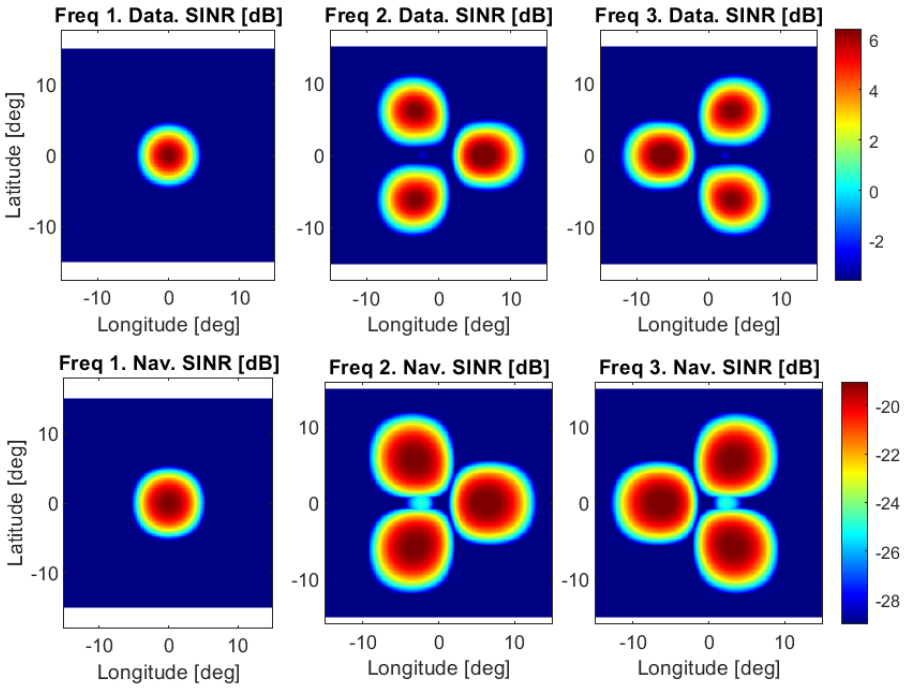

Fig. 5.11: FR3. Shared beam model. SINR [dB] reference for the Data and navigation beams.

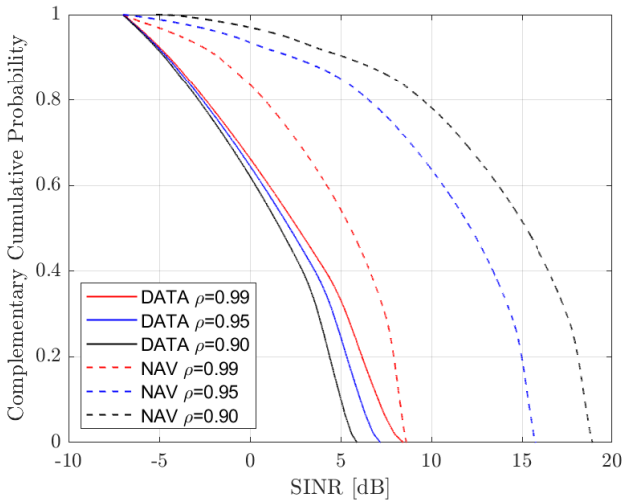

Fig. 5.12: FR3.Shared beam model. Complementary Cumulative Density Function of the SINR in the area of interest for different values of ρ.

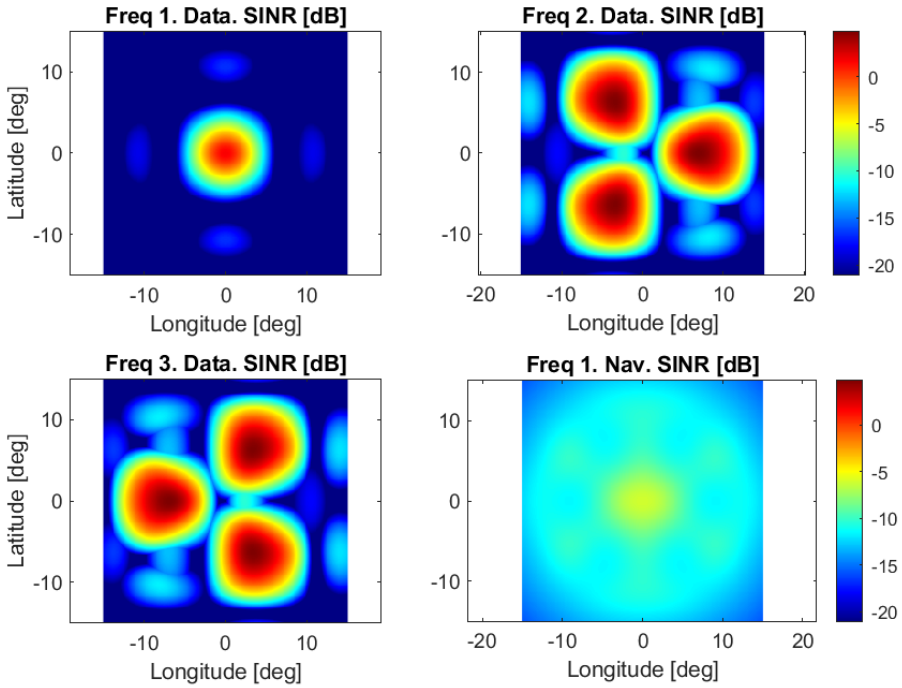

Fig. 5.13: FR3. Independent beam model. SINR [dB] reference for the Data and navigation beams beams.

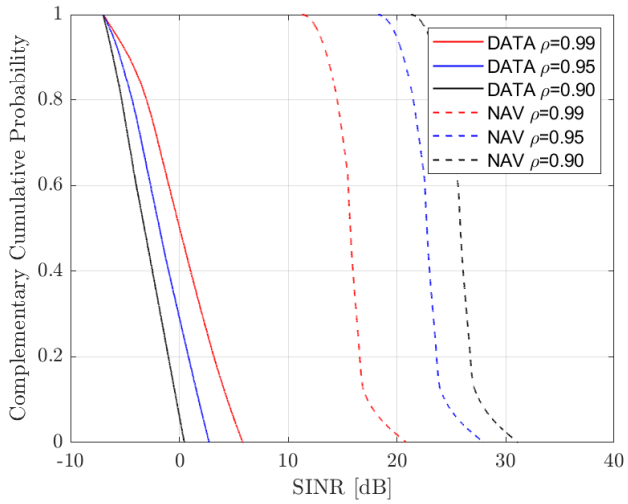

Fig. 5.14: FR3. Independent beam model. Complementary Cumulative Density Function of the SINR in the area of interest for different values of ρ.

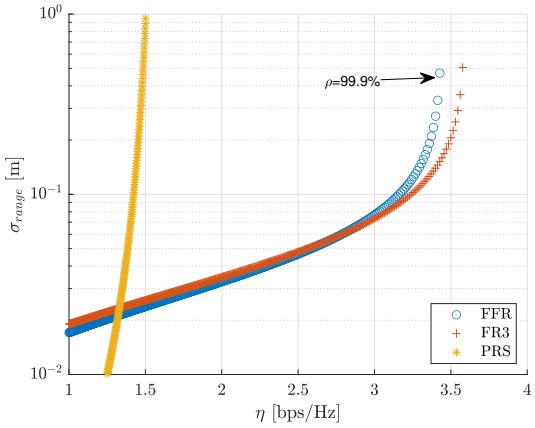

(a) Small BW. Shared beams

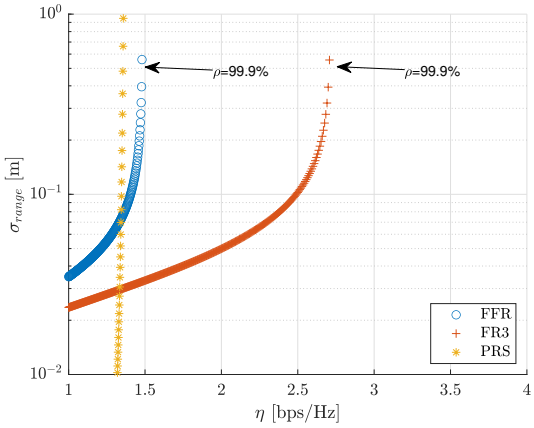

(b) Large BW. Shared beams

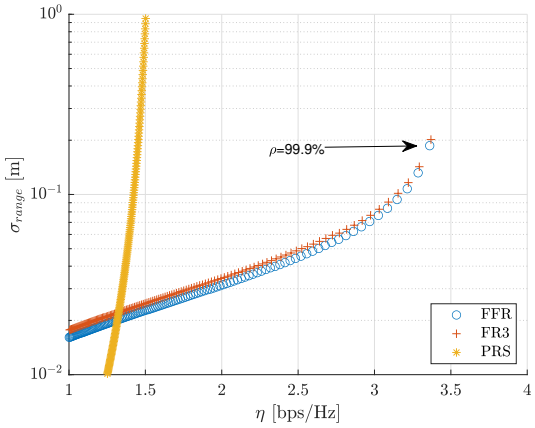

(c) Small BW. Independent beams

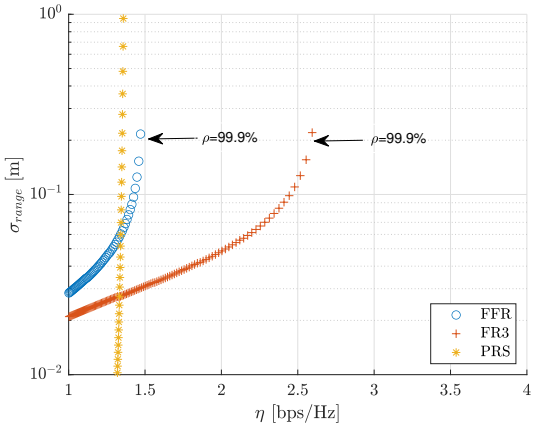

(d) Large BW. Independent beams

Fig. 5.15: Spectral efficiency η and CRLB comparison between shared beam model and independent beams in the different scenarios from Table 5.3. Also for the large bandwidth a comparison from using the 5G PRS as positioning signal.

data to decide ρ based on requirements: e.g. if a use-case demands ≤ 1 m accuracy, one must operate on the lower-ρ end of the Pareto front (and tolerate the corresponding throughput reduction).

As the reader can observe in Fig. 5.15 and Table 5.4 the use of FR3 is outperforming FFR. This is expected as a FFR mode has a large impact in the interference of nearby beams, while FR3 reduces this interference. Now related to the use of a shared or independent beams model, from Table 5.4 at equal configuration, the independent model outperform the shared beam model. Therefore, the independent model has a higher spectral efficiency. This can be explained as in the shared beam model, each beam transmit two signals, and the side lobes of each beam aggregate reducing the SINR. However, in the independent beam model, for the navigation service, there is only one large beam that generate interference to the data, and only seven beams of data that interfere with the navigation, so the aggregation of the sidelobes signals is much smaller, making this independent beam model a better option for a JCAP system.

It is helpful to quantify how different choices of ρ affect communication and positioning performance. Consider a simplified case with one beam and a fixed total power. If $\rho = 0.8$ (80% power to data), the communication SINR might be quite high. For instance, plugging into the Shannon formula gives a spectral efficiency on the order of 2 bps/Hz, whereas the navigation SINR is relatively low, yielding a high CRLB (poor accuracy). If instead it is chosen $\rho = 0.2$ (only 20% to data, 80% to nav), the roles reverse: spectral efficiency drops to about 0.3 bps/Hz while the positioning accuracy improves. This means the range error could be, say, 2–4 times smaller when navigation is prioritized, at the expense of an order-of-magnitude lower data rate.

This system can comply with the accuracy requirements for several of the 5G positioning use cases from [3] and [14] as detailed in Table 2.1.

5.4 Summary

This chapter presents two novel system architectures—shared beam and independent beam—to deliver JCAP services from LEO multi-beam satellites. Both architectures integrate a 5G-compliant OFDM waveform for communication and an overlay DSSS waveform for navigation. Through extensive simulation, the chapter evaluates trade-offs between spectral efficiency and positioning accuracy, characterizing the Pareto optimal boundary for the SIR between the two waveforms. The independent beam model emerged as superior in overall performance, providing higher spectral efficiency and improved accuracy

due to reduced mutual interference between the communication and navigation signals.

The analysis concluded that the frequency reuse factor significantly impacts JCAP performance, with the FR3 scenario outperforming the FFR scenario due to lower inter-beam interference. Results demonstrated that the hybrid waveform approach consistently achieved positioning accuracies at centimeter-level while maintaining acceptable data rates compliant with 5G requirements, confirming its feasibility and efficiency in practical NTN deployments. Furthermore, the overlay DSSS approach enables smooth integration with legacy OFDM-based 5G infrastructures, minimizing necessary payload modifications and ensuring backward compatibility.

Building on the waveform and architecture concepts introduced in this chapter, Chapter 6 develops a novel receiver architecture explicitly designed to exploit this hybrid OFDM-DSSS waveform. The receiver integrates navigation and communication functionalities into a unified framework, leveraging the DSSS signal's channel parameter estimations (such as delay and Doppler) to enhance the OFDM data demodulation process. This architecture demonstrates significant performance gains, particularly in robust signal detection and improved BER, underscoring the practical benefits and system-level efficiency of the proposed hybrid JCAP solution.

Chapter 6

Receiver architecture for joint communication and positioning

This last technical chapter shows a novel JCAP receiver architecture that use the hybrid waveform designed in the previous chapter. It details a specific scenario for the use of this hybrid waveform. Then, it presents the receiver architecture tat combines the channel parameters to improve the communication service. Finally, it presents the performance evaluation of this receiver architecture in the scenario modelled. The work presented in this chapter has been accepted for publication in the open journal of the communication society.

6.1 System model

This section introduces the mathematical models utilized in this chapter. Part of the models used in this work are already defined in the previous Chapter 5, such as: the antenna beamforming model defined in Section 5.1.1, implemented by the LEO satellite payload; the channel model in Section 5.1.2; and the received signal model in Section 5.1.3.

Therefore, this section details the implementation of the shared beam model from Section 5.1.1 and it narrow down the definition of the SINR of the received signal under this model.

6.1.1 Hybrid downlink waveform

The hybrid waveform selected for this work corresponds to the *shared beam* model under the FR3 scenario discussed in the previous Chapter 5. The choice of this waveform structure is

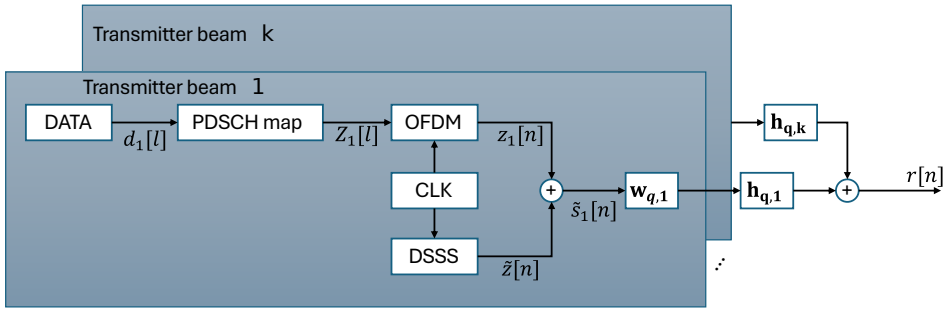

Fig. 6.1: Transmitter architecture for satellite q integrating DSSS and OFDM waveforms for JCAP services.

motivated by its minimal impact on the satellite payload architecture, specifically avoiding modifications to the established DBF configuration, and its backward compatibility with non-JCAP receivers, enabling straightforward deployment in existing software-defined payloads via firmware updates [150, 151]. Here it is presented a brief summary of it and the implementations details used in this chapter.

The hybrid transmitter consists of the input bitstream from the upper layers, which are then subsequently mapped into the physical downlink shared channel (PDSCH) and modulated using OFDM according to the 3GPP specifications. Concurrently, a DSSS signal is generated and combined with the OFDM waveform, ensuring a predefined SIR $\mathrm{SIR}_{\mathrm{DSSS}} = \rho$ (where the signal is the communication service and the interference is the DSSS). Here it is assumed the value of ρ is the same for all satellites. The aggregation is performed by aligning the beginning of the DSSS waveform with the start of the 5G subframe, resulting in identical durations (1 ms) and sampling frequencies f_s for both waveforms. Finally, the aggregated waveform is processed through the DBF matrix.

The channel model described by (5.6) is then applied to the transmitted waveform to emulate the channel impairments and generate the received signal $r[n]$. The overall transmitter architecture, including the channel response $\mathbf{h}$ for each beam, is depicted in Fig. 6.1. Where each beam k in Fig. 6.1 simultaneously transmits the hybrid waveform at a sampling frequency $f_s = 1/T_s$, defined as in (5.3)

The time-domain OFDM signal $z_{q,k}[n]$ has a length (in samples) that depends on the RB used. The number of RB defined as N_{RB}, are blocks of 12 subcarriers and define the bandwidth of the signal. This also defined the length of the DSSS as they are synchronized to have the same length in samples. Both signals share a common sampling clock at f_s rate, thus ensuring coherent alignment at sample-level as illustrated in Fig. 1.4.

6.1.2 Signal to interference plus noise ratio analysis

This (5.10) is divided in terms of the signal of interest $r_{g,i}[n]$ from satellite g and beam i, and treat the rest of satellites and beams as interference plus the receiver noise. This model is as follows

$$r[n] = r_{g,i}[n] + \sum_{k\neq i}^{K} r_{g,k}[n] + \sum_{q=1}^{Q}\sum_{k=1}^{K} r_{q,k}[n] + w[n]. \tag{6.1}$$

The effective scalar channel gain is defined for beam k from satellite q assuming a stationary channel over the time of observation, and considering only the LOS path (as seen in the channel model subsection), it is defined the following

$$h_{q,k} \triangleq \mathbb{E}\{|\mathbf{h}_{q,k}^{\mathsf{T}}[n]\mathbf{w}_{q,k}|^2\} = \mathbb{E}\{|\alpha_{q,k}|^2\}|\mathbf{a}^{\mathsf{T}}(\theta_{q,k}^{(\mathrm{rx})}, \phi_{q,k}^{(\mathrm{rx})})\mathbf{w}_{q,k}|^2 = |\mu_q|^2|\mathbf{a}^{\mathsf{T}}(\theta_{q,k}^{(\mathrm{rx})}, \phi_{q,k}^{(\mathrm{rx})})\mathbf{w}_{q,k}|^2, \tag{6.2}$$

where μ_q represent the path loss due to the distance between the UE and the different satellites q.

By using the definition of $h_{q,k}$ as an scalar that represent the power loss due to the channel at the UE for the different elements in the system, to analyze the SINR the following quantities are defined

$$\mathbb{E}\{|\mathbf{h}_{g,i}^{\mathsf{T}}[n]\mathbf{w}_{g,i}\sqrt{1-\rho}z_{g,i}[n-d_{g,i}]|^2\} = (1-\rho)h_{g,i}, \tag{6.3}$$

$$\mathbb{E}\{|\mathbf{h}_{g,i}^{\mathsf{T}}[n]\mathbf{w}_{g,i}\sqrt{\rho}\tilde{z}[n-d_{g,i}]|^2\} = \rho h_{g,i}, \tag{6.4}$$

$$\mathbb{E}\{|\sum_{k\neq i}^{K}\mathbf{h}_{g,k}^{\mathsf{T}}[n]\mathbf{w}_{g,k}s_{g,k}[n-d_{g,k}]|^2\} = R_K, \tag{6.5}$$

$$\mathbb{E}\{|\sum_{q\neq g}^{Q}\sum_{k=1}^{K}\mathbf{h}_{g,k}^{\mathsf{T}}[n]\mathbf{w}_{g,k}s_{g,k}[n-d_{g,k}]|^2\} = R_Q. \tag{6.6}$$

The resulting SINR for the 5G waveform component from satellite g and beam i can thus be expressed as

$$\gamma_{z,g,i} = \frac{(1-\rho)\,h_{g,i}}{\rho h_{g,i} + R_K + R_Q + \sigma_n^2}, \tag{6.7}$$

and similarly, the SINR for the DSSS waveform component from the same satellite and beam is given by

$$\gamma_{\tilde{z},g,i} = \frac{\rho h_{g,i}}{(1-\rho)h_{g,i} + R_K + R_Q + \sigma_n^2}. \tag{6.8}$$

These expressions form the analytical basis for the evaluation of communication performance within the proposed JCAP system. It can be seen that the impact the other beams R_K or satellites R_Q is the same for both services.

6.2 Receiver architecture

This section details the proposed hybrid receiver architecture. This receiver is designed to jointly integrate navigation and communication functionalities within a single receiver structure. Leveraging mutual interactions between both services as depicted in Fig. 1.3, the proposed architecture aims to enhance overall performance by exploiting the complementary information provided by each subsystem.

6.2.1 Navigation receiver

It is required at least 4 parallel channels as a minimum of 4 satellites are needed for an estimation of the UE state $[x, y, z, t_{\text{sat}}]$. This section shows the details of one of these channels, as the only difference between each channel is the local copy of the DSSS. Each channel consists of several processing stages as detailed below and presented in Fig. 6.2.

The navigation receiver architecture is inspired by the work in [152]. Fig. 6.2 shows a single channel for a navigation receiver, and as part of a navigation receiver, the observables to fed the PNT engine estimated in this block are:

- Noise estimation $P_{in,g,i}$.
- Delay estimation $\hat{d}_{g,i}$.
- Doppler estimation $\hat{\nu}_{g,i} = \hat{\nu}^{(CA)} + \hat{\nu}_p$.
- Phase estimation $\hat{\varphi}_{g,i}$.

There are several PNT engines in the literature such as the ones found in [7]. Depending how the PNT engine is implemented, it will make use of some of the observables or all of them. A PNT engine implementation is described in Appendix C.

Furthermore, the output of this navigation block is the received signal after compensating for the channel impairments ready for its demodulation as $\hat{s}_k[n]$.

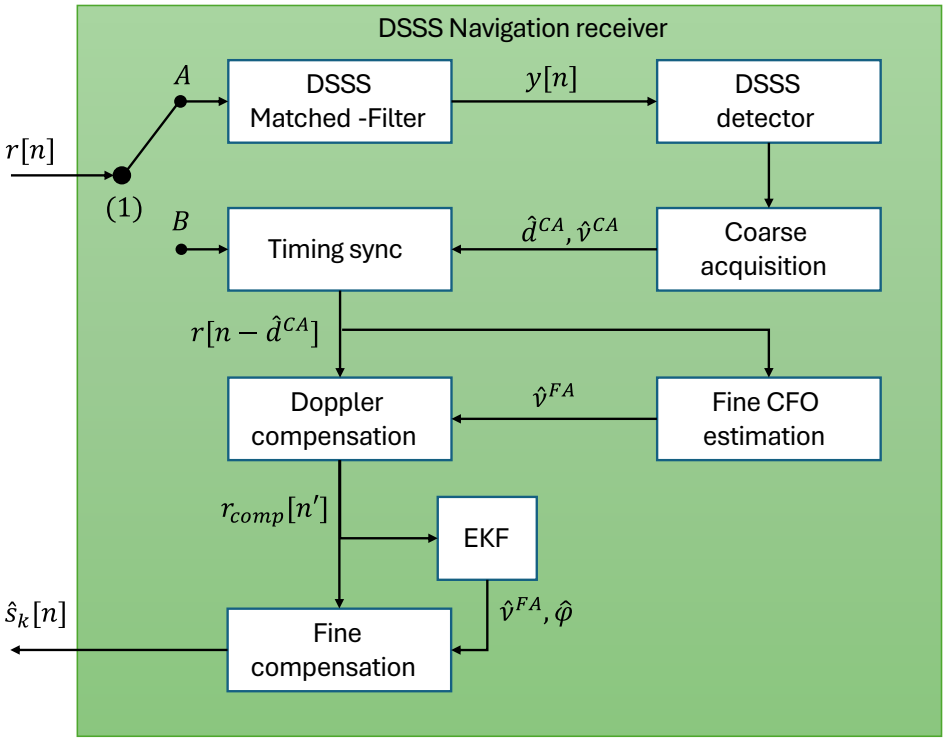

Fig. 6.2: Single channel navigation receiver architecture. The complete navigation receiver is composed by several channels running in parallel, each for a different DSSS.

Signal switch

This initial switch is used to route the received signal between different steps in a similar to the architecture designed in [152] for the 5G signals. The main rationale to use this switch is that the initial coarse acquisition is required only once, at the beginning of the reception. Then, the tracking loops enter into action for the small adjustments of the estimations. However, if the tracking loops lost the track of the signal, the switch is then changed back to its initial position.

The input signal switch (1) is managed by the action of the DSSS detector. Initially, when the DSSS is undetected, the input is routed through (1)-A, enabling coarse estimation of delay and Doppler parameters $(\hat{\tau}_q, \hat{\nu}_q)$. Upon detection of the DSSS waveform, the connection switches to (1)-B and stay in this state while the tracking loops keep the signal track.

DSSS matched filter

The DSSS matched filter performs coherent correlations over N_ν Doppler bins defined in the interval $[-\nu_{D_{\mathrm{MAX}}}, \ldots, \nu_{D_{\mathrm{MAX}}}]$, where $\nu_{\mathrm{D_{MAX}}}$ is the maximum Doppler shift expected and it

will depends on the orbit altitude and f_c. Besides, the correlation is done for integer delay lags $d = 0, \ldots, L_c - 1$, with L_c the length of the DSSS. Therefore, the matching filter is defined as

$$R_{r,\tilde{z}}[d,\nu] = \frac{1}{\sqrt{1-\rho}} \sum_{n=0}^{L_c-1} r[n+d]\tilde{z}^*[n]e^{j2\pi\nu n T_s}. \tag{6.9}$$

Expanding (6.9) using (6.1) can be approximated to (6.10).

$$R_{r,\tilde{z}}[d,\nu] \approx L_c \mathbf{h}_{g,i}^{\mathsf{T}}[d_{g,i}]\mathbf{w}_{g,i}\delta[d-d_{g,i}]\delta[\nu-\nu_{g,i}] + X_z[d,\nu] + X_K[d,\nu] + X_Q[d,\nu] + X_{w'}[d,\nu], \tag{6.10}$$

where to reduce notation the following terms are defined

$$X_z[d,\nu] = \frac{\sqrt{\rho}}{\sqrt{1-\rho}} \sum_{n=0}^{L_c-1} \mathbf{h}_{g,i}^{\mathsf{T}}[n+d]\mathbf{w}_{g,i} z_{g,i}[n+d-d_{g,i}]\tilde{z}^*[n]e^{j2\pi\nu n T_s}, \tag{6.11}$$

$$X_K[d,\nu] = \frac{1}{\sqrt{1-\rho}} \sum_{n=0}^{L_c-1} \sum_{k\neq i}^{K} r_{g,k}[n+d]\tilde{z}^*[n]e^{j2\pi\nu n T_s}, \tag{6.12}$$

$$X_Q[d,\nu] = \frac{1}{\sqrt{1-\rho}} \sum_{n=0}^{L_c-1} \sum_{q\neq g}^{Q} \sum_{k=1}^{K} r_{q,k}[n+d]\tilde{z}^*[n]e^{j2\pi\nu n T_s}, \tag{6.13}$$

$$X_{w'}[d,\nu] = \frac{1}{\sqrt{1-\rho}} \sum_{n=0}^{L_c-1} w_{q,k}[n+d]\tilde{z}^*[n]e^{j2\pi\nu n T_s}. \tag{6.14}$$

These residual terms can be approximated as a random Gaussian variable $\{X_z, X_K, X_Q, X_w\} \sim \mathcal{CN}(0,\sigma^2)$, the value of σ^2 will be different for each residual term. The residuals represent the interference after the matched filter from the data service in: the same beam and satellite (as X_z); the interference from other beams in the same satellite (as X_K); the interference from other beams from satellites (as X_Q); and the receiver noise contribution (as X_w). All of them are independent of the delay d and the Doppler ν, and the σ^2 for each contribution is

$$\sigma_z^2 = \frac{1-\rho}{\rho} h_{g,i}, \tag{6.15}$$

$$\sigma_K^2 = \frac{R_K}{\rho}, \tag{6.16}$$

$$\sigma_Q^2 = \frac{R_Q}{\rho}, \tag{6.17}$$

$$\sigma_{w'}^2 = \frac{\sigma_w^2 L_c}{\rho}. \tag{6.18}$$

These values of σ show that the closer ρ is to 0, the higher the contribution of the OFDM and the other signals to the DSSS of interest.

DSSS detector

The detection stage employs a cell averaging (CA)-constant false alarm rate (CFAR) algorithm, as described in [113], to ascertain the presence of the DSSS signal. The detector evaluates the correlation peak $\max(|R_{r,\tilde{z}}[d,\nu]|)$ against a dynamically computed threshold $\eta = \beta P_{in}$. The β is obtained from the probability of false alarm P_{fa} parameter as

$$\beta = M_d M_\nu (P_{fa}^{\frac{-1}{M_d M_\nu}} - 1). \tag{6.19}$$

where M_d is the number of training samples for the noise estimation in the time axis and M_ν the number of training samples in the Doppler bins axis.

The noise estimation P_{in} used in the threshold calculation is computed as the power of the signal within the subset of the acquisition samples centered in the position of $< d_0, \nu_0 >= \text{argmax}_{d,\nu}(|R_{r,\tilde{z}}[d,\nu]|)$ defined by

$$\mathcal{I}_{M_d}[d_0] = \{d_0 - \frac{M_d}{2}, \cdots, d_0, \cdots, d_0 + \frac{M_d}{2}\}, \tag{6.20}$$

$$\mathcal{I}_{M_\nu}[\nu_0] = \{\nu_0 - \frac{M_\nu}{2}, \cdots, \nu_0, \cdots, \nu_0 + \frac{M_\nu}{2}\}. \tag{6.21}$$

Another set is defined for the guard area as

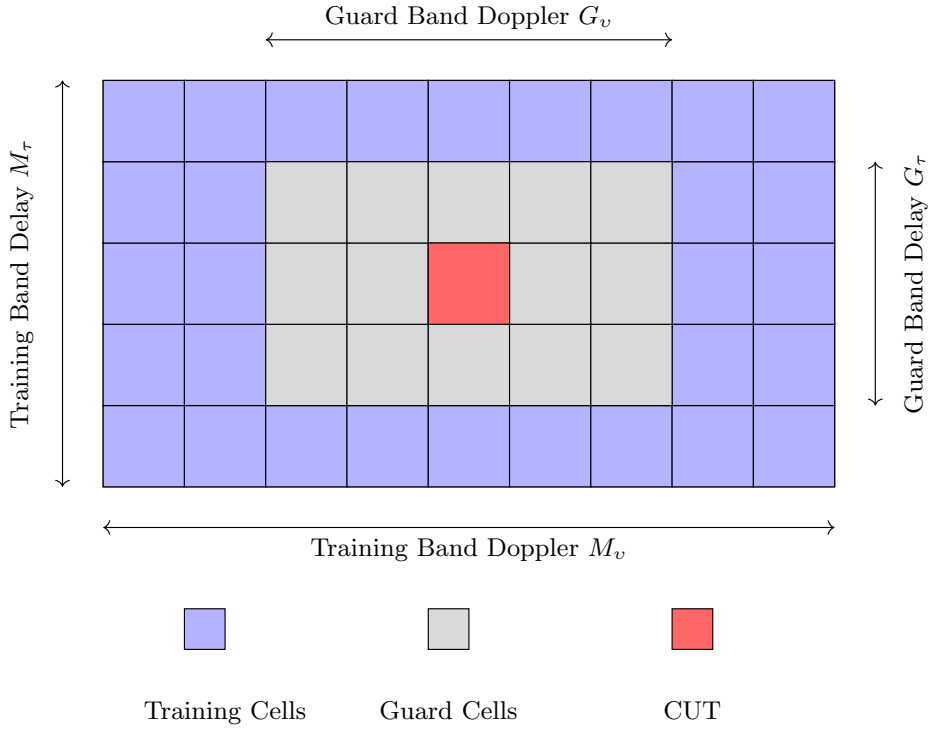

Fig. 6.3: 2D CA-CFAR algorithm

$$\mathcal{I}_{G_d}[d_0] = \{d_0 - \frac{G_d}{2}, \cdots, d_0, \cdots, d_0 + \frac{G_d}{2}\}, \tag{6.22}$$

$$\mathcal{I}_{G_\nu}[\nu_0] = \{\nu_0 - \frac{G_\nu}{2}, \cdots, \nu_0, \cdots, \nu_0 + \frac{G_\nu}{2}\}. \tag{6.23}$$

With these 4 sets defined, the noise estimation is the average power within the training set excluding the guard set as

$$P_{in} = \frac{1}{M_d M_\nu} \sum_{\substack{d \in \mathcal{I}_{M_d} \\ m \notin \mathcal{I}_{G_d}}} \sum_{\substack{\nu \in \mathcal{I}_{M_\nu} \\ \nu \notin \mathcal{I}_{G_\nu}}} |R_{r,\tilde{z}}[d, \nu]|^2. \tag{6.24}$$

Finally, for the detection test, first it is needed to compare the peak of the matched filter output $< d_0, \nu_0 >= \arg\max_{d,\nu} |R_{x,y}[d, \nu]|$. with the threshold η as

$$O = \begin{cases} 1, & |R_{r,\tilde{z}}[\hat{d}^{(CA)}, \hat{\nu}^{(CA)}]|^2 > \eta \\ 0, & |R_{r,\tilde{z}}[\hat{d}^{(CA)}, \hat{\nu}^{(CA)}]|^2 \leq \eta \end{cases} \tag{6.25}$$

If detection succeeds $O = 1$, the switch configuration transitions from (1)-A to (1)-B; otherwise, the receiver continues in this step until a detection happens.

Coarse acquisition

Upon successful detection $O = 1$, the coarse estimates for delay and Doppler are extracted directly from the peak correlation value as used in the detection test $\hat{d}^{(CA)} = d_0$ and $\hat{\nu}^{(CA)} = \nu_0$.

Timing synchronization

The estimated coarse delay $\hat{d}^{(CA)}$ is used to compensate timing via $r[n'] = r[n - \hat{d}^{(CA)}]$. This delay has a resolution of a sample. Later, an EKF tracking loop is used to refine this coarse estimation by adjusting the phase φ of the signal.

Fine Doppler estimation

The fine Doppler frequency offset refinement is performed using the phase difference across successive DSSS sequences. The Doppler is assumed that does not change significantly for the duration of 2 subframes. Therefore, the phase change between these two subframes follows a linear model $\phi[n] = (2\pi\nu T_s)n + w$ with $w \sim \mathcal{N}(0, \sigma^2)$ and correspond to the phase rotation generated by the Doppler in L_c samples as

$$\hat{\nu}^{(FA)} = \frac{\angle\left(R_{r,\tilde{z}}[\hat{d}^{(CA)}, \hat{\nu}^{(CA)}] R^*_{r,\tilde{z}}[\hat{d}^{(CA)} + L_c, \hat{\nu}^{(CA)}]\right)}{2\pi L_c T_s}. \tag{6.26}$$

Doppler compensation

Combining coarse and fine Doppler estimates, the signal is compensated as:

$$r_{\text{comp}}[n'] = r[n'] e^{-j2\pi(\hat{\nu}^{(CA)} + \hat{\nu}^{(FA)})n' T_s}. \tag{6.27}$$

Extended Kalman filter

The previous steps does not remove all the impairments from the channel, therefore it includes an EKF to estimate the $\hat{\varphi}$ phase of the signal and the residual of the Doppler $\hat{\nu}^{(\text{FA})}$. The inclusion of an EKF rationale is because the performance is higher compared with other tracking loops such as phase-locked loop (PLL) [153].

The state of the system at instant p is defined by the phase φ_p of the signal and the Doppler ν_p, where the subindex p represent the DSSS index block of one subframe duration. The Doppler is assumed constant over the measurement period, as the change in Doppler for such small period can be assumed negligible [153]. This measurement period correspond to the length of a DSSS sequence $L_c \times T_s$. Therefore, the update model $\mathbf{x}_p = [\varphi_p, \nu_p]^{\mathrm{T}}$ is defined as

$$\mathbf{x}_{p+1} = \mathbf{D}\mathbf{x}_p + \mathbf{v}_p, \quad \mathbf{D} = \begin{bmatrix} 1 & 2\pi L_c T_s \\ 0 & 1 \end{bmatrix}, \quad \mathbf{v}_p \sim \mathcal{N}\big(\mathbf{0},\, \mathbf{Q}\big), \tag{6.28}$$

where the process–noise covariance is $\mathbf{Q} = \mathrm{diag}\big(\sigma_\varphi^2,\, \sigma_\nu^2\big)$, representing unavoidable perturbations on phase and frequency.

For every DSSS sequence called p, the base-band samples $r_{comp}[n']$ are correlated with a local replica of the PRN code $\tilde{z}[n]$. This correlation includes an a-priori estimation of the Doppler based on the previous estimation ($\nu_{p|p-1}$),

$$c_p = \sum_{n=0}^{L_c-1} r_{comp}[n' + p]\tilde{z}^*[n]e^{-j\,2\pi\nu_{p|p-1}\,nT_s}. \tag{6.29}$$

Then, the phase of c_p is a noisy observation of φ_p:

$$u_p = \mathrm{wrap}\big[\angle(c_p) - \pi\big] = g(\mathbf{x}) + v_p, \tag{6.30}$$

where $g(\mathbf{x}) = \varphi_p$, and $v_p \sim \mathcal{N}\big(0,\, \sigma_u^2\big)$ is the measurement noise.

The Jacobian required by the EKF is

$$\mathbf{G}_p = \frac{\partial g}{\partial \mathbf{x}}\Big|_{\mathbf{x}_{p|p-1}} = \begin{bmatrix} 1 & 0 \end{bmatrix}. \tag{6.31}$$

Step-by-Step EKF Algorithm The following are the steps used by the EKF to estimate the phase and Doppler of the signal.

1. State prediction

$$\hat{\mathbf{x}}_{p|p-1} = \mathbf{D}\hat{\mathbf{x}}_{p-1|p-1}, \tag{6.32}$$

$$\mathbf{P}_{p|p-1} = \mathbf{D}\mathbf{P}_{p-1|p-1}\mathbf{F}^{\mathsf{T}} + \mathbf{Q}. \tag{6.33}$$

2. Measurement innovation

$$\tilde{u}_p = \text{wrap}\big[u_p - \hat{\varphi}_{p|p-1}\big], \tag{6.34}$$

$$\mathbf{S}_p = \mathbf{G}_p \mathbf{P}_{p|p-1} \mathbf{G}_p^{\mathsf{T}} + \sigma_u^2. \tag{6.35}$$

3. Kalman gain update

$$\mathbf{K}_p = \mathbf{P}_{p|p-1} \mathbf{G}_p^{\mathsf{T}} \mathbf{S}_p^{-1}. \tag{6.36}$$

4. State estimation update

$$\hat{\mathbf{x}}_{p|p} = \hat{\mathbf{x}}_{p|p-1} + \mathbf{K}_p\, \tilde{u}_p, \tag{6.37}$$

$$\mathbf{P}_{p|p} = \big(\mathbf{I} - \mathbf{K}_p \mathbf{G}_p\big) \mathbf{P}_{p|p-1}. \tag{6.38}$$

Once the EKF has finished its update estimation, its output is the new state of the system, $\hat{\mathbf{x}}_{p|p}$, with the new value of the phase and Doppler. These values of phase and Doppler are considered constant for the duration of the DSSS, and they are used to compensate the received signal as

$$\hat{s}_k[n] = r_{\text{comp}}[n'] e^{-j(2\pi \hat{\nu}^{(FA)} n T_s + \hat{\varphi})}, \tag{6.39}$$

where $\hat{s}_k[n]$ is the input to the communications block.

6.2.2 5G communications receiver

For this hybrid receiver, the communication part follows an approach similar to the architecture used in 5G. Fig. 6.4 shows the block of the receiver dedicated to the communication part, that has as input the signal compensated from the navigation part.

OFDM demodulation

In the OFDM demodulation, the receiver remove the CP as $\hat{z}_k[n] = \hat{z}_k[n + s(N_{\text{FFT}} + N_{\text{CP}}) + N_{\text{CP}}]$, where N_{FFT} are the fast Fourier transform (FFT) points and N_{CP} is the CP length.

Then, the OFDM demodulation as the FFT of $\hat{Z}_k[l] = \text{FFT}\{\hat{z}_k[n]\}$, and extract the bits transmitted.

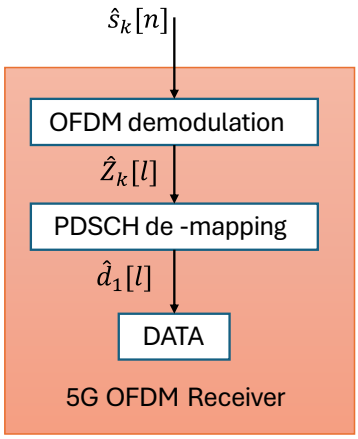

Fig. 6.4: 5G OFDM receiver architecture.

PDSCH de-mapping

Finally, the PDSCH de-mapping extract the bits from the REs within the RG dedicated to the PDSCH.

$$\mathbf{Z}_{\text{PDSCH}} = \{\hat{Z}[l,k] | (l,k) \in \mathcal{R}_{\text{subcarrier}} \times \mathcal{T}_{\text{symbol}}\} \tag{6.40}$$

where $\mathcal{R}_{\text{subcarrier}}, \mathcal{T}_{\text{symbol}}$ are the indices for the subcarriers and symbols within the RG dedicated to the PDSCH.

Once extracted the PDSCH elements, the receiver demodulate the symbols and generate the bitstream. This work does not include any channel coding as it is outside the scope of the work, therefore the final KPI for the communication block is the uncoded BER.

6.3 Performance evaluation

The following metrics are used to evaluate the performance of the proposed JCAP receiver:

1. The EVM: This metric quantifies the degradation of the OFDM signal caused by the aggregation of the DSSS for different values of SIR between the OFDM and DSSS signal. It is used the SIR between the DSSS (as signal of interest) and the OFDM (as interference for the navigation service). This metric provides insight into the effect of the aggregation of the DSSS waveform in the OFDM, prior to the channel and receiver effects.

2. The receiver operating curve (ROC) curve for the receiver. It is compared the

probability of false alarm P_{fa} detection with the probability of detection P_{d} for discrete values of SIR. Also, it is shown the probability of detection P_D of the DSSS signal for continuous values of DSSS SIR.

3. The accuracy of the observables estimators in the different steps in the receiver.

4. Finally, the uncoded BER of the system is evaluated for different values of OFDM SIR. The best scenario is included as benchmark, the uncoded BER when there is no DSSS and only AWGN as channel.

Table 6.1 summarizes the simulation parameters and their corresponding values used along with a reference where it was used, they are based on typical values found in the literature for GNSS and 5G communication systems.

6.3.1 OFDM degradation after including the DSSS

The first metric used is the EVM for different values of $\text{SIR}_{\text{DSSS}}[\text{dB}]$ of the JCAP waveform. The EVM is defined as

$$\text{EVM}_{\text{RMS}} = \sqrt{\frac{\sum_n |s[n] - z_k[n]|^2}{\sum_n |z_k[n]|^2}}, \tag{6.41}$$

where $z_k[n]$ is the signal without DSSS and $s[n]$ is the signal that includes the DSSS.

This metric is evaluated in Fig. 6.5 and provides insights on how the receiver performs ideally (without channel effects) when including the DSSS. Fig. 6.5 includes also the EVM reference to achieve a BER of 10^{-6}, these thresholds are defined by 3GPP for 5G systems, serving as a benchmark for acceptable signal quality.

Fig. 6.5 shows that a value of SIR for the limits to reach the maximum level of EVM for QPSK up to 256QAM. Different values of RB are used to evaluate the EVM, the minimum allowable number of RB as 1, the RB needed for the SSB as 20 and the maximum number of RB allowed for FR1 as 273.

The dependency of these limits with the number of RB of the waveform can be seen in Fig. 6.5. By increasing the 5G RB it reduces the maximum power allowed for the DSSS to stay below the EVM threshold for different modulations defined by 3GPP.

This reduction is because of the length of the DSSS increases ($L_c = f_s \times 1\,\text{ms}$), for larger RB more samples per subframe are needed and the energy per sample is spread over a large set. These limits are important for the next results related to the navigation and communication performance.

Table 6.1: Simulations parameters

Parameter	**Symbol**	**Value**
Antenna elements x axis	N_x	16
Antenna elements y axis	N_y	16
Number of beams	K	7
Beam directions	(θ_k, ϕ_k)	$\theta_k = 0.1334$, $\phi = \{0, \pi/3, 2\pi/3, \pi, 4\pi/3, 5\pi/3\}$
Satellites in LOS	Q	1
Channel gain phase	φ	$\mathcal{U}(0, 2\pi)$
Channel gain magnitude	$\lvert\alpha_{q,k}\rvert$	1
Carrier frequency	f_c	2.2 GHz
5G frames simulated	N_f	100
SIR range dB	$\rho_0, \cdots, \rho_z$	$[-40, \cdots, -5]$
DSSS sequence length	L_c	$1\,\text{ms} \times f_s$
OFDM subcarrier spacing		15 kHz
OFDM Resource Blocks	N_{RB}	$[1, 20, 273]$
Doppler bins	N_ν	61
Max Doppler	$\nu_{D_{\text{MAX}}}$	± 15 kHz
Detector training delay	M_d	20
Detector training Doppler	M_ν	20
Detector guard band delay	G_d	2
Detector guard band Doppler	G_ν	2
Probability of false alarm	P_{fa}	$[10^{-10}, \cdots, 10^0]$
Process phase update noise	σ^2_φ	10^{-2}
Process Doppler update noise	σ^2_ν	$10^{-3}\,\text{Hz}^2$
Measurement phase noise	σ^2_u	$6^{-2}\,\text{rad}^2$

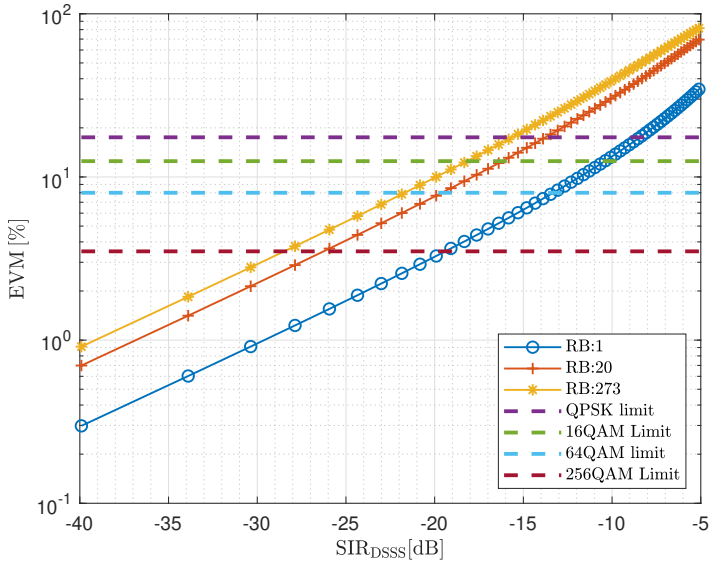

Fig. 6.5: EVM for different 5G signals. From the minimum RB of 1, the number of RB for the SSB as 20 and the maximum RB in FR1 as 273. It includes the EVM limits for different modulations as required by 3GPP.

6.3.2 Receiver operating curve

The ROC curves in Fig. 6.6 are plots of the probability of detection (Pd) versus the probability of false alarm (Pfa) for a given DSSS SIR [154]. This Fig. 6.6 shows how the detector perform in different configurations, useful for the designer when evaluating the LBA and the expected P_{fa}.

The Fig. 6.7 shows what are the SINR limits to properly detect the DSSS when it has interference from the OFDM signal and AWGN noise for a given P_{fa}. The effect of the 5G RG size is compared in Fig. 6.7 by evaluating the probability of detection. The values used for the RG are the minimum value possible and the same RG used for the SSB.

From Fig. 6.7 it is clear that the RBs affect the SINR level to reach 100% detection. Therefore, a system designer could set a limit in the SINR to detect the DSSS signal within the LBA. Besides, linking this result with the previous result, a SIR for the DSSS around $-20\,\mathrm{dB}$ will be always detected and the EVM small enough to reach up to 64QAM modulation.

It should be mentioned that the acquisition/detection steps are based on a single DSSS. Here, it is evaluated the worst case of a single DSSS, while a coherent integration of more DSSS will increase its energy and the detection SINR threshold can go lower. In the following evaluations is assumed the minimum SIR for the DSSS that is enough for being always detectable. Therefore, from Fig. 6.7 the minimum to $-20\,\mathrm{dB}$ is set.

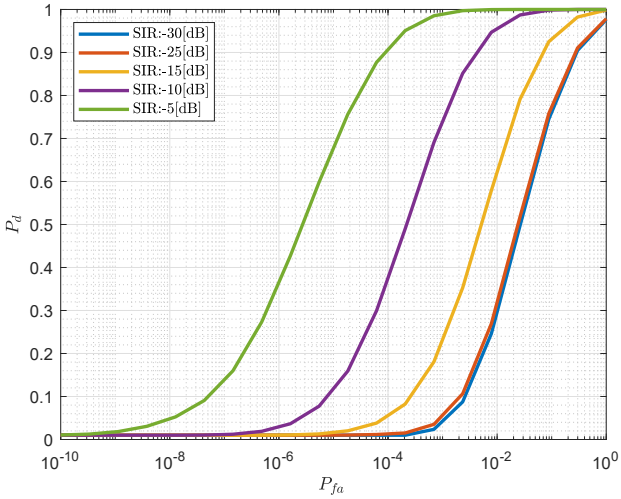

Fig. 6.6: Receiver operating curve for different values of DSSS SIR for a signal with RB=1.

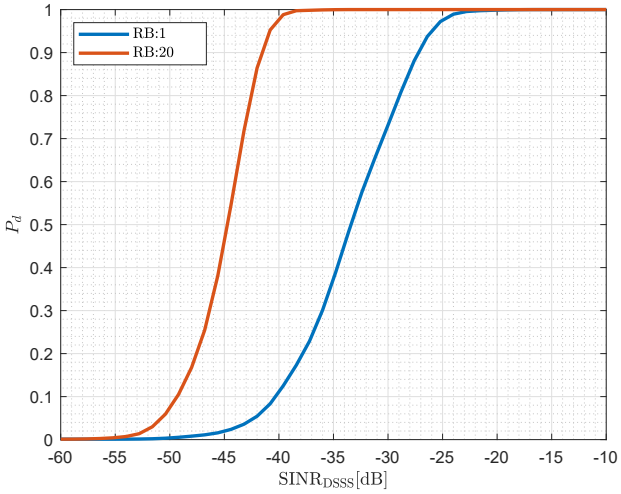

Fig. 6.7: Comparison of the RB to detect the DSSS for different values of interference from OFDM and receiver noise.

6.3.3 Observable estimation

Once the signal is detected, the evaluation of the accuracy of the observable estimation continue by evaluating the variance of the estimator. Each estimator used in Fig. 6.2 is evaluated separately in the following subsections.

Coarse delay estimation

It starts by evaluating the variance of the delay estimation defined in (6.2.1). This estimator has a resolution of one sample or $[-T_s/2, +T_s/2]$, therefore, the error can be modeled as a uniform random variable within these limits $\chi_{d^{(CA)}} \sim \mathcal{U}(-T_s/2, T_s/2)$. Therefore, the variance of this estimator can be obtained analytically as $\sigma^2(\hat{d}^{(CA)}) = 1/(12 f_s^2)$.

Coarse Doppler estimation

From the coarse acquisition the accuracy on the Doppler estimation is directly related with the number of bins used and the maximum range of expected Doppler. There is a trade-off between processing time and accuracy, as a larger number of bins increase the resolution but at the same time the processing time. The simulation uses a similar value used in GNSS application to reach 500 Hz of resolution per beam [7] give the maximum Doppler expected.

Fine Doppler estimation

Then, for the fine Doppler estimation, the phase change of two consecutive DSSS is due to the Doppler shift, modeled as $\Delta\varphi = 2\pi\nu L_c T_s + \epsilon$, where $\epsilon \sim \mathcal{N}(0, \sigma_\epsilon^2)$ represent the phase noise due to the interference and receiver noise. This work does not include the phase noise of the oscillators at the transmitter and receiver as the only impairment of interest is the external interference and the receiver noise. Therefore, it is assumed a $\sigma_\epsilon = 0.1$ rad as a typical value found in the literature [155, 156]. The estimator in (6.26) achieve an accuracy on the fine Doppler estimation as $\sigma_{\hat{\nu}^{(FA)}} = \sigma_\epsilon/(2\pi L_c T_s) = 15.92$ Hz.

Extended Kalman filter

Up to now the performance of the previous estimators was done analytically as a block processing. However, to further improve the estimation, the receiver includes an EKF. To evaluate its performance a simulation of the receiver from Fig. 6.2 is used. This simulation evaluates the following parameters for the EKF block: the time to reach an error in the

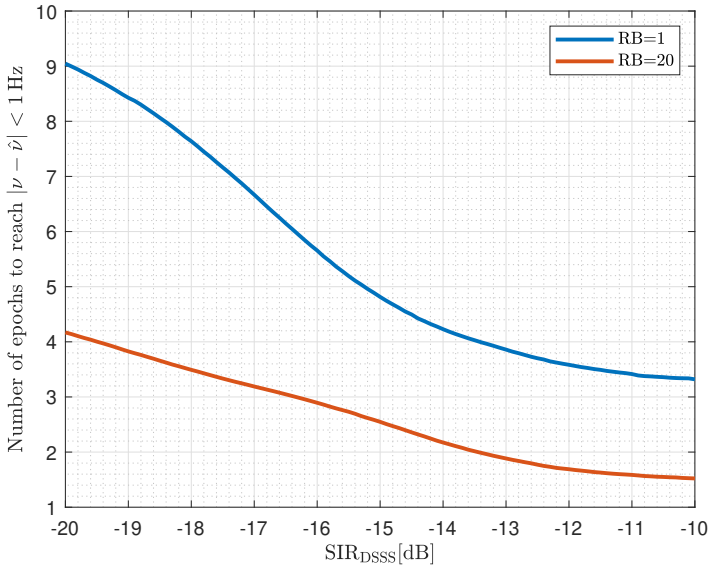

Fig. 6.8: Number of epochs to reach an error in the Doppler estimation below 1 Hz for different values of SINR of the DSSS.

estimation below a certain threshold, and once it reaches a steady state, the accuracy achieved as the absolute error between the Doppler estimation and the real value of the Doppler.

The first parameter to evaluate is the time, in epochs or DSSS sequences, that the EKF takes to reach an error in the estimation below 1 Hz. Depending on the value of SIR, the algorithm will require more or less time to reach the threshold. Fig. 6.8 shows the number of epochs required to reach and maintain the 1 Hz threshold for different values of SIR of the DSSS.

Now, it is presented some examples of the convergency of the EKF to reach as close as possible 0 Hz of error. In Fig. 6.9 and 6.10 the EKF algorithm reach an error very close to 0 Hz.

Finally, in Fig. 6.11 is evaluated the accuracy of the steady state of the tracking loop, after the initial epochs where there are some bouncing on the estimation, as seen in Fig. 6.9 or Fig. 6.10. This steady state is defined as the last epoch the error in the Doppler estimation passes the 1 Hz threshold, and it is computed as the mean value of this error within the steady state. This evaluation is done for several values of SIR.

This time, the error in the estimation is greatly reduced for SIR levels compared to the detection in Fig. 6.7. This allows to reach errors below 0.1 Hz on the estimation.

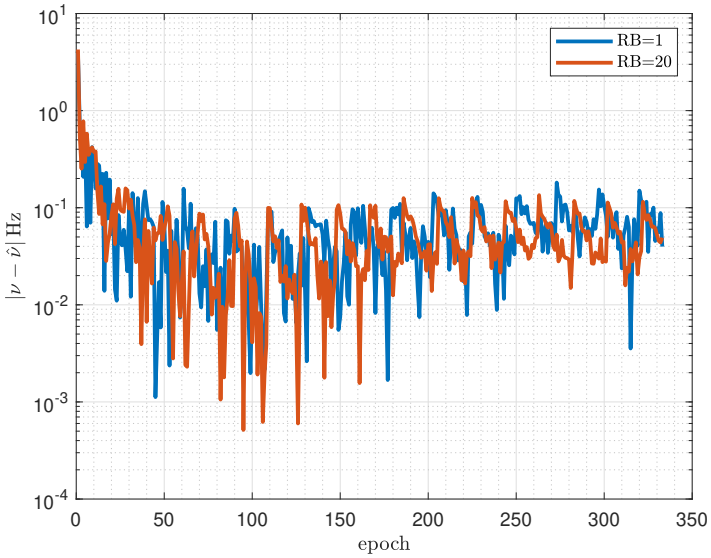

Fig. 6.9: DSSS Doppler tracking using EKF. With a SIR of -10 dB.

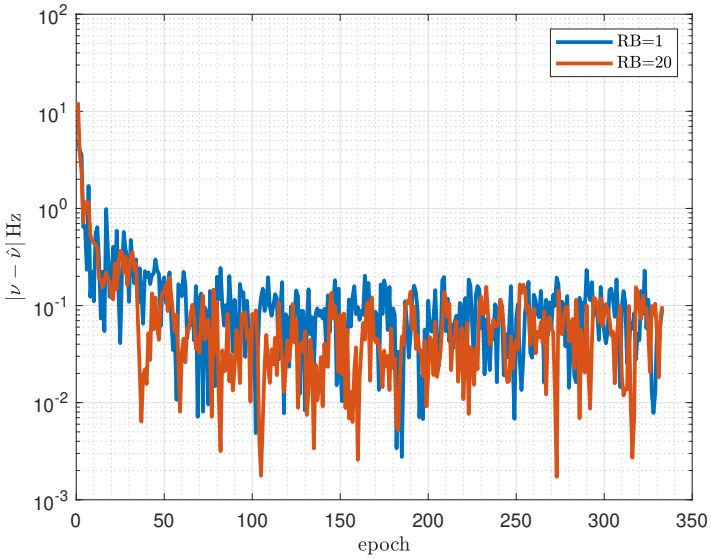

Fig. 6.10: DSSS Doppler tracking using EKF. With a SIR of -20 dB.

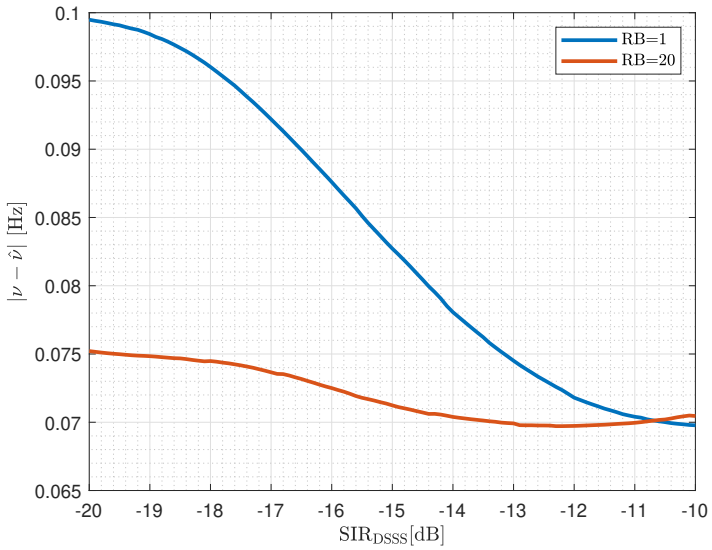

Fig. 6.11: Absolute error for Doppler estimation from EKF using the DSSS as reference for different values of SIR.

6.3.4 Communication receiver assisted by DSSS

The final evaluation of the system is the uncoded BER. Fig. 6.12 shows the uncoded BER for different values of DSSS SIR. It includes as a benchmark the case where there is no DSSS and the channel is just AWGN. This benchmark represent the best scenario possible. Therefore, one can see that reducing the SIR, the BER improves as it removes energy from the DSSS interference. However, this DSSS SIR is bounded by the detection and tracking limits shown in the previous results. If the DSSS cannot be detected, and the delay and Doppler cannot be properly estimated, the signal cannot be compensated for these impairments and the demodulation is not possible. There is no plot with lower SIR of 16 dB as the navigation system perform poorly and no demodulation is possible.

Something to take into account in this result is that there is no channel estimation within the OFDM grid, in the sense that there is no pilots embedded. The main rationale for this is to reduce the overhead at the communication block and reuse the estimation done at the navigation block hybridization both receivers blocks.

6.4 Summary

This chapter introduces a detailed receiver architecture explicitly tailored for the hybrid OFDM-DSSS waveform proposed in Chapter 5, designed to provide integrated JCAP services.

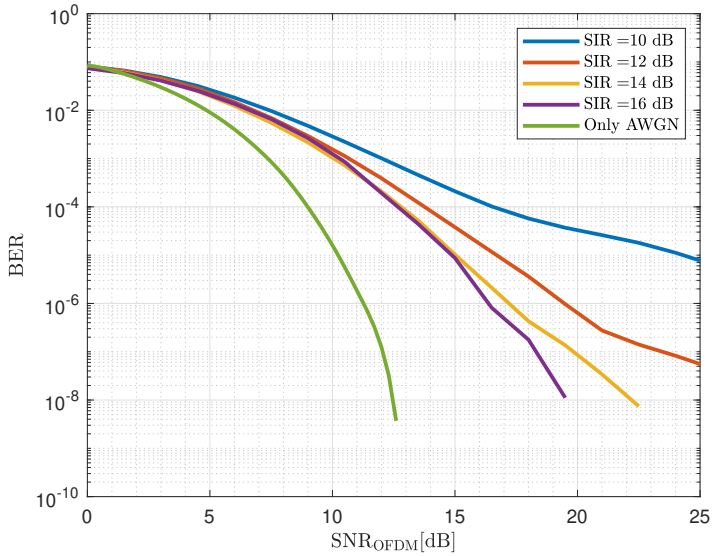

Fig. 6.12: Uncoded BER for the PDSCH in 5G for different values of SIR between the 5G OFDM signal and the DSSS pilots. The uncoded BER "Only AWGN" is the benchmark where no DSSS is included, and the channel is only AWGN.

The receiver integrates navigation and communication processing chains, utilizing the DSSS component to robustly estimate key channel parameters such as delay, Doppler, and phase. These estimations are subsequently employed to enhance OFDM data demodulation performance, demonstrating a significant improvement in communication reliability. Extensive simulations evaluated metrics such as EVM, ROC, and BER, revealing that a DSSS-to-OFDM SIR of approximately -20 dB offers an optimal balance—providing high positioning accuracy while minimally impacting communication quality.

The results confirmed that the hybrid JCAP receiver can successfully manage interference between the DSSS and OFDM signals, effectively improving the accuracy of navigation parameter estimation even in low SINR environments. Furthermore, the communication receiver's BER was enhanced by leveraging the precise channel estimates obtained from the DSSS signal, thereby validating the practical advantages of a unified JCAP receiver structure. The analysis underscored the feasibility of adopting this hybrid waveform as a robust and efficient solution for simultaneous communication and navigation, compatible with legacy 5G infrastructure.

Connecting these findings to the overall conclusions of the thesis, the hybrid receiver architecture presented in this chapter serves as a foundational step towards seamless GNSS-independent positioning within 5G NTN deployments. The receiver structure aligns with practical implementation constraints, leveraging existing OFDM-based systems while

introducing DSSS signals transparently for navigation and synchronization purposes. Future directions identified include validation through hardware-in-the-loop and over-the-air testing, further optimization of hybrid waveform parameters, exploration of uplink positioning capabilities, and standardization efforts towards next-generation JCAP systems. These pathways present promising research avenues, facilitating the transition towards fully integrated and resilient navigation solutions in future wireless networks.

Chapter 7

Discussion and perspectives

This dissertation has proposed a empirical interference model was obtained to handle the severe delay and Doppler dynamics of LEO satellites, for which closed-form analysis is intractable. Furthermore, it has analyzed, and validated a JCAP framework that can be used with the 5G NTN downlink transparently. Its central contribution is an overlay DSSS component that remains quasi-transparent to 5G NTN receivers while providing centimetre-to-metre-level positioning without requiring an external GNSS module at the UE.

7.1 Principal findings

- **Interference-aware design**: Modeling the interference maxima of the 5G PRS with a GEV distribution that enables link-budget dimensioning without exhaustive physical-layer simulations.
- **Seamless JCAP operation**: Proposing a transparent hybrid waveform based on OFDM and DSSS for JCAP services. System-level simulations show that the proposed waveform achieves a 2D root mean square error (RMSE) positioning error below 1 m while preserving 5G spectral efficiency.
- **Standardisation outlook**: Because the DSSS layer is independent to the 5G NTN downlink waveform, it can be specified as an *out-of-band* feature, maintaining backward compatibility with 5G NTN Rel-17/18 UEs. This aligns with the Rel-19 3GPP work item on GNSS-independent approach.

The contributions of this thesis represent an initial step toward that GNSS-independent operation.

7.2 Planned extensions of the present work

1. **Other positioning techniques**: This thesis work has been focused in the downlink signal for positioning. However, other approach is the use of the uplink signals [157]. The evaluation of single satellite multi-epoch uplink positioning in 5G is a research gap to be covered.

2. **Implementation of PVT in a LEO scenario as distributed LMF**: The actual architecture for positioning in 5G resides in the use of the LMF as a PVT engine for the location estimation. The novel concept of edge computing and its use in NTN arises the question on how to design a distributed LMF located in the edge of the network (the satellites). This distributed LMF could reduce the TTFF and latency of the position estimation.

3. **Evaluation of system performance with different integration times of the DSSS**: Evaluate the performance and requirements of having a DSSS of at least 20 ms. This way it is possible to remove the ambiguity for the estimation of the time of arrival (ToA) as the duration of the code is larger than the maximum delay at 0 degrees of elevation angle (for a LEO satellite at 600 km altitude). The complexity to acquire such large code, and the tradeoffs of using large codes needs to be evaluated in this future work.

4. **Experimental evaluation by hardware-in-the-loop validation and over-the-air testing**: Port the MATLAB simulation chain from the third contribution to a real-time, Ka-band, software defined radio (SDR) based testbed to assess waveform robustness under realistic phase noise and analog to digital converter (ADC) quantization. Validate the simulations and hardware-in-the-loop (HIL) by using a real satellite and receive the hybrid DSSS and 5G NTN waveform and compare with the simulations of this work. This is under evaluation with the O3b constellation from SES [158].

5. **Security improvement as signal authentication by using the DSSS as a watermark**: Another important direction for future research is the interpretation of DSSS as a digital signature for OFDM signals, as similar to [159]. In this framework, only users possessing the pseudorandom sequence can authenticate the transmitted data. Thus, in the presence of a man-in-the-middle attack, a receiver can verify the integrity of the data, as an attacker without knowledge of the sequence would be unable to generate valid transmissions.

7.3 A vision for next joint communication and positioning services

The evolution from 5G to 6G is expected to deliver native JCAP capabilities, unifying data, positioning, and even environment sensing within a single air interface [160, 161] highlighted by the Hexa-X and IMT-2030 roadmaps [162], including:

1. **Beam management and constellation design**: It was assumed in this thesis that the UE can receive at least four satellites to extract the observables to estimate its position. However, how about the data service? Can the UE decode the signal of a satellite while it is illuminated (interfered) by more than one satellite? To answer this question it is needed to design a constellation and a beam management in order to offer both services from multiple satellites.

2. **Standardization contribution**: Promote the proposed overlay DSSS pilot within 3GPP ensuring compliance with international mobile telecommunications (IMT)-2030 centimeter-accuracy requirements.

3. **Multi-layer system**: As a future work, it is envisioned the use of multiple layers of connectivity, from terrestrial, UAVs, HAPSs, satellites in different orbits. It is expected the use of this multiple connectivity to enhance communications and positioning in a collaborative way between all entities.

4. **Further than Earth**: The actual Moon missions from NASA Artemis [163] and ESA Moonlight [164] are expected to bring back the humanity to the Moon, requiring novel communications and PNT services. The extrapolation of this work and its extensions to the Moon (or other celestial bodies) is a challenge itself that need to be address in collaboration with the space agencies.

7.4 Concluding remarks

This dissertation presents an empirical interference-power model for NTN scenarios that use the PRS as a navigation waveform. As analytic formulations are impractical, the model is derived via Monte-Carlo simulations.

Overall, the results advance the understanding of interference in LEO scenarios and evaluate the feasibility of a 5G NTN system that operates independently of GNSS. The

results also underscore the importance of advanced multiplexing strategies to manage multiple satellite signals, thereby mitigating SINR degradation.

Furthermore, the proposed joint waveform relaxes the requirement on external GNSS and enables navigation services in NTN deployments. Simulations confirm that the joint waveform provides both data and navigation services within the typical use case scenarios.

Integration of JCAP services in a single receiver yields mutual benefits: the navigation signal assists data demodulation, while high-rate communications facilitate rapid delivery of navigation and correction messages.

From a standardization viewpoint, the overlay DSSS signal is not intended to replace the 5G NTN waveform but to operate transparently on top of it. Consequently, the signalling may be specified outside the 3GPP standard and still coexist with compliant receivers, supporting dedicated navigation.

In summary, combining DSSS with OFDM unifies joint communication and positioning capabilities with enhanced service trustworthiness, paving the way for resilient, GNSS-independent NTN deployments.

Appendix A

Extreme value theory

A.1 Preliminaries and notation

- Let $\{X_i\}_{i\geq 1}$ be an *i.i.d.* sequence representing the instantaneous interference power (e.g. post-filter squared magnitude) observed at symbol rate or at the in-phase/quadrature (I/Q) sample rate.
- Denote the cumulative distribution function (CDF) of X_i by $F(x) = \Pr\{X_i \leq x\}$; we assume F is non-degenerate.
- For a positive integer n,

$$M_n \triangleq \max\{X_1, \ldots, X_n\} \tag{A.1}$$

  is the *n–sample maximum*. In a communication setting n could be the number of samples within one symbol or within an entire frame, depending on the designer's definition of an *interference event*.

A.2 The Fisher-Tippett-Gnedenko theorem

There exist sequences of constants $a_n > 0$ and $b_n \in \mathbb{R}$ such that

$$\Pr\Big\{\frac{M_n - b_n}{a_n} \leq x\Big\} \;=\; F^n(a_n x + b_n) \;\xrightarrow[n\to\infty]{}\; G(x) \tag{A.2}$$

for some non-degenerate limit CDF G *if* F belongs to the *max-domain of attraction* of one of the three standard extreme value laws

$$\text{Gumbel (Type I): } G_0(x) = \exp\big(-e^{-x}\big), \quad x \in \mathbb{R}, \tag{A.3}$$

$$\text{Fréchet (Type II): } G_\xi(x) = \exp\big(-(1+\xi x)^{-1/\xi}\big), \quad x > -1/\xi,\ \xi > 0, \tag{A.4}$$

$$\text{Weibull (Type III): } G_\xi(x) = \exp\big(-(1+\xi x)^{-1/\xi}\big), \quad x < -1/\xi,\ \xi < 0. \tag{A.5}$$

Unified Representation Eqs. (A.3)–(A.5) can be written compactly as the *generalized extreme value* family

$$G_\xi(x) = \exp\Big\{-\big[1+\xi x\big]^{-1/\xi}\Big\}, \quad 1+\xi x > 0, \tag{A.6}$$

where the shape parameter ξ determines the tail regime:

$$\xi = 0 \ \Rightarrow\ \text{Gumbel}, \quad \xi > 0 \ \Rightarrow\ \text{Fréchet}, \quad \xi < 0 \ \Rightarrow\ \text{Weibull}.$$

A.3 Block-Maxima model for RF interference

A.3.1 Block definition

Assume the physical layer delivers L complex samples per symbol. Define the jth data block as

$$\mathcal{B}_j = \big\{X_{(j-1)n+1}, \ldots, X_{jn}\big\}, \quad n = L \text{ (symbol) or } n = LN_f \text{ (frame)}.$$

The block maximum is

$$Y_j = \max_{X \in \mathcal{B}_j} X, \qquad j = 1, \ldots, N \tag{A.7}$$

where $N = \lfloor T_{\text{obs}}/n \rfloor$ and T_{obs} is the total sample horizon.

A.3.2 Justification via FTG theorem

If the *parent* CDF F satisfies the FTG regularity conditions (e.g. $1-F(x)$ is regularly varying for impulsive interference or decays exponentially for thermal noise), then the normalized maxima

$$Z_j = \frac{Y_j - b_n}{a_n}$$

are (asymptotically) i.i.d. with distribution G_ξ given by (A.6). Hence, the *GEV* distribution is the theoretically justified choice for fitting $\{Y_j\}$.

A.4 Fitness tests

To evaluate the goodness-of-fit of a dataset to a known distribution, a statistical hypothesis test is structured as follows:

- **Null Hypothesis (H_0)**: The dataset is drawn from a GEV distribution with parameters μ, σ, and ξ.
- **Alternative Hypothesis (H_1)**: The dataset does not follow a GEV distribution with the given parameters.

The procedure typically involves the following steps:

1. **Parameter Estimation**: Estimate the parameters $(\hat{\mu}, \hat{\sigma}, \hat{\xi})$ using methods such as Maximum Likelihood Estimation (MLE), Probability Weighted Moments (PWM), or the Method of Moments.
2. **Goodness-of-Fit Test Statistic**: Compute a test statistic such as the Kolmogorov-Smirnov (K-S), Anderson-Darling (A-D), or the Chi-square statistic to quantify the difference between the empirical and the theoretical GEV distribution.
3. **Calculation of the p-value**: The p-value is computed by comparing the observed statistic with its distribution under the null hypothesis:

$$p = P(T \geq t_{obs}|H_0) \tag{A.8}$$

where T is the test statistic, and t_{obs} is its observed value from the sample data.

Usually, the p-value is determined numerically by Monte Carlo simulation or approximation methods due to the complexity of the distribution.

A.4.1 Kolmogorov-Smirnov / Anderson-Darling

Kolmogorov–Smirnov / Anderson–Darling goodness-of-fit tests adjusted for parameter estimation. The KS statistic quantifies the maximal deviation between an empirical and a reference CDF, offering a non-parametric, distribution-free goodness-of-fit test under the ideal conditions of i.i.d. continuous samples and no parameter estimation. In extreme value applications (e.g. validating a fitted GEV to interference block-maxima) the test remains attractive for its simplicity.

A.4.2 p-value

For the p-value a significance level (α) is chosen (commonly $\alpha = 0.05$). The decision rule is:

- If $p \leq \alpha$, reject H_0: conclude the data do not follow the GEV distribution.
- If $p > \alpha$, do not reject H_0: conclude there is insufficient evidence to reject the hypothesis that the data follow the GEV distribution.

The p-value provides a measure of compatibility between the data and the assumed GEV model. A large p-value suggests the data are compatible with the GEV model, whereas a small p-value suggests incompatibility.

A.5 Interpretation for RF interference

- *Fréchet ($\xi > 0$)* arises for heavy-tailed, impulsive interference such as co-channel bursts or man-made impulsive noise, implying unbounded extremes and infinite moments above order $1/\xi$.
- *Gumbel ($\xi = 0$)* typically models thermal-noise-dominated scenarios, consistent with exponentially decaying tails yielded by a log-normal or Gaussian parent.
- *Weibull ($\xi < 0$)* fits situations where physical or regulatory limits cap the interference power (e.g. adjacent-channel leakage masks).

Appendix B

Dataset generation

This annex shows how the dataset used in Chapter 4 has been created. It is public access [165]. We start describing the details of the satellite scenario, the parameters that are involved from a user on ground point of view, and their effect in the received signal via the channel model.

B.1 Scenario

Fig. 4.1 shows the FOV of a satellite. Here, the furthest boundary represents the complete view of Earth from a satellite when a user is positioned at an elevation angle of 0°. At the center of this illustration lies the SSP, which is the Nadir projection of the satellite on the Earth's surface. The dashed circle in the figure delimits the coverage area when users operate with a certain elevation angle mask θ_{MASK}. The value of θ_{MASK} is crucial as it significantly impacts the maximum signal propagation time between the satellite and the ground station, as well as the maximal losses incurred due to FSPL.

Fig. 4.2 represent the vertical cut of the satellite-Earth scenario that shows also the LH of the user at ground. The parameters involved are: θ_{MASK} the elevation angle mask, ρ_{MAX} is the maximum distance from the user to the satellite; r_E is the Earth radius; h_{SAT} is the satellite altitude over the Earth surface; φ is the angle from the satellite to the user on the ground and Θ is the angular distance between the SSP and the position of the user.

Fig. 4.3 presents a three-dimensional portrayal of a single satellite pass, which is an expansion of the LH concept from Fig. 4.2. This depiction emphasizes that the LH is contingent upon the geographical coordinates of the user, defined by latitude ϕ and longitude λ. Furthermore, the LH is influenced by the user's altitude above mean sea level, denoted as

h, and the time of observation t. This implies that a moving user's LH will change over time. Moreover, Fig. 4.3 highlights various parameters that play a critical role in understanding satellite dynamics from the perspective of a ground user, which are integral to the channel model. Among these parameters, θ_{MAX} stands out as particularly significant. It represents the maximum elevation angle that the satellite will attain during a specific pass over the user. This parameter is vital because it influences several other factors, such as the duration of the satellite pass and the minimum distance between the satellite and the user, represented by ρ_{min}. The range of θ_{MAX} is defined as being between $[\theta_{\text{MASK}}, \pi/2]$. It should be noted that each satellite pass will have a unique value of θ_{MAX}, which is determined by orbital dynamics, the specific location of the user, and time.

Equation (4.1) obtains the maximum distance between the satellite and the user based on the values of $\theta_{\text{MASK}}, h_{\text{SAT}}, r_E$. Fig. 4.2 serves as a perpendicular cross section of the plane illustrated in Fig. 4.1, aiding in understanding the trigonometric calculations that lead to Equation (4.1). This figure helps understand the direct relationship between θ_{MASK} and ρ_{MAX}, in relation to the altitude of a satellite h_{SAT} plus the radius of the Earth r_{E}.

B.2 Dataset generation

For the analysis of the PNT accuracy from LEO satellites we follow a MonteCarlo approach, evaluating the system in several satellite passes. We also uses the Starlink constellation as a reference, as it has thousands of satellites and in a short period of time, a user on ground could see several satellites at the same time. Furthermore, instead of simulating the whole Starlink constellation for each MonteCarlo iteration, we split the MonteCarlo analysis in four steps:

1. Spread the UE on the Earth's surface evenly
2. Simulate the Starlink passes over each user computing the satellite position $\vec{r}_i(t) = [x_i(t); y_i(t); z_i(t)]$, the velocity of each satellite $\vec{v}_i(t) = \frac{d}{dt}\vec{r}_i(t)$
3. Generate a dataset based on the channel model parameters from the simulated satellite passes $[L_i(t), \tau_i(t), \upsilon_i(t)]$.
4. For the MonteCarlo analysis, at each iteration, from the dataset, select randomly a user UE, then, select a random time t_i to evaluate the channel and obtain the values $[L_i(t_i), \tau_i(t_i), \upsilon_i(t_i)]$ for each visible satellite at this time.

Table B.1: Structure of the starlink dataset

Parameter	Data type	Content
Ground Station	Structure	Geodetic [Lat,Lon,h] and ECEF coordinates [X,Y,Z]
Passes	Array of Satellite	Satellite [1,..N]
Satellite	Structure	Pass time $[startpass, duration]$, AER coordinates $[Az, El, d]$, ECEF coordinates $[X, Y, Z]$ and relative speed with the ground station $[rel_v]$

The dataset structure is designed with the fields from Table B.1:

Fig. 4.5 shows the user ground spread. It is based on a spherical Fibonacci lattice, expressed as a sequence of points $\langle x, y\rangle$ in the unit square $[0, 1]^2$. Each point is converted to spherical coordinates (longitude λ and latitude ϕ in radians) by the inverse cylindrical equal area projection: $\langle \lambda, \phi\rangle = \langle 2\pi x, \text{acos}(2y - 1) - 2\pi\rangle$

For each UE position, using SGP-4 as a orbit propagator and with the public Starlink TLE as input, we compute the values of several satellite passes. Using ECEF as a common coordinate reference for position and velocity vectors. Fig. B.1 shows an example of the values for Doppler and delay at a single position.

B.3 Channel model

Fig. B.2 shows that the channel can be represented in different domains. These representations are: the channel impulse response (CIR) $h(t, \tau)$, the Transfer Function $H(t, f)$, the Doppler spread function $\Gamma(\upsilon, f)$ and the delay/Doppler spread $\gamma(\upsilon, \tau)$. In order to change from one representation to other, a Fourier transform $\mathcal{F}$ or an Inverse Fourier transform $\mathcal{F}^{-1}$ should be applied to the desired domain.

The behavior of the channel is the same for all representations. However, depending on the application, it is more convenient to represent the channel in one domain or another. We use a delay/Doppler spread representation in (4.5), as this more closely resembles the physical wireless channel [103].

The channel representation in (4.5) depends on the free space path looses L_i, a random phase shift h_i, a certain Doppler υ_i and a certain delay τ_i. We assume that the channel is WSS for the duration of the slot (10 ms), thus, the mean values of L_i, τ_i and υ_i can be considered constant for the duration of the slot. This is a realistic assumption that does not compromise the results, as similar NTN models use it [123]. In addition to channel parameters, we assume

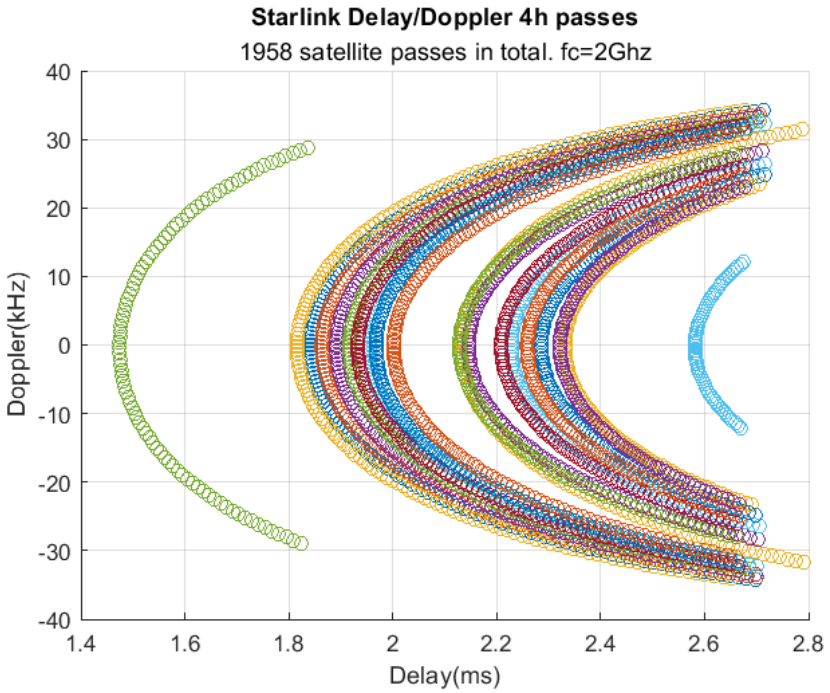

Fig. B.1: Starlink Delay/Doppler values for a 4-hours passes

that the distance between user-satellite i, ρ_i and the relative speed between the user and the satellite i $\mathrm{v_{i\ SAT}}$ are constants for the duration of the slot.

The channel parameters L_i, τ_i and υ_i are directly related by ρ_i as $L_i = \frac{c}{4\pi f_c \rho_i}$, $\tau_i = \frac{\rho_i}{c}$ and υ_i depend on the derivative (speed) of ρ_i.

The channel FSPL are modeled by L_i assuming a unit gain on the TX and RX antennas and depends on the carrier frequency f_c and ρ_i. A more realistic NTN channel has other losses, such as tropospheric effects (gas absorption, rain/cloud attenuation), antenna beam misalignment, etc. These effects are assumed negligible as these attenuations compared to FSPL are much lower for transmissions in L/S frequency bands standardized for NTN.

The signal delay τ_i is also considered constant as its variation for a slot is negligible considering only the distance between the satellite and the receiver. A more accurate model would include an excess of ionospheric and tropospheric delay due to signal refraction. These effects have been extensively studied for GNSS receivers and is modeled by Klobuchar [124] or the NeQuick model [125, 126]. However, the inclusion of these models could obscure the analysis of this work that focuses on the effects of the satellite dynamic.

$$\upsilon_i = \frac{f}{c}\hat{r}^T \left(\vec{v}_{SAT} - \vec{v}_{UE}\right) \tag{B.1}$$

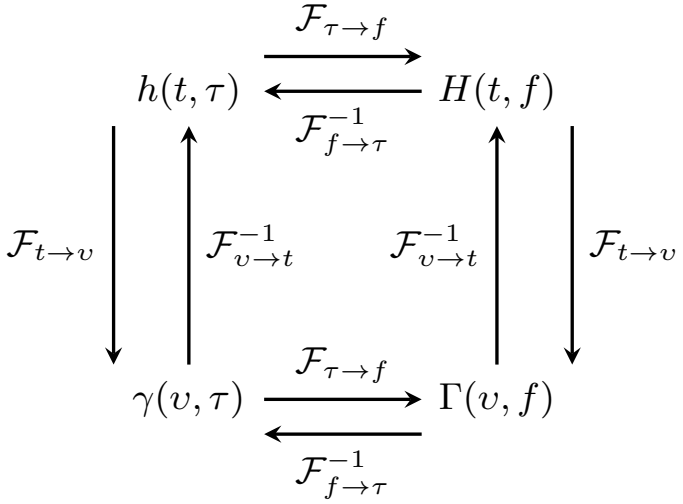

Fig. B.2: Different channel model representations

The Doppler shift υ_i in (B.1) is considered constant. It is expressed in terms of the projection of the relative speed between the satellite and the user on the unitary vector from the user to the satellite.

B.4 Received signal model

$$y(t) = \sum_{i=0}^{S-1} h_i \otimes x(t) = \sum_{i=0}^{S-1} L_i e^{j2\pi\upsilon_i t} x_i(t-\tau_i) \tag{B.2}$$

The received signal $y(t)$, represented in (B.2), is the aggregation of the signals from S different satellites in view of the ground user, where each satellite i applies to its transmitted signal $x_i(t)$ a specific delay τ_i, Doppler υ_i, phase h_i and channel gain L_i.

Appendix C

PVT engines

This appendix, where it is not a published contribution, it has been presented in the Technical Note for the project SATNEXT Y3.3 LEO-PNT. And it serves as a closing of the thesis technical chapters by modeling the observables and estimating the final UE position.

There are several algorithms for positioning estimation. Table C.1 shows a summary of the different algorithms used in the literature to estimate the UE state (position and/or velocity and clock) with some references where each algorithm is implemented. The algorithms are only those for one-way positioning. There are other options as two way positioning, where both devices, transmit and receive a signal, but they are out of the scope of this project.

C.1 Measurement models

In the PNT estimation analysis, the following measurement models were applied, the pseudorange and the Doppler shift.

Table C.1: Positioning algorithms

Algorithm	**UE state estimation**	**Minimum observables**	**Reference**
Range	$[x, y, z, \delta_{UE}]$	4	[166]
Doppler	$[x, y, z, v_x, v_y, v_z, \dot{\delta_{UE}}]$	7	[167, 157]
Range, Doppler	$[x, y, z, v_x, v_y, v_z, \delta_{UE}, \dot{\delta_{UE}}]$	4	[168]
TDoA	$[x, y, z]$	4	[4, 169]

C.1.1 Pseudorange

The UE makes ToA measurements to all gNBs. Each ToA measurement contains the distance of the UE to each gNB (i.e., true range), the difference of the clock bias between the UE and the gNB, and measurement noise. By multiplying the estimated ToAs to the speed of light, pseudorange measurements can be obtained according to Equation C.1, where $\rho \triangleq \left[\rho^{(1)}, ..., \rho^{(U)}\right]^T$ is the vector of pseudorange measurements; $\mathbf{d} \triangleq \left[d^{(1)}, ..., d^{(U)}\right]^T$ is the vector of ranges; $\mathbf{b} \triangleq \left[b^{(1)}, ..., b^{(U)}\right]^T$ is the vector of clock biases with mean μ_b and covariance matrix $\sum_b$; and $\epsilon \triangleq \left[\epsilon^{(1)}, ..., \epsilon^{(U)}\right]^T$, the measurement noise modeled as zero-mean Gaussian random variable with standard deviation of $\sigma_\tau^{(i)}$.

$$\rho = \mathbf{d} + \mathbf{b} + \epsilon \tag{C.1}$$

Since the effect of the clock bias and the noise are independent, the covariance matrix of ρ can be obtained by Equation C.2 where $\sum_\epsilon = \text{diag}\left[\sigma_\tau^{(1)}, ..., \sigma_\tau^{(U)}\right]$

$$\sum\nolimits_\rho \triangleq \text{cov}\left\{\rho\right\} = \sum\nolimits_b + \sum\nolimits_\epsilon \tag{C.2}$$

C.1.2 Doppler shift

The measurement model of the Doppler shift came from its definition as shown in Equation C.3. It shows that the Doppler measured is proportional to the relative speed of the satellite-user link.

$$f_D(t) = \frac{f_0}{c}\frac{d}{dt}\rho(t) \tag{C.3}$$

Where $\frac{d}{dt}\rho_n(t) = \frac{\vec{r}_{SATn} - \vec{r}_{UE}}{||\vec{r}_{SATn} - \vec{r}_{UE}||}\left(\vec{v}_{SATn} - \vec{v}_{UE}\right) = \hat{u}_{SATn}^T \vec{v}_{SATn,UE}$

The model from Equation C.3 is in an ideal scenario, where the measurement is only affected by the dynamics of the satellite and user. This model will serve as a baseline for a performance analysis.

C.2 Engine performance

C.2.1 Initial estimation

As initial estimation for the state estimation $\mathbf{r}_0 = [x_0, y_0, z_0]$ we use the projection of the satellites centroid into the world geodetic system 84 (WGS84). The reason behind this

method is to reduce the number of iterations of the algorithm to converge to a solution. This satellite centroid is computed as the mean value of the satellites position $\mathbf{r}_{\text{SAT centroid}} = \frac{1}{N}\sum_{i=0}^{N}[x_i, y_i, z_i]^T$. Then, this point is projected perpendicular into the WGS84 as:

1. Compute the eccentricities $e^2 = \frac{a^2-b^2}{a^2}$, $e'^2 = \frac{a^2-b^2}{b^2}$
2. Convert cartesian coordinates to Geodetic coordinates:
   (a) Initial calculations: $p = sqrtx^2 + y^2$, $\theta = \arctan\left(\frac{za}{pb}\right)$
   (b) Calculate latitude $\phi = \arctan\left(\frac{z+e'^2 b\sin^3(\theta)}{p-e^2 a\cos^3(\theta)}\right)$
   (c) Calculate longitude $\lambda = \arctan\left(\frac{y}{x}\right)$
3. Compute the height h
   (a) Calculate the radius of curvature in the prime vertical $N = \frac{a}{\sqrt{1-e^2\sin^2(\phi)}}$
   (b) Calculate height $h = \frac{p}{\cos(\phi)} - N$
4. Project the centroid onto the ellipsoid's surface:
   (a) Set height $h = 0$
   (b) Compute new Cartesian coordinates for the initial estimation as: $x_0 = N\cos(\phi)\cos(\lambda)$, $y_0 = N\cos(\phi)\sin(\lambda)$, $z_0 = \left(1-e^2\right)N\sin(\phi)$

C.2.2 First estimation using EKF

Once the initial estimation is obtained, we solve the user state $\mathbf{x}$ by using a EKF. The EKF estimation process can be modelled by the following equations:

1. Prediction step. It estimates what is going to be the state $\mathbf{x}_{k+1}$ at time $k+1$ from on the previous state $\mathbf{x}_k$ at time k based on the state transition matrix $\mathbf{F}$

$$\hat{\mathbf{x}}_{k+1} = \mathbf{F}\mathbf{x}_k \tag{C.4}$$

2. After the state prediction, it is necessary to update the covariance matrix of the error in the prediction $\mathbf{P}$ using the matrix $\mathbf{Q}$ as the process noise covariance, or how good is our model $\mathbf{F}$ to the reality:

$$\mathbf{P}_{k+1} = \mathbf{F}\mathbf{P}_k\mathbf{F}^T + \mathbf{Q} \tag{C.5}$$

3. The state update with the measurements. The measurement model we have seen before in (C.3), $h = -\frac{f_0}{c}\mathbf{u}_{\text{SAT,UE}}^T\mathbf{v}_{\text{SAT,UE}}$ is used to update the prediction done in the previous step $\hat{\mathbf{x}}_{k+1}$

$$\mathbf{y}_{k+1} = \mathbf{z}_{k+1} - h\left(\hat{\mathbf{x}}_{k+1}\right) \tag{C.6}$$

4. Then it is required to update the measurement covariance matrix $\mathbf{S}_{k+1}$ using the Jacovian of the measurement model $\mathbf{H}$ and the measurement noise covariance matrix $\mathbf{R}$

$$\mathbf{S}_{k+1} = \mathbf{H}_{k+1}\mathbf{P}_{k+1}\mathbf{H}_{k+1}^T + \mathbf{R} \tag{C.7}$$

5. Then the Kalman gain is obtained as: $\mathbf{K}_{k+1} = \mathbf{P}_{k+1}\mathbf{H}_{k+1}^T\mathbf{S}_{k+1}^{-1}$

6. With the Kalman gain, the final state estimation can be obtained: $\mathbf{x}_{k+1} = \hat{\mathbf{x}}_{k+1} + \mathbf{K}_{k+1}\mathbf{y}_{k+1}$

7. And finally update the covariance matrix of the error in the prediction $\mathbf{P}_{k+1} = \left(\mathbf{I} - \mathbf{K}_{k+1}\mathbf{H}_{k+1}\right)\mathbf{P}_k$

This EKF models used in our scenario are the following:

- State transition matrix $\mathbf{F}$. Defines how the user state (position in our case) evolve in time. As we assume static user the user position will not change from time k to time $k+1$ therefore the state transition matrix can be defined as the identity matrix $\mathbf{F} = I$
- Process noise covariance matrix $\mathbf{Q}$. Defined as the error we have between the real user movement and the model in the state transition matrix. From the simulations the user did not move, therefore the state transition model do not have an error, therefore $\mathbf{Q} = 0$.
- Measurement model h define how the user position is related with the measurements and its Jacobian matrix of the measurement model $\mathbf{H} = \left[\frac{\partial h}{\partial x}, \frac{\partial h}{\partial y}, \frac{\partial h}{\partial z}\right]$.
- Measurement noise covariance matrix $\mathbf{R} = \sigma_f^2$. Define how good are the measurements.

Therefore the estimation of the user position can be obtained by an iterative process using the EKF until any of two conditions occurs:

1. The number of iterations reach a limit and, therefore, no estimation is obtained.
2. The change in the estimation between iterations is below a certain tolerance value. Therefore a local minimum is reached.

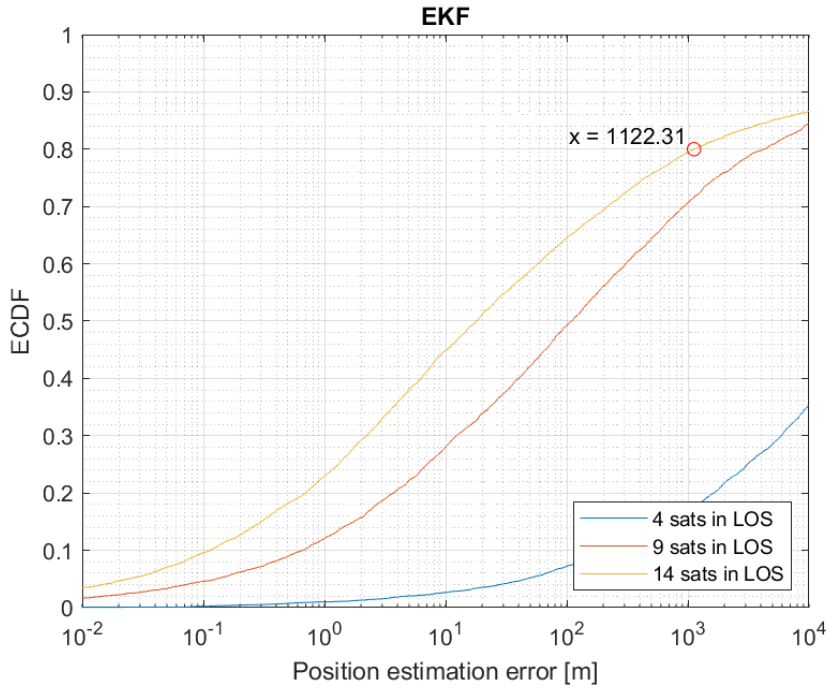

Fig. C.1: User position estimation error using only EKF and different number of observables

Something to take into account is the condition that the user is in the surface of the Earth, modeled by WGS84, therefore to set this condition, in every iteration we project the solution into the ellipsoid.

$$||\hat{\mathbf{r}}|| = f_R(\mathbf{r}) = \frac{x^2}{a^2} + \frac{y^2}{a^2} + \frac{z^2}{b^2} - 1 \tag{C.8}$$

Where the condition in (C.8) is the assumption that the user is at the Earth surface, defined by the function $f_R(\mathbf{r})$, as WGS84 reference frame for the Earth surface with parameters $a = 6378137.0$ meters as the semi-major axis, $b = a(1 - f)$ is the semi-minor axis and $f = \frac{1}{298.257223563}$ the flattening constant.

As a performance metric we use the Euclidean norm $\|r\|$ between the true position and the estimated one. The rationale for using this metric is that it is easier to interpret in a localization framework as the error distance from the true position.

Fig. C.1 shows the accuracy of using the EKF as an estimator for the user position using Doppler measurements.

C.2.3 Fine estimation using non linear least squares

Then, to refine the position estimation we use a non-linear least squared method to further improve the estimation, as the EKF alone is not enough to achieve most of the typical use cases requirements.

From the measurement models developed in Section C.1. We derive the cost function in Equation C.9. This cost function is the mean square error (MSE) between the Doppler measured, and the Doppler modelled.

$$\mathcal{L} = |\hat{\mathbf{f}}_D - \frac{f_0}{c}\hat{\mathbf{u}}_{SAT,UE}^T \mathbf{v}_{SAT,UE}|^2, \tag{C.9}$$

where $\hat{\mathbf{f}}_{D,k} = [f_D^1(t_k), f_D^2(t_k), ..., f_D^N(t_k)]$ are the Doppler measurements from N satellites at time t_k; $\hat{\mathbf{u}}_{SATn,UE}^T = [\hat{u}_{SAT,1,UE}, \hat{u}_{SAT,2,UE}, ..., \hat{u}_{SAT,N,UE}]^T$ is the transposed unitary vector pointing from the UE to the satellite n; and $\mathbf{v}_{SATn,UE} = [\vec{v}_{SAT,1,UE}, \vec{v}_{SAT,2,UE}, ..., \vec{v}_{SAT,N,UE}]$ is the relative speed between the N satellites and the user. This speed has to take into account the Earth rotation for the user.

Table C.1 shows that at least 4 Doppler measurement are needed in order to estimate the UE state $\hat{\mathbf{r}} = [x, y, z]$ as we assume the terminal is not moving. Therefore, using the cost function, the position estimation becomes a non-linear optimization problem, defined by Equation C.10.

$$\hat{\mathbf{r}} = \arg\min_{\hat{\mathbf{r}}} \mathcal{L} \tag{C.10}$$

Subject to the same assumption in (C.8) that the user is on the WGS84 ellipsoid.

Fig. C.2 shows the estimation accuracy using only the Non-Linear Least-Square algorithm, with the initial estimation as the projection of the satellites centroid on the WGS84 ellipsoid.

Finally, Fig. C.3 shows the accuracy of the estimation by first using the EKF and later refine the position by using the same algorithm previously mentioned for non-linear least squares.

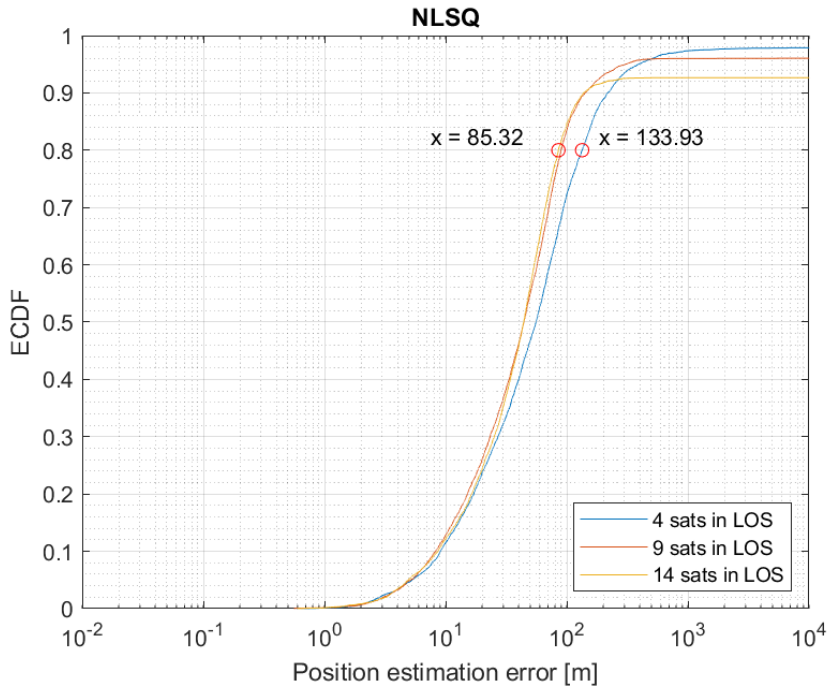

Fig. C.2: User position estimation error using only Non Linear Least-Squares Algorithm

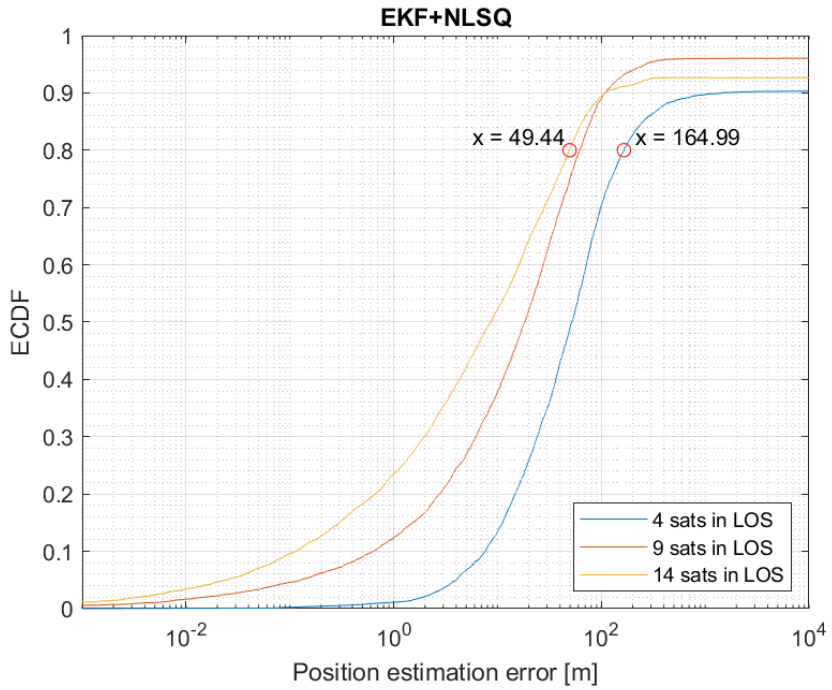

Fig. C.3: User position estimation error by initializing the Non-Linear Least-Squares Algorithm using the results from the EKF

Appendix D

List of contributions

The following list contain all the contributions and activities done during the Ph.D. duration.

D.1 Journals

1. A. Gonzalez-Garrido, J. Querol, H. Wymeersch and S. Chatzinotas, "Interference Analysis and Modeling of Positioning Reference Signals in 5G NTN," in IEEE Open Journal of the Communications Society, vol. 5, pp. 7567-7581, 2024, doi: https://doi.org/10.1109/OJCOMS.2024.3503692

2. A. Gonzalez-Garrido, J. Querol, H. Wymeersch and S. Chatzinotas, "Joint Communication and Navigation From LEO Multi-Beam Satellite," in IEEE Open Journal of the Communications Society, doi: https://doi.org/10.1109/OJCOMS.2025.3568093

3. A. Gonzalez-Garrido, I. Edjekouane, J. Querol, H. Wymeersch and S. Chatzinotas, "Joint communication and positioning receiver architecture for DSSS-overlayed OFDM waveform," IEEE Open Journal of the Communications Society, doi: https://doi.org/10.1109/OJCOMS.2025.3615957

4. I. Edejekouane, A. Gonzalez-Garrido, J. Querol, S. Chatzinotas, "User Equivalent Range Error and Positioning Accuracy Analysis for ToA-Based Techniques Using PRS and SSB in 5G/6G NTN". Accepted in IEEE Open Journal of the Communications Society.

5. C. Kumar Sheemar, J. Querol, S. Solanki, A. Gonzalez-Garrido, S. Chatzinotas, "Joint Communications, Sensing, and Positioning in 6G Multi-Functional Satellite Systems: Survey and Open Challenges". Submitted to Communications Surveys & Tutorials.

D.2 Conferences

1. A. Gonzalez-Garrido, O. Picchi, F. Menzione, J. Querol, S. Chatzinotas, "Assessing 5G PRS Signal Interference in High Frequency NTN Fused PNT Applications," IEEE 12th International Workshop on Metrology for AeroSpace (MetroAeroSpace) 2025, Napoli, Italy, doi: https://doi.org/10.1109/MetroAeroSpace64938.2025.11114545

2. G. -G. Alejandro, Q. Jorge and C. Symeon, "Analysis of the SINR in LEO-PNT Systems with 5G PRS Multiplexing: Integration of PRS and NTN," ICASSP 2024 - 2024 IEEE International Conference on Acoustics, Speech and Signal Processing (ICASSP), Seoul, Korea, Republic of, 2024, pp. 13016-13020, doi: https://doi.org/10.1109/ICASSP48485.2024.10447159

3. A. Gonzalez-Garrido, J. Querol and S. Chatzinotas, "5G Positioning Reference Signal Configuration for Integrated Terrestrial/Non-Terrestrial Network Scenario," 2023 IEEE/ION Position, Location and Navigation Symposium (PLANS), Monterey, CA, USA, 2023, pp. 1136-1142, doi: https://doi.org/10.1109/PLANS53410.2023.10140024

4. Gonzalez-Garrido, Alejandro, Querol, Jorge, Chatzinotas, Symeon, "Hybridization of GNSS and 5G Measurements for Assured Positioning, Navigation and Timing," Proceedings of the 35th International Technical Meeting of the Satellite Division of The Institute of Navigation (ION GNSS+ 2022), Denver, Colorado, September 2022, pp. 2377-2384. https://doi.org/10.33012/2022.18385

5. I. Larráyoz-Arrigote et al., "ML-based PBCH symbol detection and equalization for 5G Non-Terrestrial Networks," 2024 IEEE International Mediterranean Conference on Communications and Networking (MeditCom), Madrid, Spain, 2024, pp. 119-124, doi: https://doi.org/10.1109/MeditCom61057.2024.10621238

D.3 Other contributions

1. A. Gonzalez-Garrido, P. Kaliyammal Thiruvasagam, J. Querol, "An overview of 6G Multi-Functional Satellite Systems for Communication, Sensing and Positioning," 12th Advanced Satellite Multimedia Systems Conference (ASMS), Sitges, Barcelona (Spain).

2. Sumit Kumar, Amirhossein NIK, Jorge Querol, Alejandro GONZÁLEZ GARRIDO, Symeon Chatzinotas, "Integrated Access and Backhauling in 5G-NTN using Open Air

Interface 5G," demo presented at the 2024 IEEE International Conference on Acoustics, Speech, and Signal Processing (ICASSP 2024)

3. Abdelrahman, Astro, Gonzalez-Garrido, Alejandro, "Earth-Moon Communication and ROVER Teleoperation Via 5G-NR", poster and demo presented at Fall 2022 OAI North American Workshop. San Diego, November 2022.

4. Alejandro Gonzalez-Garrido, "Starlink satellite passes", IEEE Dataport, April 29, 2024, doi:`https://doi.org/10.21227/qggt-xr49`

D.4 Book chapter

1. J. Querol, A. Gonzalez, V. Nguyen Ha, S. Kumar, and S. Chatzinotas, "Wireless and networking technologies for social distancing - indoor and outdoor," Enabling Technologies for Social Distancing, pp. 67–111, doi: `https://doi.org/10.1049/PBTE104E_ch3`.

D.5 Thesis co-supervised

1. Larráyoz Arrigote, Inés, "Comparision of Doppler tracking techniques for Starlink satellite signals".

D.6 Projects involved

1. **ESA SATNEXT V. Y3.3 LEO-PNT**. PNT is an essential service for modern societies. Also in the context of satellite communication, positioning capabilities are very important, e.g., to close the link between a receiver and a LEO satellite. Due to the vulnerabilities and drawbacks of the prevalent GNSS, there is an urgent need for additional PNT systems. This project focuses on investigating these LEO-PNT approaches. An analysis of the impact of different error sources on the resulting PNT accuracy is performed. The feasibility of different signals for use in such LEO-PNT systems is investigated. A Doppler-shift based PNT receiver is presented.

2. **5G LEON. RADIO POSITIONING TECHNOLOGIES FOR 5G SATELLITE NETWORKS**. The project perform system and technology trade-offs available within 5G satellite networks relevant for positioning in FR1 and FR2; Study the performance

and sensitivity of the different architectures and associated key technologies for enabling the use of 5G satellite networks for positioning in light of the consolidated use cases; Demonstrate the key enabling technologies using experimental proof-of-concept; Gather lessons learned, recommendations, and ways forward relevant in what concerns positioning with 5G satellite networks.

3. **SMS2**. SMS2 focuses on the paradigm of concurrent communications, sensing and PNTs for the SS, which are able to combine two or three functionalities seamlessly and concurrently into the same frequency band and/or same hardware and/or same transmit signal. We will refer to such systems as Multi-Functional SS (MFSS) and can be classified in three different levels of interaction spanning frequency bands, hardware and transmit signal. Henceforth, at the first level we categorize cooperative systems in which the traditional operation of the communications, sensing and PNT systems share the same hardware but still operate with their own signals in adjacent or same frequency bands. At the second level, in integrated systems the three services will share the same hardware and frequency bands, but signals will be transmitted multiplexed in different domains (e.g., time, space). Finally, at the final level, in joint systems the three services will operate with the same frequency, hardware, and a common transmit signal.

4. **5G Sky**. Low-altitude unmanned aerial vehicles (UAVs), commonly referred to as drones, have proliferated a plethora of personal and commercial applications including aerial photography and sightseeing, parcel delivery, search-and-rescue, monitoring and surveillance, and precision farming. Improving the operation range and safety of the drones has led to increasing interest in connecting drones over licensed spectrum as three-dimensional (3D) aerial users and employing the fifth-generation (5G) cellular infrastructure for reliable beyond-visual-line-of-sight communication and control. On the other hand, drones with flexible mobility and large payload also enable aerial base stations (BSs) to establish, enhance, and recover cellular coverage in real-time for ground users in remote, densely populated, and disastrous areas, unlocking an unprecedented opportunity for intelligent cellular network operation in both normal and emergent scenarios. To address the socioeconomic impact of emerging aerial users and aerial BSs, this project will study cellular-connected drones via (i) assessing the applicability of 5G new radio (NR) technologies and the required enhancements towards reliable, long-range, and efficient drone communication and control, (ii) resolving key challenges for drone communication and control through novel hardware (such as

antenna design and deployment) and software (including communication protocols, control schemes, signal processing algorithms, and network architectures) designs, (iii) investigating the impact of 3D mobile drones and necessary changes on 5G terrestrial communication, signal processing, resource allocation and networking, and (iv) testing drone communication and control with practical experimentation setups and in real national 5G testbeds.

Appendix E

References

[1] 3GPP. *Study on NR positioning support*. Technical Report (TR) 38.855. 3GPP, 2019. URL: https://portal.3gpp.org/desktopmodules/Specifications/SpecificationDetails.aspx?specificationId=3501.

[2] Adrián Cardalda García, Stefan Maier, and Abhay Phillips. *Location-based services in cellular networks from GSM to 5G NR*. en. GNSS technology and applications series. Boston [MA]: Artech House, 2020. ISBN: 978-1-63081-634-6.

[3] Lorenzo Italiano et al. "A Tutorial on 5G Positioning". In: *IEEE Communications Surveys & Tutorials* (2024). Conference Name: IEEE Communications Surveys & Tutorials, pp. 1–1. ISSN: 1553-877X. DOI: 10.1109/COMST.2024.3449031. URL: https://ieeexplore.ieee.org/document/10644093 (visited on 01/20/2025).

[4] Ivo Muursepp et al. "Performance Evaluation of 5G-NR Positioning Accuracy Using Time Difference of Arrival Method". en. In: *2021 IEEE International Mediterranean Conference on Communications and Networking (MeditCom)*. Athens, Greece: IEEE, Sept. 2021, pp. 494–499. ISBN: 978-1-66544-505-4. DOI: 10.1109/MeditCom49071.2021.9647652. URL: https://ieeexplore.ieee.org/document/9647652/ (visited on 11/01/2022).

[5] M. Panchetti et al. "Performance analysis of PRS-based synchronization algorithms for LTE positioning applications". en. In: *2013 10th Workshop on Positioning, Navigation and Communication (WPNC)*. Dresden: IEEE, Mar. 2013, pp. 1–6. DOI: 10.1109/WPNC.2013.6533292. URL: http://ieeexplore.ieee.org/document/6533292/ (visited on 11/01/2022).

[6] Satyam Dwivedi et al. “Positioning in 5G Networks”. In: *IEEE Communications Magazine* 59.11 (Nov. 2021). Conference Name: IEEE Communications Magazine, pp. 38–44. ISSN: 1558-1896. DOI: 10.1109/MCOM.011.2100091. URL: https://ieeexplore.ieee.org/document/9665436 (visited on 01/17/2024).

[7] E.D. Kaplan and C.J. Hegarty. *Understanding GPS: Principles and applications*. Artech house mobile communications. tex.lccn: 2005056270. Artech House, 2006. ISBN: 978-1-58053-894-7.

[8] Federica Rinaldi et al. “Non-Terrestrial Networks in 5G & Beyond: A Survey”. In: *IEEE Access* 8 (2020). Conference Name: IEEE Access, pp. 165178–165200. ISSN: 2169-3536. DOI: 10.1109/ACCESS.2020.3022981.

[9] Mohamed El Jaafari et al. “Introduction to the 3GPP-defined NTN standard: A comprehensive view on the 3GPP work on NTN”. en. In: *International Journal of Satellite Communications and Networking* 41.3 (2023), pp. 220–238. ISSN: 1542-0981. DOI: 10.1002/sat.1471. URL: https://onlinelibrary.wiley.com/doi/abs/10.1002/sat.1471 (visited on 05/30/2023).

[10] C4ADS. *Above Us Only Stars. Exposing GPS Spoofing in Russia and Syria*. Tech. rep. C4ADS, 2019.

[11] Antoine Grenier et al. “A Survey on Low-Power GNSS”. In: *IEEE Communications Surveys & Tutorials* 25.3 (2023). Conference Name: IEEE Communications Surveys & Tutorials, pp. 1482–1509. ISSN: 1553-877X. DOI: 10.1109/COMST.2023.3265841. URL: https://ieeexplore.ieee.org/document/10097786 (visited on 08/01/2024).

[12] Zheng Zhou, Nicola Accettura, and Pascal Berthou. “A Wake-up Strategy Enabling GNSS-Free NB-IoT Links to Sparse LEO Satellite Constellations”. In: *IEEE Internet of Things Journal* (2025), pp. 1–1. ISSN: 2327-4662. DOI: 10.1109/JIOT.2025.3551911. URL: https://ieeexplore.ieee.org/document/10929718 (visited on 06/03/2025).

[13] Alejandro Gonzalez-Garrido, Jorge Querol, and Symeon Chatzinotas. “5G Positioning Reference Signal Configuration for Integrated Terrestrial/Non-Terrestrial Network Scenario”. In: *2023 IEEE/ION Position, Location and Navigation Symposium (PLANS)*. Monterey, CA, USA: IEEE, Apr. 2023, pp. 1136–1142. DOI: 10.1109/PLANS53410.2023.10140024. URL: https://ieeexplore.ieee.org/document/10140024/ (visited on 09/07/2023).

[14] José A. Del Peral-Rosado et al. “Positioning-Enabled 5G and 6G Satellite Networks: Use Cases and Key Technologies”. In: *2024 11th Workshop on Satellite Navigation Technology (NAVITEC)*. ISSN: 2325-5455. Dec. 2024, pp. 1–5. DOI: 10.1109/NAVITEC63575.2024.10843544. URL: https://ieeexplore.ieee.org/document/10843544 (visited on 02/05/2025).

[15] Stylianos E. Trevlakis et al. “Localization as a Key Enabler of 6G Wireless Systems: A Comprehensive Survey and an Outlook”. In: *IEEE Open Journal of the Communications Society* 4 (2023). Conference Name: IEEE Open Journal of the Communications Society, pp. 2733–2801. ISSN: 2644-125X. DOI: 10.1109/OJCOMS.2023.3324952. URL: https://ieeexplore.ieee.org/document/10287134/references#references (visited on 11/09/2023).

[16] *6G-NTN*. en-US. Jan. 2023. URL: https://6g-ntn.eu/ (visited on 07/14/2025).

[17] Alessandro Guidotti et al. “The path to 5G-Advanced and 6G non-terrestrial network systems”. In: *2022 11th advanced satellite multimedia systems conference and the 17th signal processing for space communications workshop (ASMS/SPSC)*. tex.organization: IEEE. 2022, pp. 1–8.

[18] Harish K. Dureppagari et al. “NTN-Based 6G Localization: Vision, Role of LEOs, and Open Problems”. In: *IEEE Wireless Communications* 30.6 (Dec. 2023). Conference Name: IEEE Wireless Communications, pp. 44–51. ISSN: 1558-0687. DOI: 10.1109/MWC.007.2300224. URL: https://ieeexplore.ieee.org/document/10355106 (visited on 01/12/2024).

[19] Zhiqing Wei et al. “5G PRS-Based Sensing: A Sensing Reference Signal Approach for Joint Sensing and Communication System”. In: *IEEE Transactions on Vehicular Technology* 72.3 (Mar. 2023). Conference Name: IEEE Transactions on Vehicular Technology, pp. 3250–3263. ISSN: 1939-9359. DOI: 10.1109/TVT.2022.3215159.

[20] Moeinreza Golzadeh et al. “Joint Sensing and UE Positioning in 5G-6G: PRS Range Estimation with Suppressed Ambiguity”. In: *2024 IEEE Radar Conference (RadarConf24)*. ISSN: 2375-5318. May 2024, pp. 1–6. DOI: 10.1109/RadarConf2458775.2024.10548650. URL: https://ieeexplore.ieee.org/document/10548650 (visited on 07/02/2025).

[21] Joerg Widmer et al. “Enablers Toward 6G Positioning and Sensing”. en. In: *Positioning and Location-based Analytics in 5G and Beyond*. Section: 4 _eprint: https://onlinelibrary.wiley.com/doi/pdf/10.1002/9781119911463.ch4. John Wiley &

Sons, Ltd, 2023, pp. 75–97. ISBN: 978-1-119-91146-3. DOI: 10.1002/9781119911463.ch4. URL: https://onlinelibrary.wiley.com/doi/abs/10.1002/9781119911463.ch4 (visited on 07/02/2025).

[22] Xinran Fang et al. "Joint Communication and Sensing Toward 6G: Models and Potential of Using MIMO". In: *IEEE Internet of Things Journal* 10.5 (Mar. 2023), pp. 4093–4116. ISSN: 2327-4662. DOI: 10.1109/JIOT.2022.3227215. URL: https://ieeexplore.ieee.org/document/9971740/ (visited on 07/02/2025).

[23] Alejandro Gonzalez-Garrido et al. "Joint Communication and Navigation From LEO Multi-Beam Satellite". In: *IEEE Open Journal of the Communications Society* (2025), pp. 1–1. ISSN: 2644-125X. DOI: 10.1109/OJCOMS.2025.3568093. URL: https://ieeexplore.ieee.org/document/10993443 (visited on 05/14/2025).

[24] Noah S. Miller et al. "SNAP: A Xona Space Systems and GPS Software-Defined Receiver". en. In: *2023 IEEE/ION Position, Location and Navigation Symposium (PLANS)*. Monterey, CA, USA: IEEE, Apr. 2023, pp. 897–904. ISBN: 978-1-66541-772-3. DOI: 10.1109/PLANS53410.2023.10139956. URL: https://ieeexplore.ieee.org/document/10139956/ (visited on 04/10/2024).

[25] Lionel Ries et al. "LEO-PNT for Augmenting Europe's Space-based PNT Capabilities". In: *2023 IEEE/ION Position, Location and Navigation Symposium (PLANS)*. ISSN: 2153-3598. Apr. 2023, pp. 329–337. DOI: 10.1109/PLANS53410.2023.10139999. URL: https://ieeexplore.ieee.org/document/10139999/ (visited on 11/14/2023).

[26] Mayank et al. "LEO-PNT Feasibility Aspects: Satellite Navigation Payload Size, Weight, and Power Analysis". In: *IEEE Access* 13 (2025), pp. 110069–110089. ISSN: 2169-3536. DOI: 10.1109/ACCESS.2025.3583080. URL: https://ieeexplore.ieee.org/document/11050377/ (visited on 07/14/2025).

[27] Inside GNSS. *SpaceX Details Starlink's Existing and Potential PNT Capabilities in Response to FCC Inquiry*. en-US. May 2025. URL: https://insidegnss.com/spacex-details-starlinks-existing-and-potential-pnt-capabilities-in-response-to-fcc-inquiry/ (visited on 06/03/2025).

[28] Eldar Rubinov et al. *LEO PNT State of the Market Report: A Comprehensive Look at the Future of Satellite Navigation*. EN. Tech. rep. 2024 Edition. FrontierSI, Jan. 2025, p. 56. URL: https://frontiersi.com.au/wp-content/uploads/2025/01/FrontierSI-State-of-Market-Report-LEO-PNT-2024-Edition-v1.1.pdf.

[29] Florin Grec. *Synergies between disruptive satellite navigation systems in LEO orbit and 5G NTN*. EN. ETSI, Mar. 2024. URL: https://docbox.etsi.org/Workshop/2024/04_ETSI_6G_NTN/SESSION%2002/S2_06_Grec.pdf.

[30] F. S. Prol et al. "Position, Navigation, and Timing (PNT) Through Low Earth Orbit (LEO) Satellites: A Survey on Current Status, Challenges, and Opportunities". en. In: *IEEE Access* 10 (2022), pp. 83971–84002. ISSN: 2169-3536. DOI: 10.1109/ACCESS.2022.3194050. URL: https://ieeexplore.ieee.org/document/9840374/ (visited on 11/01/2022).

[31] Mohammad Neinavaie, Joe Khalife, and Zaher M. Kassas. "Exploiting Starlink Signals for Navigation: First Results". en. In: St. Louis, Missouri, Oct. 2021, pp. 2766–2773. DOI: 10.33012/2021.18122. URL: https://www.ion.org/publications/abstract.cfm?articleID=18122 (visited on 01/26/2024).

[32] Riccardo De Gaudenzi. "An Integrated LEO Communication and PNT System for Beyond 5G NTN". In: *Wiley International Journal of Satellite Communications and Networking* (2024).

[33] Jun Mo et al. "A Novel FLL-Assisted PLL With Fuzzy Control for TC-OFDM Carrier Signal Tracking". en. In: *IEEE Access* 6 (2018), pp. 52447–52459. ISSN: 2169-3536. DOI: 10.1109/ACCESS.2018.2870908. URL: https://ieeexplore.ieee.org/document/8467327/ (visited on 04/10/2024).

[34] J.J. van de Beek, M. Sandell, and P.O. Borjesson. "ML estimation of time and frequency offset in OFDM systems". en. In: *IEEE Transactions on Signal Processing* 45.7 (July 1997), pp. 1800–1805. ISSN: 1053587X. DOI: 10.1109/78.599949. URL: http://ieeexplore.ieee.org/document/599949/ (visited on 11/01/2022).

[35] Zdenek Chaloupka. "Technology and Standardization Gaps for High Accuracy Positioning in 5g". en. In: *IEEE Communications Standards Magazine* 1.1 (Mar. 2017), pp. 59–65. ISSN: 2471-2825, 2471-2833. DOI: 10.1109/MCOMSTD.2017.1601030ST. URL: http://ieeexplore.ieee.org/document/7885240/ (visited on 11/05/2022).

[36] Xingqin Lin et al. "Positioning for the Internet of Things: A 3GPP Perspective". In: *IEEE Communications Magazine* 55.12 (Dec. 2017). Conference Name: IEEE Communications Magazine, pp. 179–185. ISSN: 1558-1896. DOI: 10.1109/MCOM.2017.1700269. URL: https://ieeexplore.ieee.org/document/8030544 (visited on 05/14/2024).

[37] Gianluca Torsoli, Moe Z. Win, and Andrea Conti. "Beyond 5G Localization at mm Waves in 3GPP Urban Scenarios with Blockage Intelligence (Invited Paper)". In: *2023 IEEE/ION Position, Location and Navigation Symposium (PLANS)*. ISSN: 2153-3598. Apr. 2023, pp. 354–359. DOI: 10.1109/PLANS53410.2023.10140112. URL: https://ieeexplore.ieee.org/document/10140112/ (visited on 11/14/2023).

[38] Jose A. del Peral-Rosado et al. "Survey of Cellular Mobile Radio Localization Methods: From 1G to 5G". en. In: *IEEE Communications Surveys & Tutorials* 20.2 (2018), pp. 1124–1148. ISSN: 1553-877X. DOI: 10.1109/COMST.2017.2785181. URL: https://ieeexplore.ieee.org/document/8226757/ (visited on 11/01/2022).

[39] Christos Laoudias et al. "A Survey of Enabling Technologies for Network Localization, Tracking, and Navigation". en. In: *IEEE Communications Surveys & Tutorials* 20.4 (2018), pp. 3607–3644. ISSN: 1553-877X, 2373-745X. DOI: 10.1109/COMST.2018.2855063. URL: https://ieeexplore.ieee.org/document/8409950/ (visited on 11/01/2022).

[40] Sven Fischer. "5G NR Positioning". en. In: *5G and Beyond: Fundamentals and Standards*. Ed. by Xingqin Lin and Namyoon Lee. Cham: Springer International Publishing, 2021, pp. 429–483. ISBN: 978-3-030-58197-8. DOI: 10.1007/978-3-030-58197-8_15. URL: https://doi.org/10.1007/978-3-030-58197-8_15 (visited on 11/01/2022).

[41] Mohsen Hosseinian et al. "Review of 5G NTN Standards Development and Technical Challenges for Satellite Integration With the 5G Network". In: *IEEE Aerospace and Electronic Systems Magazine* 36.8 (Aug. 2021). Conference Name: IEEE Aerospace and Electronic Systems Magazine, pp. 22–31. ISSN: 1557-959X. DOI: 10.1109/MAES.2021.3072690. URL: https://ieeexplore.ieee.org/document/9508471/?arnumber=9508471 (visited on 10/09/2024).

[42] Alda Xhafa et al. "Evaluation of 5G Positioning Performance Based on UTDoA, AoA and Base-Station Selective Exclusion". en. In: *Sensors* 22.1 (Dec. 2021), p. 101. ISSN: 1424-8220. DOI: 10.3390/s22010101. URL: https://www.mdpi.com/1424-8220/22/1/101 (visited on 12/11/2022).

[43] Roman Klus, Jukka Talvitie, and Mikko Valkama. "Neural Network Fingerprinting and GNSS Data Fusion for Improved Localization in 5G". en. In: *2021 International Conference on Localization and GNSS (ICL-GNSS)*. Tampere, Finland: IEEE, June

2021, pp. 1–6. ISBN: 978-1-72819-644-2. DOI: 10.1109/ICL-GNSS51451.2021.9452245. URL: https://ieeexplore.ieee.org/document/9452245/ (visited on 11/05/2022).

[44] Elena Omelyanchuk et al. "User Equipment Positioning Algorithm for Mobile Networks". en. In: *2020 IEEE Conference of Russian Young Researchers in Electrical and Electronic Engineering (EIConRus)*. St. Petersburg and Moscow, Russia: IEEE, Jan. 2020, pp. 1715–1720. ISBN: 978-1-72815-761-0. DOI: 10.1109/EIConRus49466.2020.9039432. URL: https://ieeexplore.ieee.org/document/9039432/ (visited on 11/01/2022).

[45] Liang Chen et al. "Carrier Phase Ranging for Indoor Positioning With 5G NR Signals". en. In: *IEEE Internet of Things Journal* 9.13 (July 2022), pp. 10908–10919. ISSN: 2327-4662, 2372-2541. DOI: 10.1109/JIOT.2021.3125373. URL: https://ieeexplore.ieee.org/document/9601204/ (visited on 11/01/2022).

[46] Qing Li. "Hybrid Localization Based on Time of Arrival and Phase Difference of Arrival Fusion". In: *2019 IEEE International Conference on Signal Processing, Communications and Computing (ICSPCC)*. Sept. 2019, pp. 1–5. DOI: 10.1109/ICSPCC46631.2019.8960860. URL: https://ieeexplore.ieee.org/document/8960860 (visited on 07/25/2025).

[47] Yu Ge et al. "V2X Sidelink Positioning in FR1: Scenarios, Algorithms, and Performance Evaluation". In: *IEEE Journal on Selected Areas in Communications* 42.10 (Oct. 2024), pp. 2608–2624. ISSN: 1558-0008. DOI: 10.1109/JSAC.2024.3414579. URL: https://ieeexplore.ieee.org/document/10557665 (visited on 07/25/2025).

[48] Lu Bai et al. "GNSS-5G Hybrid Positioning Based on Multi-Rate Measurements Fusion and Proactive Measurement Uncertainty Prediction". en. In: *IEEE Transactions on Instrumentation and Measurement* 71 (2022), pp. 1–15. ISSN: 0018-9456, 1557-9662. DOI: 10.1109/TIM.2022.3154821. URL: https://ieeexplore.ieee.org/document/9721906/ (visited on 11/01/2022).

[49] Giuseppe Destino et al. "Performance Analysis of Hybrid 5G-GNSS Localization". en. In: *2018 52nd Asilomar Conference on Signals, Systems, and Computers*. Pacific Grove, CA, USA: IEEE, Oct. 2018, pp. 8–12. ISBN: 978-1-5386-9218-9. DOI: 10.1109/ACSSC.2018.8645207. URL: https://ieeexplore.ieee.org/document/8645207/ (visited on 11/01/2022).

[50] Jose A. del Peral-Rosado et al. “Exploitation of 3D City Maps for Hybrid 5G RTT and GNSS Positioning Simulations”. en. In: *ICASSP 2020 - 2020 IEEE International Conference on Acoustics, Speech and Signal Processing (ICASSP)*. Barcelona, Spain: IEEE, May 2020, pp. 9205–9209. ISBN: 978-1-5090-6631-5. DOI: 10.1109/ICASSP40776.2020.9053157. URL: https://ieeexplore.ieee.org/document/9053157/ (visited on 11/01/2022).

[51] Sara Modarres Razavi et al. “Positioning in cellular networks: Past, present, future”. In: *2018 IEEE Wireless Communications and Networking Conference (WCNC)*. ISSN: 1558-2612. Apr. 2018, pp. 1–6. DOI: 10.1109/WCNC.2018.8377447.

[52] Bernd Eissfeller et al. “A Comparative Study of LEO-PNT Systems and Concepts”. In: Honolulu, Hawaii, May 2024, pp. 758–782. DOI: 10.33012/2024.19646. URL: https://www.ion.org/publications/abstract.cfm?articleID=19646 (visited on 01/09/2025).

[53] Winfried Stock et al. “Survey On Opportunistic PNT With Signals From LEO Communication Satellites”. In: *IEEE Communications Surveys & Tutorials* (2024). Conference Name: IEEE Communications Surveys & Tutorials, pp. 1–1. ISSN: 1553-877X. DOI: 10.1109/COMST.2024.3406990. URL: https://ieeexplore.ieee.org/document/10542356 (visited on 01/21/2025).

[54] Peter A. Iannucci and Todd E. Humphreys. “Economical Fused LEO GNSS”. In: *2020 IEEE/ION Position, Location and Navigation Symposium (PLANS)*. Portland, OR, USA: IEEE, Apr. 2020, pp. 426–443. ISBN: 978-1-72810-244-3. DOI: 10.1109/PLANS46316.2020.9110140. URL: https://ieeexplore.ieee.org/document/9110140/ (visited on 02/14/2025).

[55] Ottavio M. Picchi et al. “Fused PNT on Future Wideband European Non-Terrestrial Network Infrastructure”. In: *LEO-PNT: Concepts, Systems and Use Cases*. Salt Lake City, Utah, Apr. 2025. URL: https://www.ion.org/plans/abstracts.cfm?paperID=15292.

[56] Peter A. Iannucci and Todd E. Humphreys. *Fused Low-Earth-Orbit GNSS*. en. arXiv:2009.12334 [eess]. Mar. 2022. URL: http://arxiv.org/abs/2009.12334 (visited on 11/01/2022).

[57] Tong Li et al. “Low pilot overhead channel estimation for CP-OFDM-based massive MIMO OTFS system”. en. In: *IET Communications* 16.10 (2022), pp. 1071–1082.

ISSN: 1751-8636. DOI: 10.1049/cmu2.12298. URL: https://onlinelibrary.wiley.com/doi/abs/10.1049/cmu2.12298 (visited on 07/02/2025).

[58] Shahid Ali, Dongsheng Zheng, and Bingli Jiao. "A new pilot shared method for saving bandwidth cost of OFDM". en. In: *Scientific Reports* 14.1 (Feb. 2024). Publisher: Nature Publishing Group, p. 4528. ISSN: 2045-2322. DOI: 10.1038/s41598-024-55153-y. URL: https://www.nature.com/articles/s41598-024-55153-y (visited on 07/02/2025).

[59] Qi Wang et al. "Efficient Channel Estimation for OFDM Systems with Reduced Pilot Overhead". In: *2023 IEEE 98th Vehicular Technology Conference (VTC2023-Fall)*. ISSN: 2577-2465. Oct. 2023, pp. 1–5. DOI: 10.1109/VTC2023-Fall60731.2023.10333619. URL: https://ieeexplore.ieee.org/document/10333619 (visited on 07/02/2025).

[60] Dan Bao, Guodong Qin, and Yang-Yang Dong. "A Superimposed Pilot-Based Integrated Radar and Communication System". In: *IEEE Access* 8 (2020). ISSN: 2169-3536. DOI: 10.1109/ACCESS.2020.2965153. URL: https://ieeexplore.ieee.org/document/8954710/ (visited on 01/21/2025).

[61] Hu ZhaoPeng et al. "OFDM technology anti-multipath performance analysis in China Mobile Multimedia Broadcasting (CMMB) system". In: *2014 IEEE International Frequency Control Symposium (FCS)*. ISSN: 2327-1949. May 2014, pp. 1–3. DOI: 10.1109/FCS.2014.6859892. URL: https://ieeexplore.ieee.org/abstract/document/6859892 (visited on 01/21/2025).

[62] Wenjin Wang et al. "Location-Based Timing Advance Estimation for 5G Integrated LEO Satellite Communications". en. In: *IEEE Transactions on Vehicular Technology* 70.6 (June 2021), pp. 6002–6017. ISSN: 0018-9545, 1939-9359. DOI: 10.1109/TVT.2021.3079936. URL: https://ieeexplore.ieee.org/document/9430740/ (visited on 11/01/2022).

[63] Wallace Alves Martins et al. "Intersymbol and Intercarrier Interference in OFDM Transmissions Through Highly Dispersive Channels". In: *2019 27th European Signal Processing Conference (EUSIPCO)*. ISSN: 2076-1465. Sept. 2019, pp. 1–5. DOI: 10.23919/EUSIPCO.2019.8902648.

[64] Fernando Cruz-Roldán et al. *Intersymbol and Intercarrier Interference in OFDM Systems: Unified Formulation and Analysis*. en. arXiv:2012.04527 [eess]. Dec. 2020. URL: http://arxiv.org/abs/2012.04527 (visited on 06/07/2023).

[65] Mahyar Nemati and Hüseyin Arslan. “Low ICI Symbol Boundary Alignment for 5G Numerology Design”. In: *IEEE Access* 6 (2018). Conference Name: IEEE Access, pp. 2356–2366. ISSN: 2169-3536. DOI: 10.1109/ACCESS.2017.2782830.

[66] Ljiljana Marijanović, Stefan Schwarz, and Markus Rupp. “Multiplexing Services in 5G and Beyond: Optimal Resource Allocation Based on Mixed Numerology and Mini-Slots”. In: *IEEE Access* 8 (2020). Conference Name: IEEE Access, pp. 209537–209555. ISSN: 2169-3536. DOI: 10.1109/ACCESS.2020.3039352.

[67] Abuu B. Kihero, Muhammad Sohaib J. Solaija, and Huseyin Arslan. “Inter-Numerology Interference for Beyond 5G”. en. In: *IEEE Access* 7 (2019), pp. 146512–146523. ISSN: 2169-3536. DOI: 10.1109/ACCESS.2019.2946084. URL: https://ieeexplore.ieee.org/document/8861343/ (visited on 11/01/2022).

[68] Nessrine Trabelsi, Lamia Chaari Fourati, and Chung Shue Chen. “Interference Management in 5G and Beyond Networks”. en. In: ().

[69] Sajjad Ahmad Khan et al. “A Novel Fractional Frequency Reuse Scheme for Interference Management in LTE-A HetNets”. In: *IEEE Access* 7 (2019). Conference Name: IEEE Access, pp. 109662–109672. ISSN: 2169-3536. DOI: 10.1109/ACCESS.2019.2933689. URL: https://ieeexplore.ieee.org/document/8790698 (visited on 04/28/2024).

[70] Li Zhen et al. “Energy-Efficient Random Access for LEO Satellite-Assisted 6G Internet of Remote Things”. In: *IEEE Internet of Things Journal* 8.7 (Apr. 2021). Conference Name: IEEE Internet of Things Journal, pp. 5114–5128. ISSN: 2327-4662. DOI: 10.1109/JIOT.2020.3030856. URL: https://ieeexplore.ieee.org/document/9222142 (visited on 05/14/2024).

[71] Wang Sixin et al. “Doppler frequency-code phase division multiple access technique for LEO navigation signals”. en. In: *GPS Solutions* 26.3 (June 2022), p. 98. ISSN: 1521-1886. DOI: 10.1007/s10291-022-01283-7. URL: https://doi.org/10.1007/s10291-022-01283-7 (visited on 01/25/2024).

[72] Xingqin Lin, Dongsheng Yu, and Henning Wiemann. “A Primer on Bandwidth Parts in 5G New Radio”. en. In: *5G and Beyond*. Ed. by Xingqin Lin and Namyoon Lee. Cham: Springer International Publishing, 2021, pp. 357–370. DOI: 10.1007/978-3-030-58197-8_12. URL: http://link.springer.com/10.1007/978-3-030-58197-8_12 (visited on 11/01/2022).

[73] Li You et al. “Integrated Communications and Localization for Massive MIMO LEO Satellite Systems”. In: *IEEE Transactions on Wireless Communications* 23.9 (Sept. 2024). Conference Name: IEEE Transactions on Wireless Communications, pp. 11061–11075. ISSN: 1558-2248. DOI: 10.1109/TWC.2024.3378305. URL: https://ieeexplore.ieee.org/document/10478820/authors#authors (visited on 11/16/2024).

[74] Konstantinos Ntontin et al. “A Vision, Survey, and Roadmap Toward Space Communications in the 6G and Beyond Era”. In: *Proceedings of the IEEE* (2025). Conference Name: Proceedings of the IEEE, pp. 1–37. ISSN: 1558-2256. DOI: 10.1109/JPROC.2024.3512934. URL: https://ieeexplore.ieee.org/document/10820534 (visited on 01/21/2025).

[75] Arash Shahmansoori et al. “Design of OFDM sequences for joint communications and positioning based on the asymptotic expected CRB”. en. In: *International Conference on Localization and GNSS 2014 (ICL-GNSS 2014)*. Helsinki: IEEE, June 2014, pp. 1–6. ISBN: 978-1-4799-5123-9. DOI: 10.1109/ICL-GNSS.2014.6934168. URL: https://ieeexplore.ieee.org/document/6934168/ (visited on 11/01/2022).

[76] Rebecca Carrie Adam and Peter Adam Hoeher. “Simultaneous Model and Parameter Estimation for Joint Communication and Positioning”. In: *IEEE Access* 9 (2021). Conference Name: IEEE Access, pp. 2934–2949. ISSN: 2169-3536. DOI: 10.1109/ACCESS.2020.3047618.

[77] Wei Wang et al. “A Semiblind Tracking Algorithm for Joint Communication and Ranging With OFDM Signals”. en. In: *IEEE Transactions on Vehicular Technology* 65.7 (July 2016), pp. 5237–5250. ISSN: 0018-9545, 1939-9359. DOI: 10.1109/TVT.2015.2468079. URL: http://ieeexplore.ieee.org/document/7194841/ (visited on 11/01/2022).

[78] Hongtao Xv et al. “Joint Beam Scheduling and Beamforming Design for Cooperative Positioning in Multi-Beam LEO Satellite Networks”. In: *IEEE Transactions on Vehicular Technology* 73.4 (Apr. 2024). Conference Name: IEEE Transactions on Vehicular Technology, pp. 5276–5287. ISSN: 1939-9359. DOI: 10.1109/TVT.2023.3332142. URL: https://ieeexplore.ieee.org/abstract/document/10323191 (visited on 01/21/2025).

[79] Navid Heydarishahreza, Tao Han, and Nirwan Ansari. “Spectrum Sharing and Interference Management for 6G LEO Satellite-Terrestrial Network Integration”.

In: *IEEE Communications Surveys & Tutorials* (2024). Conference Name: IEEE Communications Surveys & Tutorials, pp. 1–1. ISSN: 1553-877X. DOI: 10.1109/COMST.2024.3507019. URL: https://ieeexplore.ieee.org/abstract/document/10769081 (visited on 01/21/2025).

[80] Wooseok Nam et al. "Advanced interference management for 5G cellular networks". In: *IEEE Communications Magazine* 52.5 (May 2014). Conference Name: IEEE Communications Magazine, pp. 52–60. ISSN: 1558-1896. DOI: 10.1109/MCOM.2014.6815893. URL: https://ieeexplore.ieee.org/abstract/document/6815893 (visited on 01/21/2025).

[81] Peng He et al. "Non-Terrestrial Network Technologies: Applications and Future Prospects". In: *IEEE Internet of Things Journal* (2024). Conference Name: IEEE Internet of Things Journal, pp. 1–1. ISSN: 2327-4662. DOI: 10.1109/JIOT.2024.3522912. URL: https://ieeexplore.ieee.org/abstract/document/10816483 (visited on 01/21/2025).

[82] Pranita Bhide, Dhanush Shetty, and Suresh Mikkili. "Review on 6G communication and its architecture, technologies included, challenges, security challenges and requirements, applications, with respect to AI domain". en. In: *IET Quantum Communication* (Dec. 2024), qtc2.12114. ISSN: 2632-8925, 2632-8925. DOI: 10.1049/qtc2.12114. URL: https://ietresearch.onlinelibrary.wiley.com/doi/10.1049/qtc2.12114 (visited on 01/21/2025).

[83] Stamatia F. Drampalou et al. "A User-Centric Perspective of 6G Networks: A Survey". In: *IEEE Access* 12 (2024). Conference Name: IEEE Access, pp. 190255–190294. ISSN: 2169-3536. DOI: 10.1109/ACCESS.2024.3516194. URL: https://ieeexplore.ieee.org/abstract/document/10795171 (visited on 01/21/2025).

[84] Andrew M. Graff et al. "Analysis of OFDM Signals for Ranging and Communications". en. In: St. Louis, Missouri, Oct. 2021, pp. 2910–2924. DOI: 10.33012/2021.17991. URL: https://www.ion.org/publications/abstract.cfm?articleID=17991 (visited on 12/11/2022).

[85] Ruoxu Chen, Xiaofeng Lu, and Kun Yang. "Joint Resource Allocation Based on F-OFDM for Integrated Communication and Positioning System". en. In: *Communications and Networking*. Ed. by Honghao Gao et al. Cham: Springer International Publishing, 2022, pp. 91–101. ISBN: 978-3-030-99200-2. DOI: 10.1007/978-3-030-99200-2_8.

[86] Tao Cui and Chintha Tellambura. "OFDM channel estimation and data detection with superimposed pilots". en. In: *European Transactions on Telecommunications* 22.3 (2011). _eprint: https://onlinelibrary.wiley.com/doi/pdf/10.1002/ett.1461, pp. 125–136. ISSN: 1541-8251. DOI: 10.1002/ett.1461. URL: https://onlinelibrary.wiley.com/doi/abs/10.1002/ett.1461 (visited on 03/18/2024).

[87] Angiras R. Varma et al. "Optimal Superimposed Pilot Selection for OFDM Channel Estimation". In: *2006 IEEE 7th Workshop on Signal Processing Advances in Wireless Communications*. ISSN: 1948-3252. July 2006, pp. 1–5. DOI: 10.1109/SPAWC.2006.346490. URL: https://ieeexplore.ieee.org/abstract/document/4153906 (visited on 01/21/2025).

[88] Karthik Upadhya, Sergiy A. Vorobyov, and Mikko Vehkapera. "Superimposed Pilots Are Superior for Mitigating Pilot Contamination in Massive MIMO". In: *IEEE Transactions on Signal Processing* 65.11 (June 2017). Conference Name: IEEE Transactions on Signal Processing, pp. 2917–2932. ISSN: 1941-0476. DOI: 10.1109/TSP.2017.2675859. URL: https://ieeexplore.ieee.org/abstract/document/7865983 (visited on 01/21/2025).

[89] Amer A. Hassan, John E. Hershey, and Gary J. Saulnier. "OFDM Spread Spectrum Communications". en. In: *Perspectives in Spread Spectrum*. Springer, Boston, MA, 1998, pp. 35–58. ISBN: 978-1-4615-5531-5. DOI: 10.1007/978-1-4615-5531-5_2. URL: https://link.springer.com/chapter/10.1007/978-1-4615-5531-5_2 (visited on 03/04/2025).

[90] Pingzhou Tu, Xiaojing Huang, and Eryk Dutkiewicz. "A Novel Approach of Spreading Spectrum in OFDM Systems". In: *2006 International Symposium on Communications and Information Technologies*. Oct. 2006, pp. 487–491. DOI: 10.1109/ISCIT.2006.339994. URL: https://ieeexplore.ieee.org/document/4141433 (visited on 04/02/2025).

[91] Zaher M. Kassas et al. "Navigation with Multi-Constellation LEO Satellite Signals of Opportunity: Starlink, OneWeb, Orbcomm, and Iridium". In: *2023 IEEE/ION Position, Location and Navigation Symposium (PLANS)*. ISSN: 2153-3598. Apr. 2023, pp. 338–343. DOI: 10.1109/PLANS53410.2023.10140066. URL: https://ieeexplore.ieee.org/document/10140066/ (visited on 11/14/2023).

[92] Zaher M. Kassas. "Navigation from Low Earth Orbit – Part 2: Models, Implementation, and Performance". In: *Position, Navigation, and Timing Technologies in the 21st*

Century: Integrated Satellite Navigation, Sensor Systems, and Civil Applications, Volume 2. 2021.

[93] Steven M. Kay. *Fundamentals of statistical signal processing*. Prentice Hall signal processing series. Englewood Cliffs, N.J: Prentice-Hall PTR, 1993.

[94] Dehan Luan. "Fundamental Performance Limits on Time of Arrival Estimation Accuracy with 5G Radio Access". en. PhD thesis. 2017.

[95] Ting He and Zherui Ma. "Proposed OFDM Modulation for Future Generations of GNSS Signal System". en. In: *The Journal of Navigation* 69.5 (Sept. 2016), pp. 971–990. ISSN: 0373-4633, 1469-7785. DOI: 10.1017/S0373463316000059. URL: https://www.cambridge.org/core/journals/journal-of-navigation/article/proposed-ofdm-modulation-for-future-generations-of-gnss-signal-system/1389D99AB66AC3D4C64E0031BA46A685# (visited on 04/25/2025).

[96] Jingfang Su et al. "Design and performance evaluation of a novel ranging signal based on an LEO satellite communication constellation". EN. In: *Geo-spatial Information Science* (Jan. 2023). Publisher: Taylor & Francis. ISSN: 1009-5020. URL: https://www.tandfonline.com/doi/abs/10.1080/10095020.2022.2121229 (visited on 04/25/2025).

[97] Daniel Egea-Roca et al. "Performance Analysis of a Multi-Slope Chirp Spread Spectrum Signal for PNT in a LEO Constellation". In: *2022 10th Workshop on Satellite Navigation Technology (NAVITEC)*. ISSN: 2325-5455. Apr. 2022, pp. 1–9. DOI: 10.1109/NAVITEC53682.2022.9847559. URL: https://ieeexplore.ieee.org/document/9847559 (visited on 04/25/2025).

[98] Fran Fabra et al. "Analysis on Signals for LEO-PNT Beyond GNSS". en. In: *2024 32nd European Signal Processing Conference (EUSIPCO)*. Lyon, France: IEEE, Aug. 2024, pp. 1237–1241. ISBN: 978-94-6459-361-7. DOI: 10.23919/EUSIPCO63174.2024.10714965. URL: https://ieeexplore.ieee.org/document/10714965/ (visited on 04/25/2025).

[99] En Yuan et al. "Ranging Method for Navigation Based on High-Speed Frequency-Hopping Signal". In: *IEEE Access* 6 (2018), pp. 4308–4320. ISSN: 2169-3536. DOI: 10.1109/ACCESS.2017.2787801. URL: https://ieeexplore.ieee.org/document/8241378 (visited on 04/25/2025).

[100] Dong Fu et al. “Delay–Doppler Block Division Multiplexing: An Integrated Navigation and Communication Waveform for LEO PNT”. en. In: *Remote Sensing* 17.7 (Jan. 2025). Number: 7 Publisher: Multidisciplinary Digital Publishing Institute, p. 1270. ISSN: 2072-4292. DOI: 10.3390/rs17071270. URL: https://www.mdpi.com/2072-4292/17/7/1270 (visited on 04/25/2025).

[101] *The Base Stations' Networking Scheme and Spreading Code Optimization Strategy of TC-OFDM — springerprofessional.de*. de. URL: https://link.springer.com/chapter/10.1007/978-981-15-3707-3_46 (visited on 04/25/2025).

[102] Hui Chen et al. “Modeling and Analysis of OFDM-based 5G/6G Localization under Hardware Impairments”. In: *IEEE Transactions on Wireless Communications* (2023). Conference Name: IEEE Transactions on Wireless Communications, pp. 1–1. ISSN: 1558-2248. DOI: 10.1109/TWC.2023.3339523. URL: https://ieeexplore.ieee.org/document/10355872 (visited on 12/18/2023).

[103] Yi Hong, Tharaj Thaj, and Emanuele Viterbo. *Delay-Doppler communications principles and applications*. eng. OCLC: 1297827135. London: Academic Press, an imprint of Elsevier, 2022. ISBN: 978-0-323-85966-0.

[104] Suvra Sekhar Das and Ramjee Prasad. “OTFS: Orthogonal Time Frequency Space Modulation A Waveform for 6G”. In: *OTFS: Orthogonal Time Frequency Space Modulation A Waveform for 6G*. Conference Name: OTFS: Orthogonal Time Frequency Space Modulation A Waveform for 6G. River Publishers, 2021, pp. i–xxvi. ISBN: 978-87-7022-655-4. URL: https://ieeexplore.ieee.org/document/9661102 (visited on 11/06/2024).

[105] Zacharias M. Komodromos, Wenkai Qin, and Todd E. Humphreys. “Signal Simulator for Starlink Ku-Band Downlink”. en. In: Denver, Colorado, Oct. 2023, pp. 2798–2812. DOI: 10.33012/2023.19308. URL: https://www.ion.org/publications/abstract.cfm?articleID=19308 (visited on 01/10/2024).

[106] Mohammad Neinavaie and Zaher M. Kassas. “Unveiling Starlink LEO Satellite OFDM-Like Signal Structure Enabling Precise Positioning”. In: *IEEE Transactions on Aerospace and Electronic Systems* 60.2 (Apr. 2024), pp. 2486–2489. ISSN: 0018-9251, 1557-9603, 2371-9877. DOI: 10.1109/TAES.2023.3265951. URL: https://ieeexplore.ieee.org/document/10098597/ (visited on 05/19/2025).

[107] Igor Kim, Jungsun Um, and Seungkeun Park. “Implementation of SDR-based 5G NR Cell Search Equipment”. en. In: (2020), p. 4.

[108] 3GPP. *NR; Physical channels and modulation*. Technical Specification (TS) 38.211. 3GPP, 2024. URL: https://portal.3gpp.org/desktopmodules/Specifications/SpecificationDetails.aspx?specificationId=3213.

[109] Ali A. Abdallah, Kimia Shamaei, and Zaher M. Kassas. "Assessing Real 5G Signals for Opportunistic Navigation". en. In: Oct. 2020, pp. 2548–2559. DOI: 10.33012/2020.17702. URL: https://www.ion.org/publications/abstract.cfm?articleID=17702 (visited on 07/05/2023).

[110] Chun Yang and Andrey Soloviev. "Starlink Doppler and Doppler Rate Estimation via Coherent Combining of Multiple Tones for Opportunistic Positioning". In: *2023 IEEE/ION Position, Location and Navigation Symposium (PLANS)*. ISSN: 2153-3598. Apr. 2023, pp. 1143–1153. DOI: 10.1109/PLANS53410.2023.10140055.

[111] Mohammad Neinavaie, Joe Khalife, and Zaher M. Kassas. "Acquisition, Doppler Tracking, and Positioning With Starlink LEO Satellites: First Results". In: *IEEE Transactions on Aerospace and Electronic Systems* 58.3 (June 2022). Conference Name: IEEE Transactions on Aerospace and Electronic Systems, pp. 2606–2610. ISSN: 1557-9603. DOI: 10.1109/TAES.2021.3127488. URL: https://ieeexplore.ieee.org/document/9612022 (visited on 01/26/2024).

[112] Todd E. Humphreys et al. "Signal Structure of the Starlink Ku-Band Downlink". en. In: *IEEE Transactions on Aerospace and Electronic Systems* (2023), pp. 1–16. ISSN: 0018-9251, 1557-9603, 2371-9877. DOI: 10.1109/TAES.2023.3268610. URL: https://ieeexplore.ieee.org/document/10107477/ (visited on 07/26/2023).

[113] Alejandro Gonzalez-Garrido et al. "Interference Analysis and Modeling of Positioning Reference Signals in 5G NTN". In: *IEEE Open Journal of the Communications Society* 5 (2024). Conference Name: IEEE Open Journal of the Communications Society, pp. 7567–7581. ISSN: 2644-125X. DOI: 10.1109/OJCOMS.2024.3503692. URL: https://ieeexplore.ieee.org/document/10759698 (visited on 02/13/2025).

[114] Gonzalez-Garrido. Alejandro, Querol. Jorge, and Chatzinotas. Symeon. "Analysis of the SINR in LEO-PNT Systems with 5G PRS Multiplexing: Integration of PRS and NTN". In: *ICASSP 2024 - 2024 IEEE International Conference on Acoustics, Speech and Signal Processing (ICASSP)*. ISSN: 2379-190X. Apr. 2024, pp. 13016–13020. DOI: 10.1109/ICASSP48485.2024.10447159. URL: https://ieeexplore.ieee.org/document/10447159 (visited on 07/13/2025).

[115] Alejandro Gonzalez-Garrido et al. “Assessing 5G PRS signal interference in high frequency NTN Fused PNT applications”. In: *Metroaerospace 2025*. Naples, Italy, June 2025.

[116] Puneeth Jubba Honnaiah et al. “Demand-Driven Beam Densification in Multibeam Satellite Communication Systems”. In: *IEEE Transactions on Aerospace and Electronic Systems* 59.5 (Oct. 2023). Conference Name: IEEE Transactions on Aerospace and Electronic Systems, pp. 6534–6554. ISSN: 1557-9603. DOI: 10.1109/TAES.2023.3278253. URL: https://ieeexplore.ieee.org/document/10130323 (visited on 01/16/2024).

[117] Juan Misael Gongora-Torres et al. “Elevation Angle Characterization for LEO Satellites: First and Second Order Statistics”. en. In: *Applied Sciences* 13.7 (Jan. 2023). Number: 7 Publisher: Multidisciplinary Digital Publishing Institute, p. 4405. ISSN: 2076-3417. DOI: 10.3390/app13074405. URL: https://www.mdpi.com/2076-3417/13/7/4405 (visited on 11/28/2023).

[118] Sheng-Yi Li and Kai-Yuan Wang. “Application of maximum elevation angle probability density function to macroscopic selection diversity in low earth orbiting satellite constellation systems”. en. In: *International Journal of Satellite Communications and Networking* 30.5 (2012), pp. 212–220. ISSN: 1542-0981. DOI: 10.1002/sat.1013. URL: https://onlinelibrary.wiley.com/doi/abs/10.1002/sat.1013 (visited on 08/21/2024).

[119] Anna Talgat, Mustafa A. Kishk, and Mohamed-Slim Alouini. “Stochastic Geometry-Based Analysis of LEO Satellite Communication Systems”. In: *IEEE Communications Letters* 25.8 (Aug. 2021). Conference Name: IEEE Communications Letters, pp. 2458–2462. ISSN: 1558-2558. DOI: 10.1109/LCOMM.2020.3029808. URL: https://ieeexplore.ieee.org/document/9218989 (visited on 11/29/2023).

[120] Niloofar Okati et al. “Downlink Coverage and Rate Analysis of Low Earth Orbit Satellite Constellations Using Stochastic Geometry”. In: *IEEE Transactions on Communications* 68.8 (Aug. 2020). Conference Name: IEEE Transactions on Communications, pp. 5120–5134. ISSN: 1558-0857. DOI: 10.1109/TCOMM.2020.2990993.

[121] Talha Ahmed Khan and Mehtnaz Afshang. “A Stochastic Geometry Approach to Doppler Characterization in a LEO Satellite Network”. In: *ICC 2020 - 2020 IEEE International Conference on Communications (ICC)*. ISSN: 1938-1883. June 2020,

pp. 1–6. DOI: 10.1109/ICC40277.2020.9148880. URL: https://ieeexplore.ieee.org/document/9148880 (visited on 12/08/2023).

[122] A. González et al. "LEO Satellites for PNT, the Next Step for Precise Positioning Applications". en. In: *Proceedings of the 35th International Technical Meeting of the Satellite Division of The Institute of Navigation (ION GNSS+ 2022)*. ISSN: 2331-5954. Sept. 2022, pp. 2573–2581. DOI: 10.33012/2022.18436. URL: http://www.ion.org/publications/abstract.cfm?jp=p&articleID=18436 (visited on 09/19/2024).

[123] Victor Monzon Baeza et al. "An Overview of Channel Models for NGSO Satellites". In: *2022 IEEE 96th Vehicular Technology Conference (VTC2022-Fall)*. ISSN: 2577-2465. Sept. 2022, pp. 1–6. DOI: 10.1109/VTC2022-Fall57202.2022.10012693. URL: https://ieeexplore.ieee.org/document/10012693 (visited on 10/03/2023).

[124] John A. Klobuchar. "Ionospheric Time-Delay Algorithm for Single-Frequency GPS Users". In: *IEEE Transactions on Aerospace and Electronic Systems* AES-23.3 (May 1987). Conference Name: IEEE Transactions on Aerospace and Electronic Systems, pp. 325–331. ISSN: 1557-9603. DOI: 10.1109/TAES.1987.310829. URL: https://ieeexplore.ieee.org/document/4104345 (visited on 12/20/2023).

[125] G. Di Giovanni and S. M. Radicella. "An analytical model of the electron density profile in the ionosphere". In: *Advances in Space Research* 10.11 (Jan. 1990), pp. 27–30. ISSN: 0273-1177. DOI: 10.1016/0273-1177(90)90301-F. URL: https://www.sciencedirect.com/science/article/pii/027311779090301F (visited on 12/20/2023).

[126] Jaume Sanz Subirana, José Miguel Juan Zornoza, and Manuel Hernández-Pajares. *GNSS DATA Processing. Fundamentals and algorithms. Vol. 1.* English. OCLC: 922681096. Noordwijk: ESA Communications, 2013. ISBN: 978-92-9221-886-7.

[127] Alejandro Gonzalez-Garrido. *Starlink satellite passes*. tex.entrytype: data. 2024. DOI: 10.21227/qggt-xr49. URL: https://dx.doi.org/10.21227/qggt-xr49.

[128] Jorge Querol et al. "SNR Degradation in GNSS-R Measurements Under the Effects of Radio-Frequency Interference". In: *IEEE Journal of Selected Topics in Applied Earth Observations and Remote Sensing* 9.10 (Oct. 2016). Conference Name: IEEE Journal of Selected Topics in Applied Earth Observations and Remote Sensing, pp. 4865–4878. ISSN: 2151-1535. DOI: 10.1109/JSTARS.2016.2597438.

[129] Enric Juan et al. “Handover Solutions for 5G Low-Earth Orbit Satellite Networks”. In: *IEEE Access* 10 (2022). Conference Name: IEEE Access, pp. 93309–93325. ISSN: 2169-3536. DOI: 10.1109/ACCESS.2022.3203189.

[130] Karin Schuler and Werner Wiesbeck. “Tapering of Multitransmit Digital Beamforming Arrays”. In: *IEEE Transactions on Antennas and Propagation* 56.7 (July 2008). Conference Name: IEEE Transactions on Antennas and Propagation, pp. 2125–2127. ISSN: 1558-2221. DOI: 10.1109/TAP.2008.924774. URL: https://ieeexplore.ieee.org/abstract/document/4558316 (visited on 01/21/2025).

[131] Ahmed Ben Ayed, Patrick Mitran, and Slim Boumaiza. “Novel Algorithm to Synthesize the Tapering Profile for Enhanced Linearization of RF Beamforming Arrays Over a Wide Steering Range”. In: *IEEE Transactions on Microwave Theory and Techniques* 71.8 (Aug. 2023). Conference Name: IEEE Transactions on Microwave Theory and Techniques, pp. 3691–3700. ISSN: 1557-9670. DOI: 10.1109/TMTT.2023.3248151. URL: https://ieeexplore.ieee.org/abstract/document/10066144 (visited on 01/21/2025).

[132] H. Cox and Hung Lai. “Sub-aperture beam-based adaptive beamforming for large dynamic arrays”. In: *Conference Record of the Thirty-Eighth Asilomar Conference on Signals, Systems and Computers, 2004.* Vol. 2. Nov. 2004, 2355–2358 Vol.2. DOI: 10.1109/ACSSC.2004.1399590. URL: https://ieeexplore.ieee.org/abstract/document/1399590 (visited on 01/21/2025).

[133] Karin Plimon et al. “Subset Precoding and Tapering on Phased Arrays for High Throughput Satellite Systems”. In: *2022 13th International Symposium on Communication Systems, Networks and Digital Signal Processing (CSNDSP)*. July 2022, pp. 115–120. DOI: 10.1109/CSNDSP54353.2022.9907918. URL: https://ieeexplore.ieee.org/abstract/document/9907918 (visited on 01/21/2025).

[134] D. Parker and D.C. Zimmermann. “Phased arrays - part 1: theory and architectures”. In: *IEEE Transactions on Microwave Theory and Techniques* 50.3 (Mar. 2002). Conference Name: IEEE Transactions on Microwave Theory and Techniques, pp. 678–687. ISSN: 1557-9670. DOI: 10.1109/22.989953. URL: https://ieeexplore.ieee.org/abstract/document/989953 (visited on 01/23/2025).

[135] Wei Hong et al. “Multibeam Antenna Technologies for 5G Wireless Communications”. In: *IEEE Transactions on Antennas and Propagation* 65.12 (Dec. 2017). Conference Name: IEEE Transactions on Antennas and Propagation, pp. 6231–6249. ISSN:

1558-2221. DOI: 10.1109/TAP.2017.2712819. URL: https://ieeexplore.ieee.org/abstract/document/7942144 (visited on 01/23/2025).

[136] T.M. Schmidl and D.C. Cox. "Robust frequency and timing synchronization for OFDM". en. In: *IEEE Transactions on Communications* 45.12 (Dec. 1997), pp. 1613–1621. ISSN: 00906778. DOI: 10.1109/26.650240. URL: http://ieeexplore.ieee.org/document/650240/ (visited on 11/01/2022).

[137] Yang Sun et al. "Handover for Multi-Beam LEO Satellite Networks: A Multi-Objective Reinforcement Learning Method". In: *IEEE Communications Letters* 28.12 (Dec. 2024). Conference Name: IEEE Communications Letters, pp. 2834–2838. ISSN: 1558-2558. DOI: 10.1109/LCOMM.2024.3470890. URL: https://ieeexplore.ieee.org/abstract/document/10700698 (visited on 04/02/2025).

[138] 3GPP. *38.821 - Solutions for NR to support Non-Terrestrial Networks (NTN)*. June 2021.

[139] Juan Misael Gongora-Torres et al. "Link Budget Analysis for LEO Satellites Based on the Statistics of the Elevation Angle". In: *IEEE Access* 10 (2022). Conference Name: IEEE Access, pp. 14518–14528. ISSN: 2169-3536. DOI: 10.1109/ACCESS.2022.3147829. URL: https://ieeexplore.ieee.org/abstract/document/9698051 (visited on 04/02/2025).

[140] Bin Zheng et al. "Inter-beam handover schemes for LEO satellites in 5G satellite–terrestrial integrated networks". In: *Physical Communication* 67 (Dec. 2024), p. 102525. ISSN: 1874-4907. DOI: 10.1016/j.phycom.2024.102525. URL: https://www.sciencedirect.com/science/article/pii/S187449072400243X (visited on 04/02/2025).

[141] Olfa Ben Yahia et al. *Evolution of High Throughput Satellite Systems: Vision, Requirements, and Key Technologies*. en. arXiv:2310.04389 [eess]. Oct. 2023. DOI: 10.48550/arXiv.2310.04389. URL: http://arxiv.org/abs/2310.04389 (visited on 04/02/2025).

[142] Florian Vidal et al. "Flexibility/complexity trade-offs in payload design". In: *Non-Geostationary Satellite Communications Systems*. Books (), pp. 113–142. ISSN: 9781839535666. DOI: 10.1049/PBTE105E_ch6. URL: https://digital-library.theiet.org/doi/10.1049/PBTE105E_ch6 (visited on 04/02/2025).

[143] Patrick K. Bailleul. "A New Era in Elemental Digital Beamforming for Spaceborne Communications Phased Arrays". In: *Proceedings of the IEEE* 104.3 (Mar. 2016). Conference Name: Proceedings of the IEEE, pp. 623–632. ISSN: 1558-2256. DOI: 10.1109/JPROC.2015.2511661. URL: https://ieeexplore.ieee.org/abstract/document/7389972 (visited on 04/02/2025).

[144] J. J. H. Wang. "Antennas for Global Navigation Satellite System (GNSS)". In: *Proceedings of the IEEE* 100.7 (July 2012), pp. 2349–2355. ISSN: 0018-9219, 1558-2256. DOI: 10.1109/JPROC.2011.2179630. URL: http://ieeexplore.ieee.org/document/6130567/ (visited on 02/11/2021).

[145] Jiahao Ning et al. "Ray-Tracing Channel Modeling for LEO Satellite-to-Ground Communication Systems". In: *2024 IEEE/CIC International Conference on Communications in China (ICCC)*. ISSN: 2377-8644. Aug. 2024, pp. 1169–1174. DOI: 10.1109/ICCC62479.2024.10681740. URL: https://ieeexplore.ieee.org/document/10681740 (visited on 06/23/2025).

[146] 3GPP. *TR38.821, Technical Specification Group Radio Access Network; Solutions for NR to support non-terrestrial networks (NTN) (Release 15), V15.2.0*. Technical report. tex.custom_keys: title tex.custom_title: TR38.821 TSG-RAN Solutions for NR to support NTN R15. Dec. 2019.

[147] Riccardo De Gaudenzi and Marco Luise. "Revisiting Band-Limited DS/SS Signal Design for GNSS". In: *2024 11th Workshop on Satellite Navigation Technology (NAVITEC)*. ISSN: 2325-5455. Dec. 2024, pp. 1–5. DOI: 10.1109/NAVITEC63575.2024.10843514. URL: https://ieeexplore.ieee.org/abstract/document/10843514 (visited on 02/05/2025).

[148] Federica Rinaldi et al. "Broadcasting Services Over 5G NR Enabled Multi-Beam Non-Terrestrial Networks". In: *IEEE Transactions on Broadcasting* 67.1 (Mar. 2021). Conference Name: IEEE Transactions on Broadcasting, pp. 33–45. ISSN: 1557-9611. DOI: 10.1109/TBC.2020.2991312. URL: https://ieeexplore.ieee.org/document/9107401 (visited on 12/08/2023).

[149] Miguel Ibarra et al. "Design of antenna arrays for isoflux radiation in satellite systems". In: *2014 IEEE 33rd International Performance Computing and Communications Conference (IPCCC)*. ISSN: 2374-9628. Dec. 2014, pp. 1–2. DOI: 10.1109/PCCC.2014.7017028. URL: https://ieeexplore.ieee.org/abstract/document/7017028 (visited on 11/26/2024).

[150] Alan W. Mast. "Reconfigurable Software Defined Payload architecture that reduces cost and risk for various missions". In: *2011 Aerospace Conference*. ISSN: 1095-323X. Mar. 2011, pp. 1–5. DOI: 10.1109/AERO.2011.5747366. URL: https://ieeexplore.ieee.org/document/5747366 (visited on 06/23/2025).

[151] Roger Birkeland et al. "Development of a multi-purpose SDR payload for the HYPSO-2 satellite". In: *2022 IEEE Aerospace Conference (AERO)*. ISSN: 1095-323X. Mar. 2022, pp. 1–11. DOI: 10.1109/AERO53065.2022.9843447. URL: https://ieeexplore.ieee.org/document/9843447 (visited on 06/23/2025).

[152] Ivan Lapin et al. "STARE: Real-Time Software Receiver for LTE and 5G NR Positioning and Signal Monitoring". en. In: *2022 10th Workshop on Satellite Navigation Technology (NAVITEC)*. Noordwijk, Netherlands: IEEE, Apr. 2022, pp. 1–11. ISBN: 978-1-66541-616-0. DOI: 10.1109/NAVITEC53682.2022.9847544. URL: https://ieeexplore.ieee.org/document/9847544/ (visited on 11/01/2022).

[153] Jordi Vila-Valls et al. "Are PLLs dead? A tutorial on kalman filter-based techniques for digital carrier synchronization". en. In: *IEEE Aerospace and Electronic Systems Magazine* 32.7 (July 2017), pp. 28–45. ISSN: 0885-8985. DOI: 10.1109/MAES.2017.150260. URL: http://ieeexplore.ieee.org/document/8039260/ (visited on 02/19/2024).

[154] Sayed Hossein Dokhanchi, André Noll Barreto, and Gerhard P. Fettweis. "Performance Analysis of Zero-Padded Sequences for Joint Communications and Sensing". In: *IEEE Transactions on Signal Processing* 71 (2023), pp. 1725–1741. ISSN: 1941-0476. DOI: 10.1109/TSP.2023.3273331. URL: https://ieeexplore.ieee.org/document/10121669 (visited on 07/08/2025).

[155] Xuan Liu et al. "Analysis on the Effect of Phase Noise on the Performance of Satellite Communication and Measurement System". en. In: *Symmetry* 15.11 (Nov. 2023). Number: 11 Publisher: Multidisciplinary Digital Publishing Institute, p. 2053. ISSN: 2073-8994. DOI: 10.3390/sym15112053. URL: https://www.mdpi.com/2073-8994/15/11/2053 (visited on 07/08/2025).

[156] D. Petrovic, W. Rave, and G. Fettweis. "Common phase error due to phase noise in OFDM-estimation and suppression". In: *2004 IEEE 15th International Symposium on Personal, Indoor and Mobile Radio Communications*. Vol. 3. Sept. 2004, 1901–1905 Vol.3. DOI: 10.1109/PIMRC.2004.1368329. URL: https://ieeexplore.ieee.org/document/1368329 (visited on 07/08/2025).

[157] Patrick Ellis, Donald Van Rheeden, and Farid Dowla. "Use of Doppler and Doppler Rate for RF Geolocation Using a Single LEO Satellite". en. In: *IEEE Access* 8 (2020), pp. 12907–12920. ISSN: 2169-3536. DOI: 10.1109/ACCESS.2020.2965931. URL: https://ieeexplore.ieee.org/document/8957111/ (visited on 11/01/2022).

[158] *O3b mPOWER — SES*. en. Sept. 2017. URL: https://www.ses.com/o3b-mpower (visited on 07/05/2025).

[159] Muzi Yuan, Xiaomei Tang, and Gang Ou. "Authenticating GNSS civilian signals: a survey". In: *Satellite Navigation* 4.1 (Feb. 2023), p. 6. ISSN: 2662-1363. DOI: 10.1186/s43020-023-00094-6. URL: https://doi.org/10.1186/s43020-023-00094-6 (visited on 03/05/2025).

[160] Henk Wymeersch et al. "Integration of Communication and Sensing in 6G: a Joint Industrial and Academic Perspective". In: *2021 IEEE 32nd Annual International Symposium on Personal, Indoor and Mobile Radio Communications (PIMRC)*. ISSN: 2166-9589. Sept. 2021, pp. 1–7. DOI: 10.1109/PIMRC50174.2021.9569364. URL: https://ieeexplore.ieee.org/document/9569364 (visited on 06/09/2025).

[161] Henk Wymeersch et al. "Joint Communication and Sensing for 6G - A Cross-Layer Perspective". In: *2024 IEEE 4th International Symposium on Joint Communications & Sensing (JC&S)*. Mar. 2024, pp. 01–06. DOI: 10.1109/JCS61227.2024.10646326. URL: https://ieeexplore.ieee.org/document/10646326 (visited on 06/09/2025).

[162] Henk Wymeersch. *Final Models and Measurements for Localization and Sensing*, Deliverable D3.3. Hexa-X Consortium, Jan. 2023.

[163] *Artemis - NASA*. en-US. Section: Artemis. URL: https://www.nasa.gov/humans-in-space/artemis/ (visited on 07/14/2025).

[164] *ESA's Moonlight programme: Pioneering the path for lunar exploration*. en. URL: https://www.esa.int/Applications/Connectivity_and_Secure_Communications/ESA_s_Moonlight_programme_Pioneering_the_path_for_lunar_exploration (visited on 07/14/2025).

[165] Alejandro Gonzalez-Garrido Gonzalez-Garrido. *Starlink satellite passes*. DOI: 10.21227/QGGT-XR49. URL: https://ieee-dataport.org/documents/starlink-satellite-passes (visited on 07/13/2025).

[166] Mike Koivisto et al. “Joint Device Positioning and Clock Synchronization in 5G Ultra-Dense Networks”. en. In: *IEEE Transactions on Wireless Communications* 16.5 (May 2017), pp. 2866–2881. ISSN: 1536-1276. DOI: 10.1109/TWC.2017.2669963. URL: http://ieeexplore.ieee.org/document/7880669/ (visited on 11/01/2022).

[167] Sharbel Kozhaya, Haitham Kanj, and Zaher M. Kassas. “Multi-Constellation Blind Beacon Estimation, Doppler Tracking, and Opportunistic Positioning with OneWeb, Starlink, Iridium NEXT, and Orbcomm LEO Satellites”. en. In: *2023 IEEE/ION Position, Location and Navigation Symposium (PLANS)*. Monterey, CA, USA: IEEE, Apr. 2023, pp. 1184–1195. ISBN: 978-1-66541-772-3. DOI: 10.1109/PLANS53410.2023.10139969. URL: https://ieeexplore.ieee.org/document/10139969/ (visited on 07/18/2023).

[168] William W. Jun et al. “Localizing in Urban Canyons using Joint Doppler and Ranging and the Law of Cosines Method”. en. In: ISSN: 2331-5954. Sept. 2019, pp. 140–153. DOI: 10.33012/2019.16897. URL: http://www.ion.org/publications/abstract.cfm?jp=p&articleID=16897 (visited on 11/01/2022).

[169] Paul C. Chestnut. “Emitter Location Accuracy Using TDOA and Differential Doppler”. In: *IEEE Transactions on Aerospace and Electronic Systems* AES-18.2 (Mar. 1982). Conference Name: IEEE Transactions on Aerospace and Electronic Systems, pp. 214–218. ISSN: 1557-9603. DOI: 10.1109/TAES.1982.309230.